ISSN en trámite

Geofísica Internacional

Revista Trimestral Publicada por el Instituto de Geofísica de la Universidad Nacional Autónoma de México

México
Volume 60 Number 3
July - September
2021

— Geofísica Internacional —

GEOFÍSICA INTERNACIONAL, Año 60, Vol. 60, Núm. 3, julio - septiembre de 2021 es una publicación trimestral, editada por la Universidad Nacional Autónoma de México, Ciudad Universitaria, Alcaldía Coyoacán, C.P. 04150, Ciudad de México, a través del Instituto de Geofísica, Circuito de la Investigación Científica s/n, Ciudad Universitaria, Alcaldía Coyoacán, C.P. 04150, Ciudad de México, Tel. (55)56 22 41 15. URL: http://revistagi.geofisica.unam.mx, correo electrónico: revistagi@igeofisica.unam.mx. Editora responsable: Andrea Rostan Robledo. Certificado de Reserva de Derechos al uso Exclusivo del Título: 04-2022-081610251200-102, ISSN: en trámite, otorgados por el Instituto Nacional del Derecho de Autor (INDAUTOR). Responsable de la última actualización Saúl Armendáriz Sánchez, Editor Técnico. Fecha de la última modificación: 30 de junio 2021, Circuito de la Investigación Científica s/n, Ciudad Universitaria, Alcaldía Coyoacán, C.P. 04150, Ciudad de México.

Geofísica Internacional
Vol. 60, Núm. 3, julio-septiembre de 2021

Contents

Original paper

https://doi.org/10.22201/igeof.00167169p.2021.60.3.1917

LOVE WAVE IN POROUS LAYER UNDER INITIAL STRESS OVER HETEROGENEOUS ELASTIC HALF-SPACE UNDER GRAVITY AND INITIAL STRESS

Asit Kr. Gupta[1], Anup Kr. Mukhopadhyay[2], Pulak Patra[3*], Santimoy Kundu[4]

Received: January 1, 2019; accepted: January 15, 2021; published online: July 1, 2021.

RESUMEN

En este trabajo se estudió el efecto de las tensiones iniciales y la gravedad sobre la propagación de las ondas de Love, lo anterior en la superficie de una capa porosa sobre un semiespacio heterogéneo. Se consideraron dos tipos de límite en superficies libres: (a) límite rígido y (b) límite libre de tracción. La propagación de las ondas de Love ha sido investigada bajo supuestos medios, tanto en los casos de frontera como en un estudio comparativo de dos casos. En ambos, se obtuvieron las ecuaciones de dispersión y las velocidades de fase. Se presentan los cálculos numéricos de forma gráfica. Este estudio de las ondas de Love en el medio supuesto revela que la presencia de tensión inicial en el medio espacio y la ausencia de tensión inicial en la capa, el desplazamiento de la velocidad de fase en un límite rígido es mayor que el límite libre de tracción.

PALABRAS CLAVE: Ondas de Love, propagación, tensión inicial, heterogéneo, poroso y gravedad.

ABSTRACT

In the present paper, the effect of initial stresses and gravity on the propagation of Love waves have been studied in porous layer surface over a heterogeneous half-space. We have considered two types of boundary on free surfaces: (a) rigid boundary and (b) traction free boundary. The propagation of Love waves has been investigated under assumed media in both the cases of boundary and discusses a comparative study of two cases. The dispersion equations and phase velocities have been obtained in both cases. The numerical calculations have been done and presented graphically. This study of Love waves in the assumed medium reveals that the presence of initial stress in the half-space and absence of initial stress in the layer, the displacement of phase velocity in a rigid boundary is more than the traction free boundary.

KEY WORDS. Love wave, propagation, initial stress, heterogeneous, porous and gravity.

* *Corresponding author*: pulakmath11@gmail.com

[1]*Department of Physics, Asansol Engineering College, Asansol, India*

[2]*Department of Computer Science, Asansol Engineering College, Asansol, India*

[3]*Department of Mathematics, Brainware Group of Institutions-SDET, Kolkata, India*

[4]*Department of Applied Mathematics, IIT(ISM), Dhanbad, Jharkhand, India*

INTRODUCTION

The stress is generally developed in media due to natural phenomena. Since the earth is an elastic solid medium under high initial stresses. These stresses play a significant role to propagate an elastic wave. Chattopadhyay et al. (1978) discussed the propagation of Love type waves in an initially stressed crustal layer having an irregular interface. Chakraborty et al. (1981) shows that Love waves propagate in dissipative media under gravity. Chakraborty et al. (1983) discussed the effect of initial stress and irregularity on the propagation of SH-waves. Dey et al. (1996) discussed the propagation of Love waves in heterogeneous crust over a heterogeneous mantle. Abd-Alla et al. (1999) have studied the propagation of Love waves in a non-homogeneous orthotropic elastic layer under initial stress overlying semi-infinite medium. Dey et al. (2004) also studied the propagation of Love waves in an elastic layer with void pores. Sharma (2004) established a mathematical expression about wave propagation in a general anisotropic poroelastic medium with anisotropic permeability phase velocity and attenuation. Kalyani et al. (2008) have made finite-difference modeling of seismic wave propagation in monoclinic media.

Many researchers in the field of elastic wave propagation in layered medium bounded by different forms of irregular boundaries have been studied in several research papers. Such as Anjana and Samal (2010) shows that Love waves propagate in a fluid-saturated porous layer under a rigid boundary and lying over elastic half-space under gravity. Chattaraj and Samal (2013) investigated the propagation of Love waves in the fiber-reinforced layer over a gravitating porous half-space. Gupta et al. (2013a) discussed the propagation of Love waves in a non-homogeneous substratum over an initially stressed heterogeneous half-space. Gupta et al. (2013b) were introduced the possibility of Love wave propagation in a porous layer under the effect of linearly varying directional rigidities. SH-type waves dispersion in an isotropic medium sandwiched between an initially stressed orthotropic and heterogeneous semi-infinite media were studied by Kundu et al. (2013). Manna et al. (2013) show the Love wave propagation in a piezoelectric layer overlying in an inhomogeneous elastic half-space. Bacigalupo and Gambarotta (2014) discussed second-gradient homogenized model for wave propagation in heterogeneous periodic media. Propagation of Love wave in fiber-reinforced medium lying over an initially stressed orthotropic half-space was formulated by Kundu et al. (2014).

In this paper, we have studied the problem of propagation of Love waves in a porous layer over a heterogeneous elastic half-space under gravitating half-space for a rigid boundary as well as traction free boundary in the upper layer. Both the layer is considered under the effect of initial stress. The dispersion relations have been derived for rigid boundary as well as traction free boundary. The initial stresses play a vital role on the propagation of Love waves in the assumed medium. Gravity and heterogeneity in the half-space play a notable effect on the propagation of Love waves in the medium and half-space. The influences of porosity, initial stresses, and gravitational parameters have discussed graphically.

FORMULATION OF THE PROBLEM

We consider a model consisting of the water-saturated anisotropic poroelastic layer under initial stress of finite thickness laying (Figure 1 under traction free boundary and Figure 2 under rigid boundary) over a gravitating heterogeneous elastic half-space under initial stress. Considering the origin of the coordinate system at the interface of the crust and mantle, z-axis downloads positively. The following variation has been taken.

For the half-space $\mu = \mu_2(1 + a_1 z), \rho = \rho_2$

where, μ and ρ is the rigidity and density of the half space, a be the constant having inverse of length.

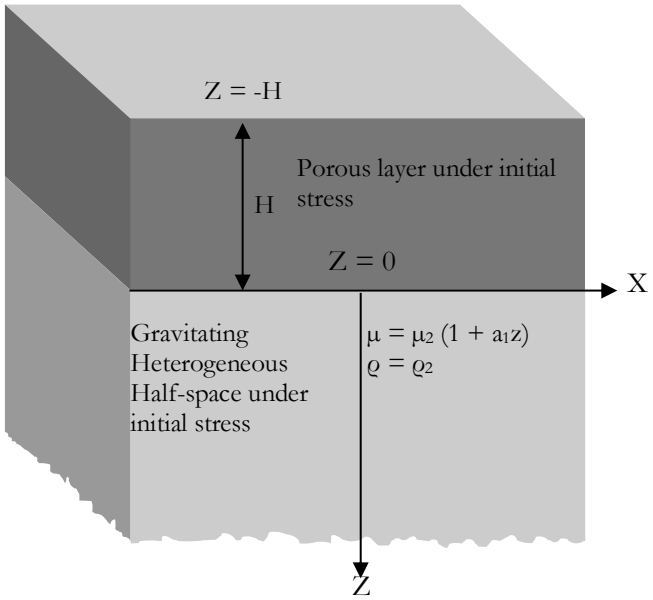

Figure 1: Geometry of the problem

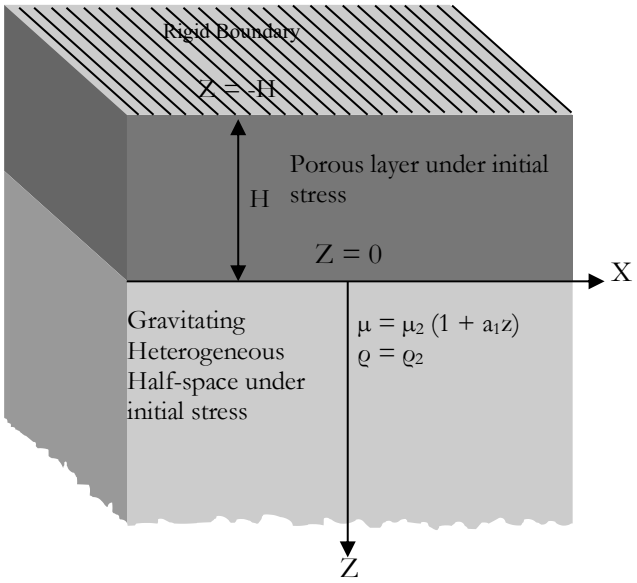

Figure 2: Geometry of the problem

SOLUTION OF THE POROUS LAYER

For the fluid-saturated anisotropic porous layer under initial stress P_1 in the absence of body forces, the equation of motion can be written as (Biot, 1965).

$$\frac{\partial s_{21}^{'}}{\partial x}+\frac{\partial s_{22}^{'}}{\partial y}+\frac{\partial s_{23}^{'}}{\partial z}-P_1\frac{\partial \omega_z}{\partial x}=\frac{\partial^2}{\partial t^2}(\rho_{11}v_y^{'}+\rho_{12}V_y)$$
$$\frac{\partial S}{\partial y}=\frac{\partial^2}{\partial t^2}(\rho_{12}v_y^{'}+\rho_{22}V_y)$$
$$s_{23}^{'}=2L\,e_{yz}\ ,\ s_{12}^{'}=2N\,e_{xy},\ s_{22}^{'}=(A-2N)e_{xx}+Ae_{yy}+Fe_{zz}+Q\varepsilon \qquad (1)$$

where, $s_{ij}^{'}$ are the components of stress tensor in the solid, $S(=-fp)$ is the reduced pressure of the fluid, p is the pressure in the fluid, and f is the porosity of the porous layer, $(u_x^{'},v_y^{'},w_z^{'})$ are the components of the displacement vector of the solid and (U_x,V_y,W_z) are those of fluid. L and N are represent the shear moduli of the anisotropic layer in the x- and z- direction respectively, whereas A and F are elastic constants for the medium. The positive quantity Q is the measure of coupling between the changes in the volume of solid and liquid.

Since the Love waves propagating along the x-direction, having the displacement of particles along the y-direction, we have

$$u_x^{'}=0,v_y^{'}=v(x,z,t),w_z^{'}=0$$
$$U_x=0,V_y=V(x,z,t),W_z=0$$

This displacement will produce e_{yz} and e_{xy} strain components and others are vanishing.

The dynamic components $\rho_{11,},\rho_{12},\rho_{22}$ take into account the inertia effects of the moving fluid and are related to the densities of the solid ρ_s, fluid ρ_f and the layer $\rho^{'}$ by the equations

$$\rho_{11}+\rho_{22}=(1-f)\rho_s\ ,\ \rho_{12}+\rho_{22}=f\rho_f$$

So that the mass density of the aggregate is

$$\rho^{'}=\rho_{11}+2\rho_{12}+\rho_{22}=\rho_s+f(\rho_f-\rho_s)$$

Also

$$\rho_{11}>0,\ \rho_{12}\le 0,\ \rho_{22}>0\ ,\ \rho_{11}\rho_{22}-{\rho_{12}}^2>0.$$

The Love wave equation takes the form

$$(N-\frac{P_1}{2})\frac{\partial^2 v}{\partial x^2}+L\frac{\partial^2 v}{\partial z^2}=\frac{\partial^2}{\partial t^2}\left[\rho_{11}v+\rho_{12}V\right]\ \text{and}$$
$$\frac{\partial^2}{\partial t^2}\left[\rho_{12}v+\rho_{22}V\right]=0 \qquad (2)$$

Hence, we have from (2)

$$(N-\frac{P_1}{2})\frac{\partial^2 v}{\partial x^2}+L\frac{\partial^2 v}{\partial z^2}=d_1\frac{\partial^2 v}{\partial t^2}$$

where $d_1=\rho_{11}-\frac{{\rho_{12}}^2}{\rho_{22}}$, $V=(d_2-\rho_{12}v)/\rho_{22}$, $d_2=[\rho_{12}v+\rho_{22}V]$ (3)

The shear wave velocity in the porous layer along the x-direction can be expressed as

$$\beta'=\sqrt{\frac{\left(N-\frac{P_1}{2}\right)}{d_1}}=\beta_1\sqrt{\left(1-\frac{\xi_1}{d}\right)}$$

where $d=\gamma_{11}-\left(\frac{\gamma_{12}^2}{\gamma_{22}}\right)$, $\beta_1=\sqrt{\frac{N}{\rho'}}$, is the velocity of shear wave in the corresponding initial stress free non-porous, anisotropic, elastic medium along x-direction.

$\xi_1=\frac{P_1}{2N}$, is the non-dimensional parameter due to the initial stress P_1 and

$\gamma_{11}=\frac{\rho_{11}}{\rho'}$, $\gamma_{12}=\frac{\rho_{12}}{\rho'}$ and $\gamma_{22}=\frac{\rho_{22}}{\rho'}$, are the non-dimensional parameter for the material of the porous layer as obtained by Biot (1965)

We consider

$$v(x,z,t)=f(z)e^{i(kx-\omega t)} \tag{4}$$

where, k is the wave number and ω is the angular frequency.

Now, we get

$$\frac{d^2 f(z)}{dz^2}+q_1^2 f(z)=0,$$

where $q_1^2=\frac{k^2}{L}\left(c^2 d-\left(N-\frac{P_1}{2}\right)\right)=k^2\left\{\alpha d\left(\frac{c^2}{\beta_1^2}-\frac{1-\xi_1}{d}\right)\right\}$, $\alpha=\frac{N}{L}$, $\omega=kc$

(5)

The solution of equation (5)

$$f(z)=Ae^{iq_1 z}+Be^{-iq_1 z}$$

where A and B are constants (6)

Hence, finally we get

$$v_1(x,z,t)=(Ae^{iq_1 z}+Be^{-iq_1 z})e^{i(kx-\omega t)} \tag{7}$$

THE DYNAMIC EQUATION OF THE MOTION IN THE HALF-SPACE

The dynamic equation of motion in the half space may be written as Biot (1965)

$$\frac{\partial S_{12}}{\partial x}+\frac{\partial S_{22}}{\partial y}+\frac{\partial S_{23}}{\partial z}-\rho g\omega_{23}+\rho gz\frac{\partial \omega_{12}}{\partial x}-\rho gz\frac{\partial \omega_{23}}{\partial z}-\frac{P_2}{2}\frac{\partial v}{\partial x^2}=\rho\frac{\partial^2 v_2}{\partial t^2} \tag{8}$$

where, $v_2(x,z,t)$ is the displacement along y direction, ρ is the density, S_{ij} are incremental stress and ω_{ij} are rotational components in the half space and g is the acceleration due to gravity. P_2, is the initial stress.

The components of body forces are $X=0$, $Y=0$, $Z=g$.

The stress-strain relations are

$$S_{12}=2\mu e_{xy}\text{ , }S_{23}=2\mu e_{yz}\text{ , }e_{ij}=\frac{1}{2}\left(\frac{\partial u_i}{\partial x_j}+\frac{\partial u_j}{\partial x_i}\right)$$

$$e_{xy}=\tfrac{1}{2}\left(\frac{\partial v_1}{\partial y}+\frac{\partial v_2}{\partial x}\right),\ e_{yz}=\tfrac{1}{2}\left(\frac{\partial v_2}{\partial z}+\frac{\partial v_3}{\partial y}\right)$$

In this problem $\frac{\partial}{\partial y}=0$ and $\mu=\mu_2(1+a_1z)$, $\rho=\rho_2$, the stress strain relation becomes

$$e_{xy}=\tfrac{1}{2}\frac{\partial v_2}{\partial x},\quad e_{yz}=\frac{1}{2}\frac{\partial v_2}{\partial z}$$

$$S_{12}=\mu_2(1+a_1z)\frac{\partial v_2}{\partial x}\text{ , }\quad S_{23}=\mu_2(1+a_1z)\frac{\partial v_2}{\partial z}$$

(9)

where, μ is the modulus of rigidity, a_1 is a variation parameter of a rigidity having dimension inverse of length.

Equation (8) using the above relations takes the form

$$\left[\mu_2(1+a_1z)-\frac{1}{2}\rho_2gz-\frac{P_2}{2}\right]\frac{\partial^2 v_2}{\partial x^2}+\left[\mu_2(1+a_1z)-\frac{1}{2}\rho_2gz\right]\frac{\partial^2 v_2}{\partial z^2}+\left(a_1\mu_2-\frac{1}{2}\rho_2g\right)\frac{\partial v_2}{\partial z}=\rho_2\frac{\partial^2 v_2}{\partial t^2} \tag{10}$$

The solution of equation (10) may be taken as

$$v_2=\phi(z)e^{i(kx-\omega t)} \tag{11}$$

Equation (10) is now

$$\left[\mu_2(1+a_1z)-\frac{1}{2}\rho_2gz-\frac{P_2}{2}\right]\left[-k^2\phi\right]+\left[\mu_2(1+a_1z)-\frac{1}{2}\rho_2gz\right]\phi''+\left(a_1\mu_2-\frac{1}{2}\rho_2g\right)\phi'+\rho_2c^2k^2\phi=0$$

$$\phi''+k\left\{\frac{\frac{a_1}{k}-\frac{G}{2}}{1+k\left(\frac{a_1}{k}-\frac{G}{2}\right)z}\right\}\phi'+k^2\left[\frac{\frac{c^2}{c_2^2}-\frac{P_2}{2\mu_2}}{1+k\left(\frac{a_1}{k}-\frac{G}{2}\right)z}-1\right]\phi=0 \tag{12}$$

where $c_2^2=\frac{\mu_2}{\rho_2}$, $\omega=kc$ and $G=\frac{\rho_2 g}{\mu_2 k}$, is the Biot's gravity parameter, $\phi''=\frac{\partial^2\phi}{\partial z^2}$, $\phi'=\frac{\partial\phi}{\partial z}$.

Now we substitute, $\varphi(z)=\dfrac{\phi(z)}{\left\{1+k\left(\dfrac{a_1}{k}-\dfrac{G}{2}\right)z\right\}^{\frac{1}{2}}}$ in equation (12), we have

$$\varphi''+\left[\frac{k^2\left(\dfrac{a_1}{k}-\dfrac{G}{2}\right)^2}{4\left\{1+k\left(\dfrac{a_1}{k}-\dfrac{G}{2}\right)z\right\}^2}+k^2\left(\frac{\dfrac{c^2}{c_2^2}-\dfrac{P_2}{2\mu_2}}{1+k\left(\dfrac{a_1}{k}-\dfrac{G}{2}\right)z}-1\right)\right]\varphi=0 \tag{13}$$

Using dimensionless quantities, $\eta=-\dfrac{2\left[1+k\left(\dfrac{a_1}{k}-\dfrac{G}{2}\right)z\right]}{\left(\dfrac{a_1}{k}-\dfrac{G}{2}\right)}$

Equation (13) becomes

$$\frac{\partial^2\varphi(\eta)}{\partial\eta^2}+\left[-\frac{1}{4}+\frac{R}{\eta}+\frac{1}{4\eta^2}\right]\varphi(\eta)=0$$

$$\text{where}\quad R=-\frac{\dfrac{c^2}{c_2^2}+\dfrac{P_2}{2\mu_2}}{2\left(\dfrac{a_1}{k}-\dfrac{G}{2}\right)} \tag{14}$$

which is standard Whittaker's equation and solution is

$$\varphi(\eta)=DW_{R,0}(\eta)+EW_{-R,0}(-\eta) \tag{15a}$$

where, D and E are arbitrary constants and $W_{R,0}(\eta)$, and $W_{-R,0}(-\eta)$ are the Whittaker functions.

As the solution should vanish at $z\to\infty$, i.e. for $\eta\to-\infty$, we may take the solution as

$$\varphi(\eta)=W_{-R,0}(-\eta) \tag{15b}$$

Hence

$$v_2=\frac{EW_{-R,0}\left\{\dfrac{2\left[1+k\left(\dfrac{a_1}{k}-\dfrac{G}{2}\right)z\right]}{\left(\dfrac{a_1}{k}-\dfrac{G}{2}\right)}\right\}}{\left\{1+k\left(\dfrac{a_1}{k}-\dfrac{G}{2}\right)z\right\}^{\frac{1}{2}}}e^{i(kx-\omega t)} \tag{16}$$

Boundary Conditions and Dispersion Relation

We consider two cases

Case A: If the surface of the upper layer is rigid boundary, then

i. $v_1 = 0$ at $z = -H$

ii. $\left(\Delta f_y\right)_1 = \left(\Delta f_y\right)_2$ at $z = 0$

iii. $v_1 = v_2$ at $z = 0$

Case B: If the surface of the upper layer is traction free, then

i. $\left(\Delta f_y\right)_1 = 0$ at $z = -H$

ii. $\left(\Delta f_y\right)_1 = \left(\Delta f_y\right)_2$ at $z = 0$

iii. $v_1 = v_2$ at $z = 0$

For case A using the boundary condition (i), we have

$$Ae^{-iq_1H} + Be^{iq_1H} = 0 \text{ at } z = -H \tag{17}$$

For case B using the boundary condition (i), we have

$$Ae^{-iq_1H} - Be^{iq_1H} = 0 \text{ at } z = -H \tag{18}$$

For case A and case B using the boundary condition (ii), we have

$$L\left[iq_1A - iq_1B\right] = \mu_2 \left[\frac{d}{dz} \left(\frac{EW_{-R,0} \left\{ \frac{2\left[1 + k\left(\frac{a_1}{k} - \frac{G}{2}\right)z\right]}{\left(\frac{a_1}{k} - \frac{G}{2}\right)} \right\} e^{i(kx - \omega t)}}{\left\{1 + k\left(\frac{a_1}{k} - \frac{G}{2}\right)z\right\}^{\frac{1}{2}}} \right) \right]_{z=0} \tag{19}$$

For case A and case B using the boundary condition (iii), we have

$$A + B - E\left[W_{-R,0}(-\eta)\right]_{z=0} = 0 \tag{20}$$

Case I -In rigid boundary, eliminating A, B and E from equation (17), (19) and (20), we have

$$\begin{vmatrix} e^{-iq_1 H} & e^{iq_1 H} & 0 \\ Liq_1 & -Liq_1 & -\mu_2 \left[\frac{d}{dz} \left(\frac{W_{-R,0} \left\{ \frac{2\left[1+k\left(\frac{a}{k}-\frac{G}{2}\right)z\right]}{\left(\frac{a_1}{k}-\frac{G}{2}\right)} \right\} e^{i(kx-\omega t)}}{\left\{1+k\left(\frac{a_1}{k}-\frac{G}{2}\right)z\right\}^{\frac{1}{2}}} \right) \right]_{z=0} \\ 1 & 1 & -\left[W_{-R,0}(-\eta)\right]_{z=0} \end{vmatrix} = 0 \qquad (21)$$

Expanding the determinant, we get

$$\tan\left(\sqrt{\alpha d\left(\frac{c^2}{\beta_1^2}-\frac{1-\xi_1}{d}\right)}kH\right) = \frac{\sqrt{\alpha d\left(\frac{c^2}{\beta_1^2}-\frac{1-\xi_1}{d}\right)}\left[1-\frac{1}{8}\left\{\frac{-\left(\frac{c^2}{c_2^2}+\xi_2\right)}{\left(\frac{a_1}{k}-\frac{G}{2}\right)}+1\right\}^2\left(\frac{a_1}{k}-\frac{G}{2}\right)\right]}{\frac{L}{\mu_2}\left[\left\{1-\frac{1}{8}\left\{\frac{-\left(\frac{c^2}{c_2^2}+\xi_2\right)}{\left(\frac{a_1}{k}-\frac{G}{2}\right)}+1\right\}^2\left(\frac{a_1}{k}-\frac{G}{2}\right)\right\}\left\{\left(\frac{c^2}{c_2^2}+\xi_2\right)-\frac{1}{2}\left(\frac{a_1}{k}-\frac{G}{2}\right)-1\right\}+\frac{1}{8}\left\{\left\{1-\frac{\left(\frac{c^2}{c_2^2}+\xi_2\right)}{\left(\frac{a_1}{k}-\frac{G}{2}\right)}\right\}^2\left(\frac{a_1}{k}-\frac{G}{2}\right)^2\right\}\right]} \qquad (22)$$

where $\xi_2 = \dfrac{P_2}{2\mu_2}$

Equation (22) gives the dispersion equation of Love wave in the anisotropic porous medium of finite thickness H under a rigid boundary and overlying elastic gravitating heterogeneous half-space under initial stress.

PARTICULAR CASE

a. When, $a_1 \to 0$, ξ_1=0 and $\xi_2 = 0$, i.e. half-space becomes homogeneous under gravity, then equation (22) reduces to

b.

$$\tan\left(\sqrt{\alpha d\left(\frac{c^2}{\beta_1^2}-\frac{1}{d}\right)}kH\right) = \frac{L}{\mu_2}\left[\frac{\sqrt{\alpha d\left(\frac{c^2}{\beta_1^2}-\frac{1}{d}\right)}\left[16G+(2\frac{c^2}{c_2^2}+G)^2\right]}{\left(\frac{G}{4}-\sqrt{1-\frac{c^2}{c_2^2}}\right)\left\{16G+(2\frac{c^2}{c_2^2}+G)^2\right\}+\frac{G}{2}(2\frac{c^2}{c_2^2}+G)^2}\right] \qquad (23)$$

Which, is the result obtained by Anjana et al. (2010) for fluid-saturated porous layer under a rigid boundary and lying over an elastic half-space under gravity.

c. In case the medium is homogeneous i.e. $f = 0$ then $d = 1$,the equation (22) becomes

$$\tan\left(\sqrt{\alpha\left(\frac{c^2}{\beta_1^2}-1\right)}kH\right)=\frac{L}{\mu_2}\left[\frac{\sqrt{\alpha\left(\frac{c^2}{\beta_1^2}-1\right)}\left[16G+(2\frac{c^2}{c_2^2}+G)^2\right]}{\left(\frac{G}{4}-\sqrt{1-\frac{c^2}{c_2^2}}\right)\left\{16G+(2\frac{c^2}{c_2^2}+G)^2\right\}+\frac{G}{2}(2\frac{c^2}{c_2^2}+G)^2}\right] \tag{24}$$

This is the dispersion equation of Love waves in medium under gravity.

d. When $\alpha = 1$ i.e $L = \mu_1$, $d \to 1, a_1 = 0$ and $g \to 0$, upper layer is non-porous and lower half-space is homogeneous without gravitational force the equation (22) becomes
e.

$$\tan\left(\sqrt{\left(\frac{c^2}{\beta_1^2}-1\right)}kH\right)=\frac{\mu_1}{\mu_2}\left[\frac{\sqrt{\left(\frac{c^2}{\beta_1^2}-1\right)}}{-\sqrt{1-\frac{c^2}{c_2^2}}}\right] \tag{25}$$

This is the dispersion equation of Love waves of finite thickness homogeneous elastic layer over semi-infinite in a homogeneous isotropic half-space bounded by a rigid boundary.

Case II -In traction free boundary, eliminating A, B and E from equation (18), (19) and (20), we have

$$\begin{vmatrix} e^{-iq_1H} & -e^{iq_1H} & 0 \\ Liq_1 & -Liq_1 & -\mu_2\left[\frac{d}{dz}\left\{\frac{W_{-R,0}\left\{\frac{2\left[1+k\left(\frac{a_1}{k}-\frac{G}{2}\right)z\right]}{\left(\frac{a_1}{k}-\frac{G}{2}\right)}\right\}e^{i(kx-\omega t)}}{\left\{1+k\left(\frac{a_1}{k}-\frac{G}{2}\right)z\right\}^{\frac{1}{2}}}\right\}\right]_{z=0} \\ 1 & 1 & -\left[W_{-R,0}(-\eta)\right]_{z=0} \end{vmatrix} = 0 \tag{27}$$

Expanding the determinant, we get

$$\cot\left(\sqrt{\alpha d\left(\frac{c^2}{\beta_1^2}-\frac{1-\xi_1}{d}\right)}kH\right)= -\frac{L}{\mu_2}\frac{\sqrt{\alpha d\left(\frac{c^2}{\beta_1^2}-\frac{1-\xi_1}{d}\right)}\left[1-\frac{1}{8}\left\{\frac{-\left(\frac{c^2}{c_2^2}+\xi_2\right)}{\left(\frac{a_1}{k}-\frac{G}{2}\right)}+1\right\}^2\left(\frac{a_1}{k}-\frac{G}{2}\right)\right]}{\left[\left\{1-\frac{1}{8}\left\{\frac{-\left(\frac{c^2}{c_2^2}+\xi_2\right)}{\left(\frac{a_1}{k}-\frac{G}{2}\right)}+1\right\}^2\left(\frac{a_1}{k}-\frac{G}{2}\right)\right\}\left\{\left(\frac{c^2}{c_2^2}+\xi_2\right)-\frac{1}{2}\left(\frac{a_1}{k}-\frac{G}{2}\right)-1\right\}+\frac{1}{8}\left\{\left\{\frac{-\left(\frac{c^2}{c_2^2}+\xi_2\right)}{\left(\frac{a_1}{k}-\frac{G}{2}\right)}+1\right\}^2\left(\frac{a_1}{k}-\frac{G}{2}\right)^2\right\}\right]} \tag{28}$$

where $\xi_2=\dfrac{P_2}{2\mu_2}$

Equation (28) gives the dispersion equation of Love wave in the anisotropic porous medium of finite thickness H under traction free boundary and overlying elastic gravitating heterogeneous half-space under initial stress.

PARTICULAR CASE

When $\alpha=1$ i.e. $L\to\mu_1, d\to 1, a_1\to 0$ and $G\to 0$, upper layer is homogeneous and lower half-space is homogeneous without gravitational force the equation (27) becomes

$$\tan\left(\sqrt{\left(\frac{c^2}{\beta_1^2}-1\right)}kH\right)=\frac{\mu_2}{\mu_1}\left[\frac{\sqrt{1-\frac{c^2}{c_2^2}}}{\sqrt{\left(\frac{c^2}{\beta_1^2}-1\right)}}\right] \tag{29}$$

This is the dispersion equation of Love waves in a homogeneous isotropic half-space in the absence of rigid layer.

ANGE OF LOVE WAVE SPEED

From the equation (22), it follows that Love waves can propagate in the porous layer under initial stress overlying heterogeneous elastic half-space under gravity if

$$\beta_1\sqrt{\frac{1-\xi_1}{d}}<c<c_2 \tag{30}$$

Relation indicates the roll of initial stress and porosity of the media for the existence and non-existence of Love waves.

NUMERICAL RESULTS AND DISCUSSION

The dispersion curves of Love wave is drawn by taking $d = 0.6, \frac{c}{c_2} = 0.87, \frac{L}{\mu_2} = 2.5$ and other data from Table 1 to Table 5.

In Figure 1 and Figure 2, the phase velocity of the Love wave in absence of gravity is more than in the presence of gravity in the presence of compressive and tensile initial stress in the upper layer in case of rigid boundary. In case of traction free boundary, the phase velocity of the Love wave is same under the initial stress of the upper layer in the presence or absence of gravity.

The phase velocity of the Love waves in absence of gravity are more than in the presence of gravity without initial stress of the upper layer in rigid boundary, but in case of traction free boundary, the phase velocity of Love wave is same in the presence or absence of gravity without initial stress.

Also we observed that the phase velocity of Love waves in rigid boundary is more than traction free boundary, either upper layer is presence or absence of gravity or initial stress.

In Figure 3, the phase velocity of Love wave in absence of gravity is more than in presence of gravity in presence of heterogeneity parameter in case of rigid boundary where as in traction free boundary, the phase velocity of Love wave is same.

If the heterogeneity parameter increases, the phase velocity of Love wave increases in presence or absence of gravity under rigid where as in traction free boundary the phase velocity decreases.

In Figure 4 and Figure 5, the phase velocity of Love wave in absence of gravity parameter is more than the presence of gravity parameter under compressive and tensile stress in half-space, under rigid boundary, whereas the phase velocity of Love wave is same in case of traction free boundary.

The phase velocity of Love wave in absence of compressive and tensile stress in the half-space is more than the presence of gravity parameter under rigid boundary where as in traction free boundary, the phase velocity of Love wave is same. The phase velocity of Love wave in rigid boundary is always more than the traction free boundary in presence or absence of compressive and tensile stress in the half space.

Table 1. Parameters of Figure 1

Rigid Boundary Curve No.	Traction free Boundary Curve No	ξ_1	G
1	5	0.3	0.3
2	6	0.0	0.3
3	7	0.3	0.0
4	8	0.0	0.0

Table 2. Parameters of Figure 2

Rigid Boundary Curve No.	Traction free Boundary Curve No.	ξ_1	G
1	5	0.0	0.3
2	6	-0.3	0.3
3	7	0.0	0.0
4	8	-0.3	0.0

Table 3. Parameters of Figure 3

Rigid Boundary Curve No.	Traction free Boundary Curve No.	G	$\frac{a_1}{k}$
1	5	0.3	0.01
2	6	0.3	0.03
3	7	0.0	0.01
4	8	0.0	0.03

Table 4. Parameters of Figure 4

Rigid Boundary Curve No.	Traction free Boundary Curve No.	ξ_2	G
1	5	0.0	0.3
2	6	-0.3	0.3
3	7	0.0	0.0
4	8	-0.3	0.0

Table 5. Parameters of Figure 5

Rigid Boundary Curve No.	Traction free Boundary Curve No.	ξ_2	G
1	5	0.0	0.3
2	6	0.3	0.3
3	7	0.0	0.0
4	8	0.3	0.0

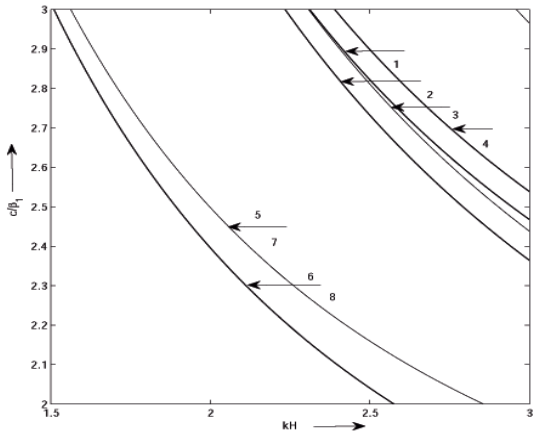

Figure 3. Variation of dimensionless phase velocity $\frac{c}{\beta_1}$ against the wave number kH for the different values of initial stress ξ_1.

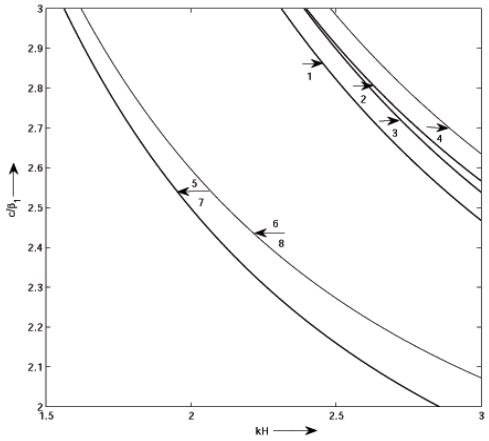

Figure 4. Variation of dimensionless phase velocity $\frac{c}{\beta_1}$ against the wave number kH for the different values of heterogeneity parameter.

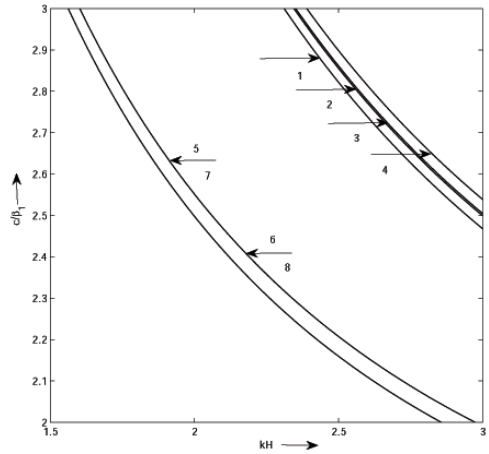

Figure 5: Variation of dimensionless phase velocity $\frac{c}{\beta_1}$ against the wave number kH for the different values of heterogeneity parameter and G

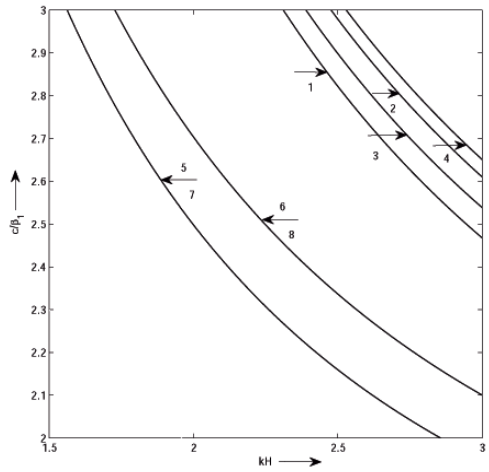

Figure 6. Variation of dimensionless phase velocity $\frac{c}{\beta_1}$ against the wave number kH for the different values of compressive initial stress ξ_2 and G.

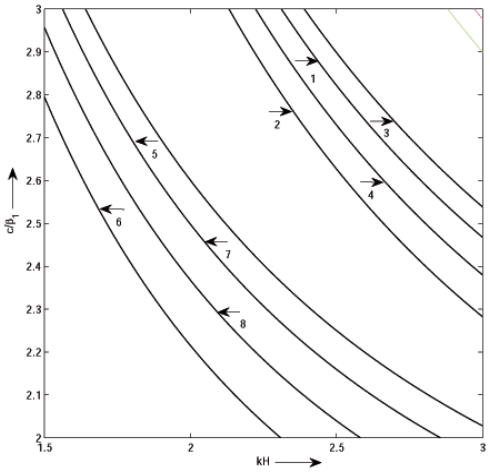

Figure 7. Variation of dimensionless phase velocity $\frac{c}{\beta_1}$ against the wave number kH for the different values of initial stress ξ_2 and G.

CONCLUSIONS

Propagation of Love waves in porous layer under initially stress over heterogeneous half-space under gravity and initially stress has been investigated analytically in rigid boundary as well as traction free boundary. The dispersion equation is obtained in both the cases. From the figures we may conclude that

1. In absence or presence of initial stresses in the half-space or layer, the phase velocity of Love waves in rigid boundary is more than the traction free boundary in presence or absence of gravity.
2. In presence of initial stress in the half-space and absence of initial stress in the layer, the phase velocities of Love wave in traction free boundary is more than the rigid boundary.
3. Initial stresses play a vital role on the propagation of Love waves in the assumed medium.
4. Gravity and heterogeneity in the half-space play a notable effect on the propagation of Love waves in the medium and half-space.

ACKNOWLEDGEMENT

The authors convey their sincere thanks to Asansol Engineering College, Asansol, Brainware Group of Institutions, Barasat and IIT(ISM), Dhanbad for providing us with its best facility.

The authors are also thankful to the reviewers for their valuable feedbacks about the paper.

CONFLICT OF INTEREST

The authors are stated that there is no conflict of interest between them.

REFERENCES

Abd-alla, A. M. and Ahmed,S. M. ,1999. Propagation of Love waves in a non-homogeneous orthotropic astic layer under initial stress overlying semi-infinite medium. *Applied Mathematics and Computation*,106(2),449-460.

Anjana, P.G., Samal, S.K. and Mahanti, S.K, 2010. Love waves in a fluid-saturated porous layer under a rigid boundary and lying over an elastic half-space under gravity. *Applied Mathematical Modeling*, 34, 1873-1883.

Biot M.A., 1956, Theory of deformation of a porous viscoelastic anisotropic solid, *Journal of Applied Physics* 27: 459-467.

Biot M.A., 1956, Theory of propagation of elastic waves in fluid saturated porous solid, *Journal of the Acoustical Society of America* 28: 168-178.

Bacigalupo, A., Gambarotta, L., 2014. Second-gradient homogenized model for wave propagation in heterogeneous periodic media. *Int. J. Solids Struct.* 51, 1052–1065.

Chakraborty, M., Chattopadhyay, A. and Dey, S.,1983. The effects of initial stress and irregularity on the propagation of SH-waves. *Indian J. pure appl. Math.*,14(7),850-863.

Chakraborty, S.K. and Dey, S., 1981. Love waves in dissipative media under gravity. Garlands Beitragezur Geophysik. 9096 ,521-528.

Chattaraj, R., Samal, S.K., Mahanti, N., 2013. Dispersion of Love wave propagating in irregular anisotropic porous stratum under initial stress. *Int. J. Geomech.* 13 (4),402-408.

Chattopadhyay, A. and Kar, B.K., 1978.On the dispersion curves of Love type waves in an initially stressed crustal layer having an irregular interface. *Geophysical Research Bullentin*,16(1),13-23.

Dey, S., Gupta, S.,Gupta, A.K., 1996. Propagation of Love waves in heterogeneous crust over a heterogeneous mantle. *J. ActaGeophys. Pol.* Poland XLIX (2), 125–137.

Dey, S., Gupta, S., Gupta, A.K., 2004. Propagation of Love waves in an elastic layer with void pores. Sadhana 29, 355–363.

Gupta, S., Majhi, D.K., Kundu, S., Vishwakarma, S.K., 2013a. Propagation of Love waves in non-homogeneous substratum over initially stressed heterogeneous half-space. *Appl. Math. Mech. Engl.* Ed. 34 (2), 249–258.

Gupta, S., Chattopadhyay, A., Majhi, D.K., 2010b. Effect of initial stress on propagation of Love waves in an anisotropic porous layer. J. Solid Mech. 2 (1), 50–62.

Kalyani, V.K., Sinha, A., Pallavika, Chakraborty, S.K., Mahanti, N.C., 2008, Finite difference modeling of seismic wave propagation in monoclinic media. *Acta Geophys.* 56 (4), 1074–1089.

Kundu, S., Gupta, S., Manna, S., 2013. SH-type waves dispersion in an isotropic medium sandwiched between an initially stressed orthotropic and heterogeneous semi-infinite media. *Meccanica.* http://dx.doi.org/10.1007/ s11012-013-9825-5.

Kundu, S., Gupta, S., Manna, S., 2014. Propagation of Love wave in fiber-reinforced medium lying over an initially stressed orthotropic half-space. *Int. J. Numer. Anal. Methods Geomech.* http://dx.doi.org/10.1002/nag.2254.

Manna, S., Kundu, S., Gupta, S., 2013. Love wave propagation in a piezoelectric layer overlying in an inhomogeneous elastic half-space. J. Vib. Control. http://dx.doi.org/10.1177/1077546313513626.

Pal, P.C., Sen, B., 2011. Disturbance of SH-type waves due to shearing-stress discontinuity in a visco-elastic layered half-space. *Int. J. Mech. Solids* 6 (2), 176-189.

Pradhan, A., Samal, S.K., Mahanti, N.C., 2003. The Influence of anisotropy on the Love waves in a self-reinforced medium. *Tamkang J. Sci. Eng.* 6 (3), 173-178.

Sharma, M.D., 2004. Wave propagation in a general anisotropic poro-elastic medium with anisotropic permeability: phase velocity and attenuation. *Int. J. Solids Struct.* 41, 4587-4597.

APPENDIX-I

Derivation from equation (2)-(3):

$$(N-\frac{P_1}{2})\frac{\partial^2 v}{\partial x^2}+L\frac{\partial^2 v}{\partial z^2}=\frac{\partial^2}{\partial t^2}\left[\rho_{11}v+\rho_{12}V\right] \text{ and}$$
$$\frac{\partial^2}{\partial t^2}\left[\rho_{12}v+\rho_{22}V\right]=0 \qquad (2)$$

Let $d_2=[\rho_{12}v+\rho_{22}V]$, then $V=(d_2-\rho_{12}v)/\rho_{22}$

Hence $d_1=\rho_{11}-\frac{{\rho_{12}}^2}{\rho_{22}}$

Therefore,

$$(N-\frac{P_1}{2})\frac{\partial^2 v}{\partial x^2}+L\frac{\partial^2 v}{\partial z^2}=d_1\frac{\partial^2 v}{\partial t^2}$$

(3)

Where, $\frac{\partial^2}{\partial t^2}\left[\frac{\rho_{12}d_2}{\rho_{22}}\right]=0$, since $\frac{\rho_{12}d_2}{\rho_{22}}$ is a constant term.

APPENDIX –II

Derivation of equation (10):

we have

$$\frac{\partial S_{12}}{\partial x}+\frac{\partial S_{22}}{\partial y}+\frac{\partial S_{23}}{\partial z}-\rho g\omega_{23}+\rho gz\frac{\partial \omega_{12}}{\partial x}-\rho gz\frac{\partial \omega_{23}}{\partial z}-\frac{P_2}{2}\frac{\partial v}{\partial x^2}=\rho\frac{\partial^2 v_2}{\partial t^2} \qquad (8)$$

$$S_{12}=2\mu e_{xy},\ S_{23}=2\mu e_{yz},\ e_{ij}=\frac{1}{2}\left(\frac{\partial u_i}{\partial x_j}+\frac{\partial u_j}{\partial x_i}\right),\ e_{xy}=\tfrac{1}{2}\left(\frac{\partial v_1}{\partial y}+\frac{\partial v_2}{\partial x}\right),\ e_{yz}=\tfrac{1}{2}\left(\frac{\partial v_2}{\partial z}+\frac{\partial v_3}{\partial y}\right)$$

In this problem $\frac{\partial}{\partial y}=0$ and $\mu=\mu_2(1+a_1z)$, $\rho=\rho_2$, the stress strain relation becomes

$$e_{xy} = \tfrac{1}{2}\frac{\partial v_2}{\partial x}, \quad e_{yz} = \frac{1}{2}\frac{\partial v_2}{\partial z}$$

$$S_{12} = \mu_2\left(1+a_1 z\right)\frac{\partial v_2}{\partial x}, \quad S_{23} = \mu_2\left(1+a_1 z\right)\frac{\partial v_2}{\partial z}, \frac{\partial S_{12}}{\partial x} = \mu_2\left(1+a_1 z\right)\frac{\partial^2 v_2}{\partial x^2} \tag{9}$$

$$\frac{\partial S_{23}}{\partial x} = \mu_2\left(1+a_1 z\right)\frac{\partial^2 v_2}{\partial z^2} + a_1\mu_2\frac{\partial v_2}{\partial z}, \frac{\partial w_{12}}{\partial x} = -\frac{1}{2}\frac{\partial^2 v_2}{\partial x^2}, \frac{\partial w_{12}}{\partial x} = \frac{1}{2}\frac{\partial^2 v_2}{\partial z^2}$$

where, μ is the modulus of rigidity, a_1 is a variation parameter of a rigidity having dimension inverse of length.

.

Equation (8) using the above relations takes the form

$$\left[\mu_2\left(1+a_1 z\right) - \frac{1}{2}\rho_2 g z - \frac{P_2}{2}\right]\frac{\partial^2 v_2}{\partial x^2} + \left[\mu_2\left(1+a_1 z\right) - \frac{1}{2}\rho_2 g z\right]\frac{\partial^2 v_2}{\partial z^2} + \left(a_1\mu_2 - \frac{1}{2}\rho_2 g\right)\frac{\partial v_2}{\partial z} = \rho_2\frac{\partial^2 v_2}{\partial t^2} \tag{10}$$

Original paper

https://doi.org/10.22201/igeof.00167169p.2021.60.3.1920

New Semi-Quantitative Approach for Interpreting Vertical Electrical Sounding (VES) Measurements – Using a Fractal Modeling Technique, Case Study from Khanasser Valley, Northern Syria

Jamal Asfahani[1*]

Received: January 14, 2019; accepted: April 12, 2021; published online: July 1, 2021.

Resumen

Se propone una nueva técnica de modelado fractal, adaptando el modelo de concentración-número (*C-N*, según sus siglas en inglés) y el concepto de puntos de ruptura de umbral para interpretar las medidas de sondeo eléctrico vertical (VES, según sus siglas en inglés) distribuidas a lo largo de un perfil dado. En consecuencia, se propone un enfoque semicuantitativo para diferenciar fácilmente entre diversas poblaciones de resistividad aparente, donde se podría construir una interpretación semicuantitativa bidimensional (2D) y un análisis geológico preliminar. La nueva técnica se aplicó en un estudio de caso de la región del valle de Khanasser, norte de Siria, donde se interpretaron diferentes perfiles (*LP1, LP2, LP3* y *TP5*). La idoneidad y viabilidad del enfoque propuesto se confirman y aprueban a través de diferentes comparaciones entre las secciones transversales establecidas de múltiples fractales y los modelos de interpretación VES unidimensionales (1D) tradicionales. Se recomienda utilizar de forma rutinaria este nuevo enfoque fractal propuesto en la investigación geoeléctrica para interpretar las mediciones de VES distribuidas a lo largo de un perfil determinado.

Palabras clave: Modelado fractal, modelo de concentración-número (C-N), técnica VES, Khanasser Valley, Siria.

Abstract

A new fractal modeling technique, adapting the concentration-number (*C-N*) model and the threshold break points concept is proposed to interpret vertical electrical sounding (VES) measurements distributed along a given profile. A new semi-quantitative approach is consequently proposed to readily differentiate between different apparent resistivity populations, where two-dimensional (2D) semi-quantitative interpretation and a preliminary geological analysis could be constructed. The new technique is applied and tested on a case study from the Khanasser Valley region, Northern Syria, where different selected profiles (*LP1, LP2, LP3, and TP5*) are interpreted. The suitability and feasibility of the proposed approach are confirmed and approved through different comparisons between the multi-fractal established cross-sections and the traditional one-dimensional (1D) VES interpretation models. It is recommended to routinely use this new proposed fractal approach in geoelectrical research for interpreting VES measurements distributed along a given profile.

Key words: Fractal modeling, Concentration-Number (C-N) model, VES technique, Khanasser Valley, Syria.

**Corresponding author: cscientific3@aec.org.sy*
[1] Geology Department
Atomic Energy Commission of Syria
P.O.Box. 6091, Damascus- Syria

INTRODUCTION

Electrical resistivity investigation techniques are extensively used for several applications, among others, water exploration to search suitable groundwater sources or groundwater pollution, engineering prospection to locate sub-surface faults, fissures and cavities, permafrost, etc, and archaeological mapping to define the extension of buried formations or ancient buildings (Reynolds, 2011). They are used in those fields to obtain detailed information readily and economically about the location, depth, and resistivity of subsurface formations. Those electrical resistivity techniques applied on the surface have proved to successfuly delineate the subsurface geology and structures (Olasehinde, *et al.*, 2013).

The traditional Vertical Electrical Sounding (VES) with Schlumberger configuration is an effective electrical resistivity surveying technique for groundwater exploration (Edwards, 1977 and Zohdy *et al.*, 1984).

The one-dimensional (1D) quantitative interpretation of the VES measurements allows the real resistivities and thicknesses to be determined under every studied VES point (Zohdy and Bisdorf, 1989). The two-dimensional (2D) qualitative VES interpretations are mainly oriented towards establishing the geoelectrical section and analyzing the resistivity variations along a given profile laterally and vertically, where the 1D quantitative VES results are used for such a 2D interpretation. Establishing a 2D interpretation analysis is not an easy task, because every VES point is solely 1D interpreted without considering the effect of other surrounding VES. In those conditions, the 2D interpretations along a given VES profile strongly depend on the experience of the geo-scientist and his geological knowledge of the study region. Such a weakness prevents giving an accurate and integrated subsurface geoelectrical picture, particularly in geologically complex areas, and in the area between the interpreted VES along the studied profile.

The Pichgin and Habibulleav method (1985) enhanced by Asfahani and Radwan (2007) is one of the elaborated mathematical techniques for interpreting VES measurements distributed along a given profile in terms of a two-dimensional model (2D). It has been successfully applied in Syria for solving different structural subsurface problems related to groundwater (Asfahani and Radwan, 2007), and in geo-exploration mining such as phosphate, uranium, sulfur, and bitumen (Asfahani, 2010; Asfahani, 2011). This 2D method has been recently applied by Al-Fares and Asfahani (2018) for solving the Abou Barra leakage dam problem in Northern Syria. It was also applied in the Arbil region for environmental and groundwater contaminations studies (Gardi and Asfahani, 2018). This 2D technique is oriented towards determining in detail the structural subsurface along a given VES profile.

A new procedure for the interpretation of VES data with the use of a 1.5D simultaneous inversion method was proposed by Gyulai and Ormos in 1999. The basic idea of their method showed that the horizontal changes in the layer thicknesses and the resistivities of the 2D geological structure can be described by (expanding in series) functions of spatial coordinates. The coefficients of the basis functions are determined from the VES data by a simultaneous inversion method using a least-squares technique.

A quick 2D geoelectric inversion method using series expansion was also proposed by Gyulai *et al.*, 2010. They indicated that horizontal changes in the layer-thicknesses and resistivities of the geological structure are discretized in the form of series expansion. The linearized iterative least-squares (LSQ) inversion of data provided by surface geoelectric measurements determines the unknown expansion coefficients. The discretization of the 2D model using series expansion gives the possibility to reduce the number of model parameters. The resulting inverse problem

becomes consequently over-determined and can be solved without the application of additional regularization.

A combined geoelectric weighted inversion was proposed by Gyulai *et al*., 2014 for interpreting VES data for environmental exploration purposes. The 2D combined geoelectric inversion (CGI) method performs more accurate parameter estimation than conventional 1D single inversion methods by efficiently decreasing the number of unknowns of the inverse problem (single means that data sets of individual vertical electric sounding stations are inverted separately).

Gyulai *et al*., 2016 used 2.5D CGWI combined geoelectric weighted inversion of VES measurements for characterizing geoelectrically the thermal water aquifers. According to their technique, which uses the joint 2D forward modeling of dip and strike direction data, the 3D structures can be determined.

A new geoelectrical combined sounding-profiling configuration was recently adapted and proposed for increasing the resolution of 1D VES quantitative interpretations (Asfahani, 2018). The electrode *C* in this new proposed three-electrode array is not fixed at the infinity but is slightly modified and movable, where $OA=OB=OC=AB/2$ as shown and presented in Figure 1. It allows to gain a maximum of geoelectrical information when ϱ_{AB} gradient transformation and $\varrho_{AC}/\varrho_{BC}$ are integrally interpreted, to get an accurate subsurface resistivity picture along a given profile.

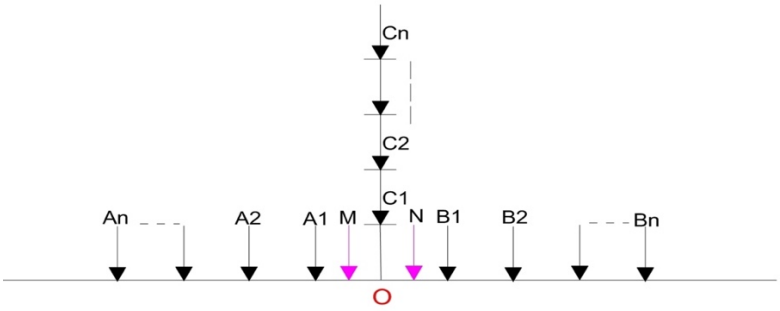

Figure 1. Schema of the combined sounding- profiling configuration (two three electrode configurations AMN and MNB). A, B and C: current electrodes, M and N: potential electrodes, O: configuration center (Asfahani, 2018).

The geo-electric surveys have been carried out in the Khanasser valley in Northern Syria for hydro-geological purposes to solve different posed problems in the study region. The VES technique applied in this survey is oriented to provide information concerning the thickness of subsurface layers, geological structures, contributing groundwater occurrence, and to follow the lateral and vertical variations of subsurface layers. Those VES measurements have been carried out during an international cooperation program, which has been established between three scientific organizations; ICARDA, AECS, and Bonne university (Schweers *et al.,* 2002). The objectives of this program have been designed to address the typical problems characterizing the marginal dry-land environments. The poverty, the relatively easy accessibility, and the diversity and dynamics of the natural resources and livelihoods made Khanasser valley region a prime candidate.

The present paper discusses an application of the geoelectrical survey using Schlumberger VES technique, oriented towards clarifying and identifying the subsurface resistivity variations in terms of a 2D semi-quantitative interpretation along a given profile.

A fractal modeling technique adapting the concentration- number (*C-N*) model is proposed herein as a new approach to interpreting the geoelectrical VES measurements carried out along a given profile. It is worth mentioning that the same fractal modeling technique (*C-N*) was recently applied for characterizing the basalt environments in Southern Syria, where different geological scenarios have been established and proposed to explain the basalt distributions along different profiles in the study region (Asfahani and Al-Fares, 2021).

Different geoelectrical profiles (*LP1, LP2, LP3, and TP5*) are selected from the study Khanasser valley region (Fig. 2 and Fig.3), and re-interpreted by using this new fractal approach.

The fractal and multifractal models developed by Mandelbrot (1983) are widely used in different branches of geosciences. Those models are used for example in geophysical exploration for the separation of geophysical anomalies from background. Fractal dimensions of variations in geophysical resistivity data can therefore provide useful information and applicable criteria to identify and categorize different lithological zones within the studied profiles. The log-log plots are suitable to distinguish between different resistivity populations, and make a kind of classification in the geoelectrical data. In fact, the threshold values determined can be identified and delineated as break points in those log-log plots. A break point located and determined in the log-log plot reflects a lithological change and the passage from a lithology to a different one. The determination of those points makes the fractal C-N model more precise, being very sensitive to the lithological boundary location.

The concentration-number (*C-N*) fractal model is applied and newly introduced in this paper to distinguish between different resistivity populations, and give a range of resistivity values for each of them. Such a new application makes the unclear apparent resistivity values obtained as a function of depth (*AB/2*) to a clearer litho-resistivity populations, easily explained and documented along a given profile.

In this way, a semi-quantitative technique is proposed herein for interpreting the resistivity variations with depth using the VES technique along a given profile.

The main objectives of this paper are therefore constructed to be as follows:

1) Carrying out VES measurements distributed along given profiles with Schlumberger array.
2) Proposing the fractal modeling technique as a new approach to interpret VES measurements carried out along a given profile.
3) Interpreting the measured VES data points by using the new proposed approach and the 2D concentration-number (*C-N*) fractal model with the log-log plots, to get a kind of litho-resistivity pseudo section for the VES measurements distributed along a given profile.
4) Comparing the VES results obtained by the fractal modeling with other traditional geoelectrical interpretations.

HYDROGEOLOGY OF THE KHANASSER VALLEY

Khanasser Valley is located approximately 70 km southeast of Aleppo City, and lies between two hill ranges; the Jabal Shbeith eastwards and the Jabal Al Hoss westwards. The southern part drains towards the Adami depression in the south, while the northern part of the valley drains towards the Jaboul Salt Lake (Figs. 2 and 3).

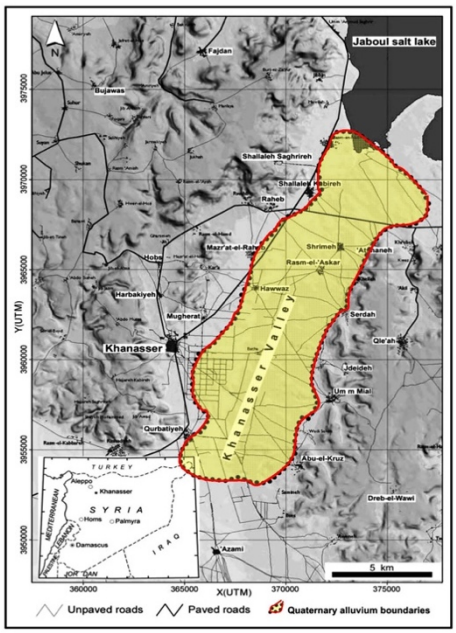

Figure 2. Location of the Khanasser valley, Northern Syria.

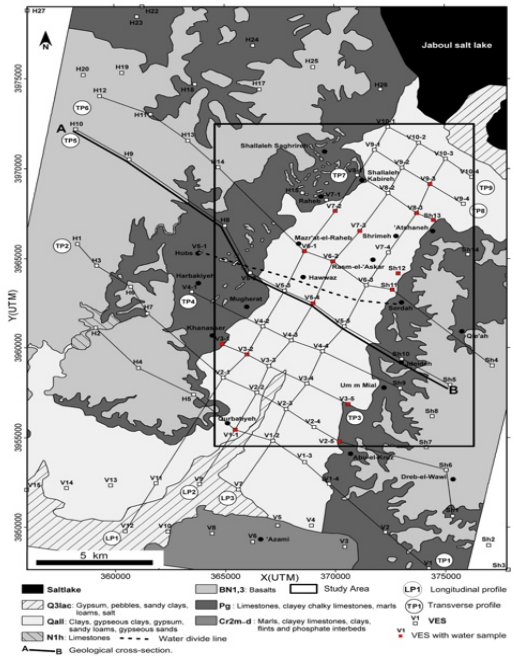

Figure 3. Locations of the VES measurements in the Khanasser Valley and its surrounding area.

Three aquifers are used in the Khanasser Valley for groundwater extraction. The deepest is of upper Cretaceous age at 400 m below ground level. Above the Maestrichtian, the Paleocene-Lower Eocene limestone aquifer of low productivity is located (ACSAD, 1984), where the average hydraulic conductivity (*k*) as referred from the pumping test is 0.0054 m/day (Schweers *et al*., 2002). Lengiprovodkhoz (1987) had previously registered a hydraulic conductivity ranging between 0.008 m/day and 0.5 m/day for the Paleogene formation. The paleogene strata in the central part of Khanasser valley are not very thick; about 50 m of lower Eocene and Paleocene

overlay the Maastrichtian. Quaternary water-bearing formations, the most transmissive in the region situated near the surface, are covered by some of 10 m of alluvial and proluvial soil. This aquifer receives direct recharge from rainwater as well as infiltrating runoff and subsurface flow from the slopes of Jabal Al Hoss and Jabal Shbeith. Electrical conductivities of groundwater in this aquifer vary between 2.5 and 26 dS/m, (Schweers *et al.*, 2002).

Figure 4 shows a geological section of NW-SE orientation from Jabal. Al Hoss to Jabal. Shbeith passing through Khanasser Valley, in which the different geological formations with their stratigraphic units are presented.

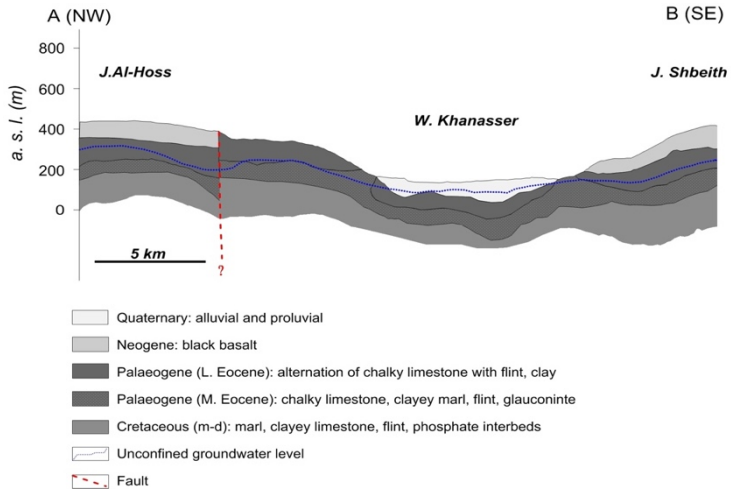

Figure 4. Geological section of NW-SE orientation from Jabal.Al Hoss to Jabal.Shbeith passing by Khanasser Valley.

The rapid development of mechanical irrigation wells during the last two decades has led to a substantial increase in groundwater withdrawal from the upper, unconfined aquifer system. The groundwater monitoring and analysis indicate that the valley may be affected by salt water intrusion from the Jaboul Salt Lake, where variable changes in water level and quality are observed since 1998 (Hoogeveen and Zobisch, 1999; Asfahani and Abo Zakhem, 2013). Rainfall is comprised between 200 and 250 mm/year and is not predictable, while the natural resources are quite poor and prone to degradation.

Vertical Electrical Soundings (VES)

VES technique requires to impose an electrical current on the study area by a pair of A and B electrodes at varying spacing expanding symmetrically from a central point, and to measure the surface expression of the resulting potential field with an additional pair of M and N electrodes at appropriate spacings.

The apparent resistivity (ρa) is expressed by the following equation:

$$\rho a = \frac{2\pi}{\frac{1}{AM} - \frac{1}{BM} - \frac{1}{AN} + \frac{1}{BN}} \frac{\Delta V}{I} \quad (1)$$

Where I is the current introduced into the earth by A and B electrodes, and ΔV is the potential measured between the potential electrodes M and N, as shown in Fig. 5.

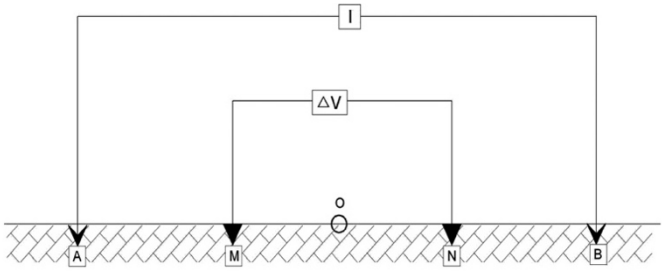

Figure 5. Schlumberger array in the field.

The electrical (VES) sounding gives an estimate of the variation of the electrical resistivity with the depth below a given point on the earth surface. Fig. 6 shows the field resistivity curve measured at point V10-4, which plotting the apparent resistivity values (ϱa), obtained by increasing the electrode spacing $(AB/2)$ about a fixed VES point (ϱa= f ($AB/2$)).

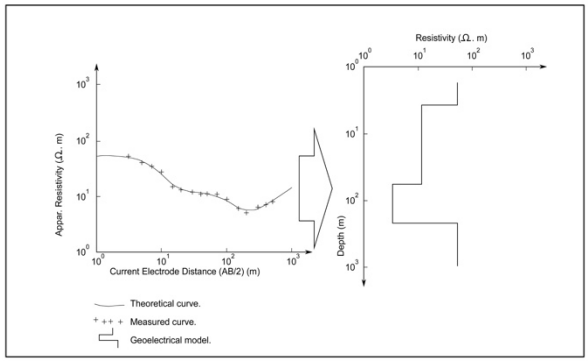

Figure 6. Field VES curve and its interpretation at point V10-4.

The field apparent resistivity curve is interpreted using a curve matching technique of master curves (Orellana and Mooney, 1966), where an initial approximate model of thicknesses and resistivities of corresponding layers is obtained. This approximate model is thereafter accurately interpreted with an inverse technique program until reaching acceptable goodness of fit between the field resistivity curve and the theoretical regenerated curve (Zohdy, 1989, Zohdy and Bisdorf, 1989).

FIELD SURVEY

An Indian equipment (ACR-1) has been used to survey ninety-six VES points in the study region, distributed on a grid including three longitudinal profiles labeled as *LP1, LP2, and LP3,* and nine transverse profiles oriented approximately NW–SE (Fig. 3) and labeled as (*TP1, TP2, TP9*). The resistance $(\Delta V/I)$ is directly measured by the ACR-1, and the apparent resistivity (ϱa) is consequently estimated according to equation [1] (Dobrin, 1976). The distance between profiles is approximately 1 km, where a VES point is generally measured every kilometer along each profile (especially in the valley itself). This distance observation interval is sometimes changed according to the topographic conditions. The geo-electrical lines for all the VES executed in the study area have been chosen to be parallel to the direction of Khanasser valley axis of N301E. Schlumberger array was applied to carry out those ninety-six VES measurements, for which a maximum current electrode spacing ($AB/2$ = 500 m) of 1000 m was used.

FRACTAL THEORY

Mandelbrot (1983) has already proposed the fractal geometry with its different models, as a nonlinear mathematical science, to be extensively practiced in many branches of earth sciences. Different applications of 2D and 3D geophysical data have been carried out by using several fractal-multifractal models, which have been recently proposed, such as concentration-number (*C-N*) (Hassanpour and Afzal, 2013), concentration-distance (*C-D*) (Li *et al.*, 2003), and concentration-volume (*C-V*) (Afzal *et al.*, 2011).The application of the fractal models requires the use of log-log plots, in which the straight line segments fitted to the log-log graph have some break threshold points (Zuo, 2011; Wang *et al.*, 2011; Mohammadi *et al.*, 2013). Every straight line segment determined on the log-log plots reflects a specific geophysical population, that we have to evaluate its variation range.

The (C-N) multifractal model is proposed in this paper as a new application approach for interpreting the VES measurements distributed along a given profile, and explaining its resistivity variations with depth through differentiating between different resistivity ranges. The concentration-number (*C-N*) fractal model is expressed by the following equation:

$$N(\geq \varrho) = F\varrho^{-D} \tag{2}$$

Where ϱ denotes the treated geoelectrical parameter values. The geoelectrical parameter used in this paper is the apparent resistivity (Ω.m). $N(\geq\varrho)$ denotes the cumulative number of the apparent resistivity data ($A\varrho$), with the resistivity parameter values greater than or equal to ϱ, F is a constant and D is the scaling exponent or fractal dimension of the distribution of electrical resistivity parameter values.

RESULTS AND DISCUSSION

The ninety-six (VES) measurements carried out in the Khanasser Valley have been firstly 1D interpreted by using the master curves, where an initial approximate model with resistivities and thickness of corresponding layers are reached (Asfahani, 2007). The reached approximate model is secondly interpreted by an inversion resistivity program for getting correctly the final optimum theoretical curve, that fits as best as possible with the measured apparent resistivity data. The geological layers in the field in such a 1D quantitative interpretation are assumed to be horizontal (Asfahani, 2007). Fig.6 shows an example of field VES curve obtained at the point V10-4 and its interpretative model solution. The ninety six (VES) measured points were distributed on twelve profiles as shown in Fig. 3 and interpreted with the assumption of *1D* structure (Asfahani, 2007). Three of those profiles are longitudinal, labeled *LP1, LP2* and *LP3* and carried out in the Khanasser valley itself, while the other nine are transverse and labeled *TP1, TP2,* and *TP9*. The thickness and resistivity parameters of the Quaternary and Paleogene deposits are quantitatively evaluated through interpreting those ninety six measured (VES) points (Asfahani, 2007). The Quaternary deposits thickness varies between a minimum of 4.5m and 99.4m with an average of 38.5 m. Its resistivity varies between 4.1 and 43 Ω.m with an average of 15.3 Ω.m. The Paleogene thickness varies between a minimum of 54m and a maximum of 283m, with an average of 162.4 m. Its resistivity varies between 1.7 and 16 Ω.m with an average of 5.1 Ω.m (Asfahani, 2007).

The Pichgin and Habibullaev (1985) method has been already applied for interpreting the VES soundings distributed along the mentioned longitudinal and transverse profiles in term of 2D modeling (Asfahani and Radwan, 2007). This 2D interpretation modelings have already allowed to get detailed subsurface images about the studied profiles. Fig. 7 shows an example on using this 2D technique for interpreting *LP2* profile. According to this technique, the subsurface tectonic fractured zones, and the geological structural features for all the *AB/2* spacings have been defined along *LP2* profile.

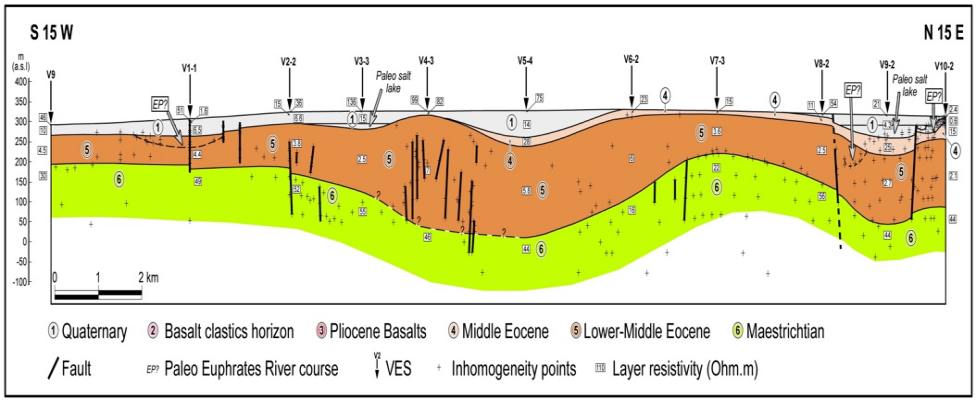

Figure 7. Interpretative 2D model of LP2 profile according to Pichgin and Habibeleave technique.

The results of this interpretative method as previously explained (Asfahani, 2007; Asfahani, 2010) are presented by the points of nonhomogeneity (+), which mainly show the locations of fractured zones as shown under the V4-3 and V5-4 soundings, and under the V8-2 and V10-2 soundings. The distribution of these points in regular form of bedding planes as shown between the V8-2 and V6-2 soundings reflects the geological structure of the study area. It is evident that the Maastrichtian formation is remarkably uplifted. The effect of the Quaternary paleo-sabkhas discussed previously is also shown under the V10-2 in the north. Other similar tectonic subsurface features have also been traced through the analysis of the other two measured profiles *LP1* and *LP3* (Asfahani, 2007).

The three longitudinal profiles *LP1*, *LP2*, and *LP3* and the transverse *TP5* profile are studied, analyzed, and re-interpreted in this paper, by applying the proposed multifractal (*C-N*) modeling technique. The application of the multifractal modeling technique is considered as a new approach for getting a semi-quantitative interpretation for the VES soundings distributed along a given profile. It allows having a preliminary idea about the number of apparent resistivity populations, present along the studied profile.

The *LP1* profile of length of 23.77 Km includes eleven VES measured points, for which the resistivity variations as a function of *AB/2* varying from 3 to 500 m are analyzed and interpreted by the use of fractal concentration-number (*C-N*) model. Based on the *C-N* log-log plot presented in (Fig.8) for *LP1* profile, the 176 data points of apparent resistivity *ϱa* for all the *AB/2* (from 3 to 500 m) show three threshold break points C1, C2, and C3 at 1, 1.16, and 1.36 respectively. The log (*ϱa*) values indicate an apparent resistivity of 10, 14 and 23Ω.m respectively.

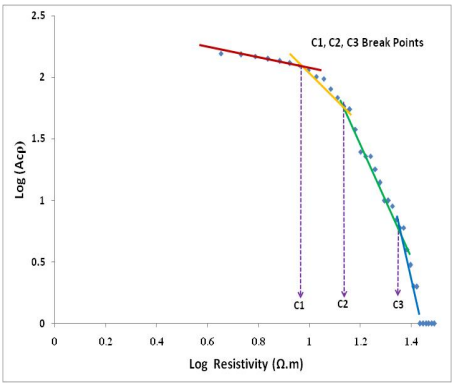

Figure 8. Fractal C-N log-log plot for the measured apparent resistivity data along LP1 profile.

The log-log plots of Acρ as a function of the apparent resistivity values show the scattered data points, which can be fitted by several straight lines (segments) with different slopes based on a least square regression. The selection of the break points as threshold values is an objective decision since apparent resistivity populations are addressed by different line segments in the *C-N* log-log plots. The intensity of various populations is depicted by each slope of the line segment in the *C-N* log-log plots.

Those three break points correspond to four apparent resistivity ranges as follows: the first range is less than 10 Ω.m, the second range is between 10 and 14 Ω.m, the third range is between 14 and 23 Ω.m, and the fourth range is bigger than 23 Ω.m. The use of those resistivity ranges allows the establishment of the apparent resistivity cross section along *LP1* profile as shown in Fig. 9B. The distinction between those four resistivity populations is clear, where every resistivity population is due to a distinct and specific lithology. The boundaries between those resistivity ranges also emphasize indirectly the lithologic type distribution along the studied profile. Geological interpretation about the lithology and the resistivity population could be easily done along the studied *LP1* profile. By such a manner, a semi quantitative 2D interpretation could be achieved. The traditional iso-apparent resistivity map is established as a function of *AB/2* along the *LP1* profile as shown in Fig.9A. The distance in kilometer along *LP1* profile is represented linearly, while the depth of *AB/2* in meter is represented with a negative sign in a logarithmic scale to get an acceptable concordance between the two axes (distance and depth). The scale of *AB/2* being logarithmic, the corresponding *AB/2* of -3, -4.3, -5.2, -6.15, -7.25, -8.1, -9.1, -9.9, -10.5, -11.4, -12.3, -13.4, -14.2, -15.3, -16.1, and -16.7 are used instead of *AB/2* of 3, 5,7, 10, 15, 20, 30, 40, 50, 70, 100, 150, 200, 300, 400, and 500 m, respectively.

The iso-apparent resistivity map shown in Fig.9A is difficult to be qualitatively interpreted, compared with that obtained by applying the multi-fractal approach (Fig.9B). It is worth mentioning that an acceptable coincidence is obtained between the multi-fractal established apparent resistivity cross-section along *LP1* profile (Fig.9B) and the traditional 1D quantitative interpretation along this *LP1* profile, as shown in the figure 9C (Asfahani, 2007). The VES sounding at V6-1 point for example shows four resistivity populations from up to down. The first one is related to the resistivity range of bigger than 23 Ω.m, and reflects the superficial layer. The second range of between 10 and 14 Ω.m, and the third range of between 14 and 23 Ω.m represent the Quaternary deposit, separated in this V6-1 point into two distinguished layers. The first resistivity range of less than 10 Ω.m indicates to the Paleogene presence. This V6-1 point was 1D quantitatively interpreted adapting a model of 5 layers (Asfahani, 2007). The resistivity of the first superficial layer is 26.8 Ω.m and its thickness is 3.7m. The second layer has a resistivity of 8.5 Ω.m and a thickness of 34.7 m; The third layer has a resistivity of 25.8 Ω.m and a thickness of 49.4 m, and both of them are of Quaternary deposit with different resistivities. The fourth layer related to the Paleogene has a resistivity of 5.7 Ω.m and a thickness of 226 m. The fifth layer is related to the Maastrichtian and has a resistivity of 51 Ω.m. This quantitative described model for V6-1 has been completely indicated, shown, and confirmed by the fractal concentration–number model, where a good coincidence is obtained between the two different interpretative approaches.

The Paleogene is shown near the surface at V7-1 directly after the superficial layer of a resistivity of 16 Ω.m and thickness of 6 m.

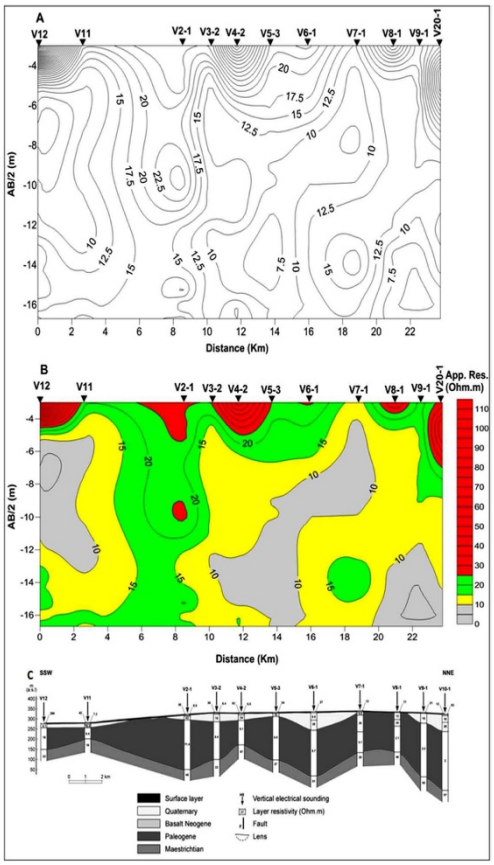

Figure 9 A: Traditional iso-apparent resistivity cross section along LP1 profile. B: Concentration-number fractal model along LP1 profile. C: Traditional 1D quantitative geoelectrical model along LP1(Asfahani, 2007).

The application of the proposed fractal (*C-N*) approach on the 192 apparent resistivity data points related to *LP2* profile shows three threshold break points of C1, C2, and C3 at 0.78, 1.16, and 1.39 respectively as presented in (Fig.10). The log (*ρa*) values indicate an apparent resistivity of 6, 14 and 24 Ω.m, respectively. Those three break points correspond to four apparent resistivity ranges as follows; the first range is less than 6 Ω.m, the second range is between 6 and 14 Ω.m, the third range is between 14 and 24 Ω.m, and the fourth range is bigger than 24 Ω.m. The established apparent resistivity cross-section along *LP2* profile is illustrated in Fig.11B.

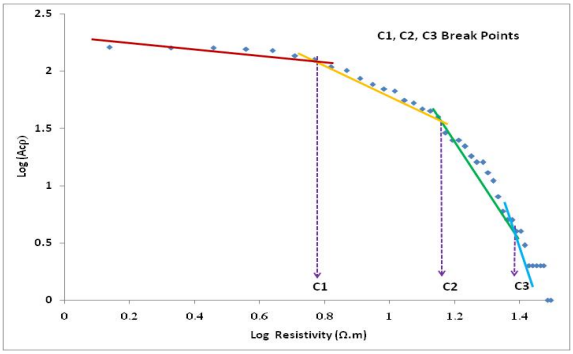

Figure 10. Fractal C-N log-log plot for the measured apparent resistivity data along LP2 profile.

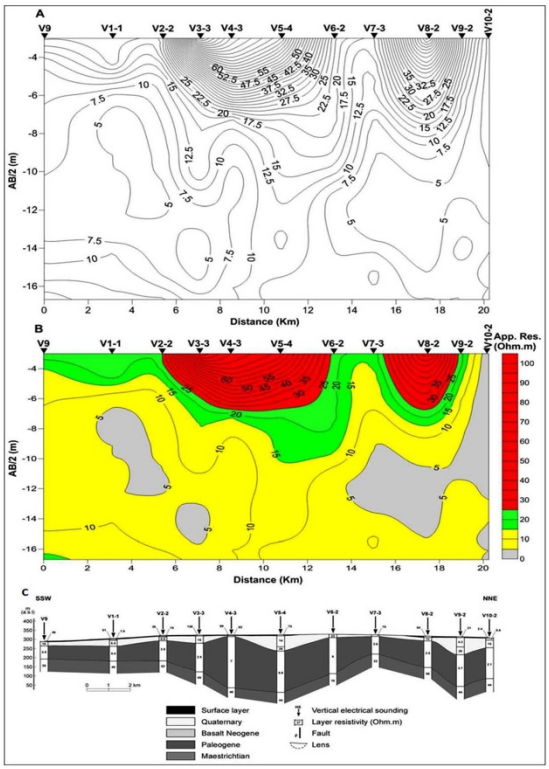

Figure 11 A. Traditional iso-apparent resistivity cross section along LP2 profile. B: Concentration-number fractal model along LP2 profile. C: Traditional quantitative geoelectrical model along LP2 (Asfahani, 2007).

The iso-apparent resistivity map established as a function of *AB/2* along *LP2* shown in Fig. 11A is also difficult to be qualitatively interpreted in comparing with that obtained by applying the proposed multi fractal approach (Fig.11B). An acceptable coincidence between the multi fractal established apparent resistivity cross-section along *LP2* profile (Fig.11B) and the traditional 1D quantitative interpretation along this *LP2* profile is also obtained, as shown in Fig. 11C (Asfahani, 2007).

The application of fractal approach (*C-N*) on the 192 apparent resistivity data points related to *LP3* profile indicates four threshold break points of C1, C2, C3 and C4 at 0.75, 0.98, 1.24 and 1.43 respectively as shown in Fig.12. The log (ϱa) values indicate an apparent resistivity of 5.6, 9.5, 17.4 and 30 Ω.m respectively. Those four break points correspond to five apparent resistivity ranges as follows; the first range is less than 5.6 Ω.m, the second range is between 5.6 and 9.5 Ω.m, the third range is between 9.5 and 17.4 Ω.m, the fourth range is between 17.4 and 30 Ω.m. The fifth range is bigger than 30 Ω.m. The established apparent resistivity cross-section along *LP3* profile is shown in Fig. 13B. The same remarks as documented on *LP1* and *LP2* profiles could be shown with *LP3* profile. The iso-apparent resistivity map established as a function of *AB/2* along *LP3* shown in Fig. 13A is also difficult to be qualitatively interpreted when compared with that obtained by applying multi fractal approach.

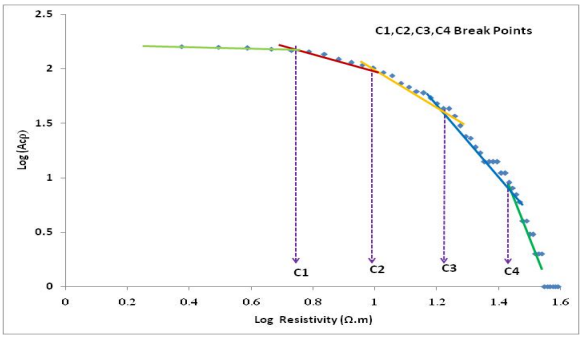

Figure 12. Fractal C-N log-log plot for the measured apparent resistivity data along LP3 profile.

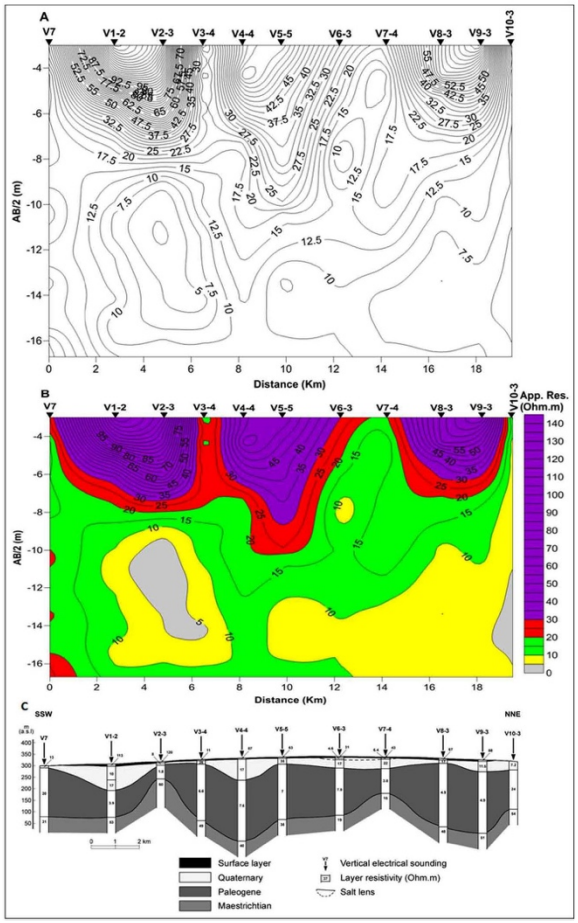

Figure 13 A. Traditional iso-apparent resistivity cross-section along the LP3 profile. B: Concentration-number fractal model along with LP3 profile. C: Traditional quantitative geoelectrical model along LP3 (Asfahani, 2007).

The application of fractal (*C-N*) approach on the 144 apparent resistivity data points related to the transverse *TP5* profile shows four threshold break points C1, C2, C3 and C4 at 1, 1.19, 1.44 and 1.70 respectively as presented in Fig.14. The log (*ρa*) values indicate an apparent resistivity of 10, 15, 27.5 and 50 Ω.m respectively. Those four break points correspond to five apparent resistivity ranges as follows: the first range is less than 10 Ω.m,

the second range is between 10 and 15 Ω.m, the third range is between 15 and 27.5 Ω.m, the fourth range is between 27.5 and 50 Ω.m. The fifth range is bigger than 50 Ω.m. The established apparent resistivity cross-section along *TP5* profile is illustrated in Fig.15A.

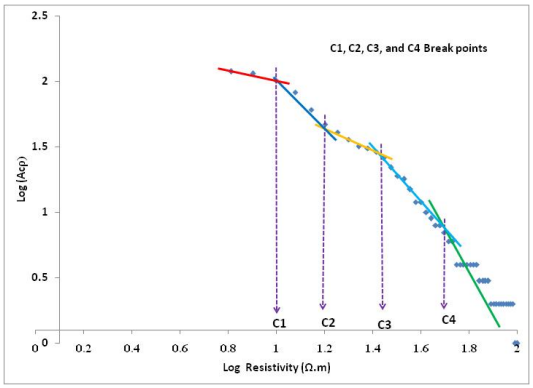

Figure 14. Fractal C-N log-log plot for the measured apparent resistivity data along the TP5 profile.

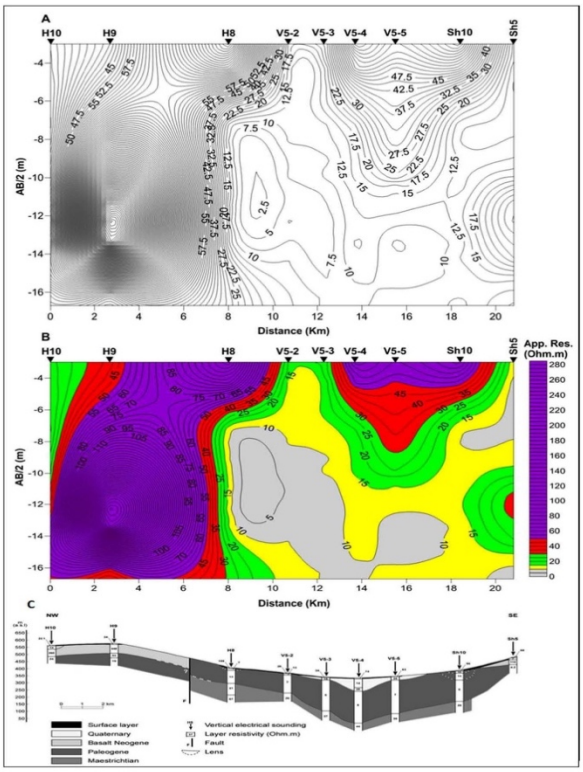

Figure 15 A. Traditional iso-apparent resistivity cross section along TP5 profile. B: Concentration-number fractal model along TP5 profile. C: Traditional quantitative geoelectrical model along TP5 (Asfahani, 2007).

The above-treated examples and the different comparisons shown between the established multifractal cross-sections and the traditional 1D quantitative interpretative models along the studied profiles *LP1, LP2, LP3*, and *TP5* confirm the feasibility of the new proposed fractal approach.

VALIDATION OF THE C-N TECHNIQUE

The fractal *C-N* modeling approach is a nonlinear tool that deals with field apparent resistivity measurements to separate different apparent resistivity ranges, that differ from one profile to another. This approach is newly introduced in this research to interpret in terms of 2D modeling the VES measurements distributed along a given profile.

Traditionally, the field apparent resistivity measurements of each VES point have been treated and interpreted separately using different known inversion procedures. The inversion allows consequently to obtain a one-dimensional (1D) interpretation model including the real thicknesses and resistivities of the layers under the study VES point. On the other hand, when the fractal *C-N* modeling procedure is applied, all the apparent resistivity measurements distributed under a given profile for all *AB/2* spacings are treated together at the same time by the use of log-log plots, as demonstrated above during interpreting the four profiles (*LP1, LP2, LP3*, and *TP5*). The use of the fractal *C-N* model with the log-log plots permits to determine the break points and the different line segments with their related apparent resistivity ranges, by such, it is very sensitive to the lithological boundaries. This efficacy in determining the different break points and the different apparent resistivity ranges gives this fractal method its suitability in comparing with other geostatistical methods.

The two approaches of VES inversion and *C-N* are therefore completely different from a methodological point of view. However, the fractal *C-N* helps widely in separating different apparent resistivity populations, that dominate in the study area, and in relating the apparent resistivity ranges of those populations with geological variations laterally and vertically. Those apparent resistivity ranges help also in calibrating and interpreting correctly the VES data measurements. Such apparent resistivity ranges are also of great importance, particularly when we deal with a sedimentary environment with rapid lateral and vertical changes. The fractal *C-N* modeling is consequently a useful guiding technique that helps us in calibrating and correctly interpreting the VES data.

CONCLUSION

A new semi-quantitative approach is proposed and introduced to interpret vertical electrical sounding (VES) measurements distributed along a given profile. This approach is based on using the fractal modeling technique, with adapting the concentration-number (*C-N*) model. The application of log-log plots with the threshold break points concept allows different apparent resistivity populations to be easily isolated along the studied profiles. Two-dimensional (2D) quantitative interpretation and a preliminary geological analysis could be achieved by using such an approach.

The advantage of this new proposed fractal technique in comparing with other already proposed 2D techniques, is that it does not need prior constraints. The method itself is very sensitive to the lithological variations, where the different lithological boundaries are determined under a given profile. It is therefore easily applicable, where it guides and orients the interpreter to select thereafter the appropriate geoelectrical model to correctly interpret quantitatively the VES data at every measured point. This new technique is practiced and tested on a case study taken from Khanasser Valley region, Northern Syria, where different profiles (*LP1, LP2, LP3, and TP5*) are selected and re-interpreted. The capacity and practicability of the new proposed approach are confirmed through the different comparisons between the multi-fractal established cross-

sections and the traditional (1D) VES interpretation models. The results presented in this paper encourage to use routinely this fractal approach for interpreting VES measurements distributed along a given profile.

ACKNOWLEDGEMENT

The author would like to thank Dr. I. Othman, General Director of Syrian Atomic Energy Commission, for his permission to publish this paper. The three competent anonymous reviewers are deeply thanked for their critics, remarks and suggestions that considerably improve the final version of this paper. Prof. Servando De la Cruz-Reyna, the Editor-in-Chief of Geofísica Internacional is cordialy thanked for the editing and linguistic English corrections.

REFERENCES

ACSAD., 1987, Water resources map of the Arab countries. The Arab Center for the Studies of Arid Zones and Dry Lands, Damascus, Syria.

Afzal P., Fadakar Alghalandis Y., Khakzad A., Moarefvand P., Rashidnejad Omran N., 2011, Delineation of mineralization zones in porphyry Cu deposits by fractal concentration–volume modeling. J Geochem Explor 108:220–232.

Al-Fares W., Asfahani J., 2018, Evaluation of the leakage origin in Abu Baara earthen dam using electrical resistivity tomography, northwestern Syria. Geofísica Internacional, 57-4: 223-237.

Asfahani J., 2007, Geoelectrical investigation for characterizing the hydrogeological conditions in semi-arid region in Khanasser valley, Syria. J. Arid Environ. 68, 31-52.

Asfahani J., Radwan Y., 2007, Tectonic Evolution and Hydrogeological Characteristics of Khanasser Valley, Northern Syria, Derived from the Interpretation of Vertical Electrical Soundings, *Pure appl. Geophy,* 164, 2291–2311, DOI 10.1007/s00024-007-0274-8.

Asfahani J., 2010, Geophysical case study of shallow and deep structures based on traditional and modified interpretation methods: Application to tectonic studies and mineral exploration. *Exploration and Mining Geology, 19*(3–4), 135–152.

Asfahani J., 2011, The Role of Geoelectrical DC Methods in Determining the Subsurface Tectonics Features. Case Studies from Syria, Tectonics, Damien Closson (Ed.), ISBN: 978-953-307-545-7, InTech, Available from: http://www.intechopen.com/articles/show/title/the-role-of-geoelectrical-dc-methods-in-determining-the-subsurface-tectonics-features-case-studies.

Asfahani J., Abou Zakhem B., 2013, Geoelectrical and hydrochemical investigations for characterizing the salt water intrusion in the Khanasser valley, northern Syria. Acta Geophys. 61 (2), 422e444. http://dx.doi.org/10.2478/s11600-012-0071-3.

Asfahani J., 2018, Geoelectrical Combined Sounding-Profiling Configuration for Characterizing the Sedimentary Phosphatic Environment in Al-Sharquieh Deposits Mine in Syria.Geofísica Internacional 57-3: 189-203.

Asfahani J., Al-Fares W., 2021, Geological and structural characterizations of a basaltic environment by vertical electrical soundings and multifractal modeling techniques in Deir El-Adas Area, Yarmouk Basin, Syria. Acta Geodaetica et Geophysica. 56:211–228. https://doi.org/10.1007/s40328-020-00319-z.

Dobrin M B., 1967, Introduction to geophysical prospecting, Mc Graw-Hill, New York.

Edwards L S., 1977, A modified pseudo section for resistivity and IP: Geophysics, Vol. 42, No. 5, P.1020-1036.

Gardi S., Asfahani J., 2019, Subsurface Tectonic Characterizations by the Use of Geo-electrical Resistivity Technique and Their Implications on Environmental Soil and Groundwater at Erbil Dumpsite, West of Erbil City-Iraqi Kurdistan Region. Contributions to Geophysics and Geodesy Vol. 49/3, P:325–354.

Gyulai A., Ormos T., 1999, A new procedure for the interpretation of VES data: 1.5 D simultaneous inversion method. J Appl Geophys 41:1–17.

Gyulai A., Ormos T., Dobro´ka M., 2010, A quick 2D geoelectric inversion method using series expansion. J Appl Geophys 72(4):232–241.

Gyulai A., Baracza MK., Szabo NP., 2014, On the application of combined geoelectric weighted inversion in environmental exploration. Environ Earth Sci 71:383–392.

Gyulai A., Sz}ucs P., Turai E., Baracza M K., Fejes Z., 2016, Geoelectric Characterization of Thermal Water Aquifers Using 2.5D Inversion of VES Measurements. Surv Geophys. DOI 10.1007/s10712-016-9393-z.

Hassanpour S., Afzal P., 2013, Application of concentration-number (CN) multifractal modelling for geochemical anomaly separation in Haftcheshmeh porphyry system, NW Iran. Arab J Geosci 6:957–970. doi:10.1007/s12517-011-0396-2.

Hoogeveen RJA., Zobisch M., 1999, Decline of groundwater quality in Khanasser valley (Syria) due to salt-water intrusion. Paper presented at International Dryland Conference, Cairo, Egypt, 16p.

Lengiprovodkhoz Institute., 1987, Water resources in the Syrian desert, Syrian Arab Republic for pasture water supply. *In*: *Hydrogeology*. Moscow: USSR Ministry of Land Reclamation and Water Management, Volume 1, Book 2.

Li C., Ma T., Shi J., 2003, Application of a fractal method relating concentrations and distances for separation of geochemical anomalies from background. J Geochem Explor 77:167–175.

Mandelbrot B B., 1983, The Fractal Geometry of Nature, W. H. Freeman, San Fransisco, 468 pp.

Mohammadi A., Khakzad A., Rashidnejad Omran N., Mahvi MR., Moarefvand P., Afzal P., 2013, Application of number–size (N–S) fractal model for separation of mineralized zones in Dareh-Ashki gold deposit, Muteh Complex, Central Iran. Arab J Geosci. doi:10.1007/s12517-012-0662-y.

Olasehinde PI., Ejepu SJ., Alabi AA., 2013, Fracture Detection in a Hard Rock Terrain Using Geoelectric Sounding Techniques. Water Resources Journal 23(1&2): 1-19.

Orellana E., Mooney HM., 1966, Master Tables and curves for vertical electrical sounding over layered structures, interciencia, Madrid, Spain.

Pichgin NI., Habibullaev IKH., 1985, Methodological Recomendations in studying geo- tectonic conditions of vertical electrical soundings data with application of EC computer for solving hydrogeological and geo-engineering problems, Tashkend (in Russian).

Ponikarov., 1964, The Geological Map of Syria, 1:200.000 and Explanatory. Notes. Syrian Arab Republic, Ministry of Industry, Department of Geological and Mineral Research, Damascus,Syria.

Reynolds JM., 2011, An Introduction to Applied and Environmental Geophysics. Wiley – Blackwell, 698p.

Schweers W., Rieser A., Bruggeman A., Abu-Zakhem B., Asfahani J., Kadkoy N., Kasmo B., 2002, Assessment of groundwater resources for sustainable management in the Khanasser valley, northwest Syria. Paper presented at ACSAD/BGR Workshop on Soil and Groundwater Quality: Monitoring Management and Protection, Amman, 23-25 June 2002.

Wang Q F., Deng J., Liu H., Wang Y., Sun X., Wan L., 2011, Fractal models for estimating local reserves with different mineralization qualities and spatial variations. J. Geochem. Explor. 108, 196–208. doi:10.1016/j.gexplo.2011.02.008.

Zohdy A A R., Eaton GP., Mabey DR., 1984, Applications of Surface Geophysics to Groundwater Investigations: Department of Interior US Geological Survey, Third Printing. US Government Printing Office, Washington, p.116.
Zohdy A A R., 1989, A new method for the automatic interpretation of Schlumberger and Wenner sounding curves, Geophysics, vol. 54, 245-253.

Zohdy A A R., Bisdorf R J., 1989, Schlumberger sounding data processing and interpretation program, U. S. Geological Survey, Denver.

Zuo R., 2011, Decomposing of mixed pattern of arsenic using fractal model in Gangdese belt, Tibet, China. Appl Geochem 26:S271–S273.

Zuo, R.: Decomposing of mixed pattern of arsenic using fractal model in Gangdese belt, Tibet, China. Appl

Geochem 26: S271–S273 Davis JC (2002) Statistics and data analysis in geology, 3rd ed. John Wiley & Sons Inc, New York,2011.

Original paper

https://doi.org/10.22201/igeof.00167169p.2021.60.3.2024

How to use solutions of advection-dispersion equation to describe reactive solute transport through porous media

Jetzabeth Ramírez-Sabag[1] and Dennys A. López-Falcón[1*].

Received: December 11, 2019; accepted: April 4, 2021; published online: July 1, 2021.

Resumen

Las soluciones de la ecuación de advección-dispersión son usadas frecuentemente para describir el transporte de solutos a través de medios porosos, considerando adsorción en equilibrio, de tipo lineal y reversible. Para indicar algunas sugerencias acerca de este tema, se hizo una revisión de las soluciones analíticas disponibles. Hay soluciones para problemas con condiciones de frontera, de primer y tercer-tipo en la entrada, así como de primer y segundo-tipo a la salida. Se analiza el comportamiento de las soluciones equivalentes, para sistemas finitos y semi-infinitos, observando que las soluciones de los sistemas semi-infinitos se aproximan a las correspondientes de los sistemas finitos conforme la condición de frontera de salida en el infinito se aproxima a la ubicación de medición del sistema finito. Solamente se presentan las soluciones analíticas con condiciones de frontera de segundo-tipo a la salida, ya que son iguales a las correspondientes soluciones analíticas con frontera de primer-tipo a la salida, para ambos tipos de condiciones de frontera de entrada usadas. Un análisis paramétrico, basado en el número de Peclet, muestra que todas las soluciones convergen cuando el número de Peclet es mayor que veinte. Los sistemas investigados deben tener un número de Peclet mayor que cinco para usar con confianza las soluciones de la ecuación de advección-dispersión para describir el transporte de soluto en medios porosos.

Palabras clave: Ecuación de advección-difusión, soluciones analíticas, transporte de solutos reactivos, medios porosos.

Abstract

The solutions of advection-dispersion equation are frequently used to describe solute transport through porous media when considering lineal and reversible equilibrium adsorption. To notice some warnings about this item, a review of analytical solutions available was done. There are solutions for boundary value problems with first and third-type inlet boundary conditions as well as first and second-type outlet boundary condition. The behavior of equivalent solutions for finite and semi-infinite systems are analyzed, observing that semi-infinite system solutions approximates to the corresponding finite ones as the "infinite" outlet boundary condition approach to the finite measurement location. Because the analytical solutions with a first-type outlet boundary condition are equal to the corresponding analytical solutions with a second-type

Corresponding author: dalopez@imp.mx

Instituto Mexicano del Petróleo, Gerencia de Ingeniería de Yacimientos, CDMX. CP 07730. México

[1]*Instituto Mexicano del Petróleo. CDMX. CP 07730. México*

one, for both inlet boundary condition type used, only the latter is presented. A parametric analysis based on Peclet number shows that all solutions converge for Peclet number greater than twenty. Systems under research must have Peclet number greater than five to use confidently the solutions of advection-dispersion equation to describe reactive solute transport through porous media.

KEYWORDS: Advection-diffusion equation, analytical solutions, reactive solute transport, porous media.

INTRODUCTION

From the perspective in continuous media mechanics, the advection-dispersion equation (ADE) is the fundamental element to develop a mathematical model that describes the reactive solute transport throughout porous media (Allen *et al.*, 1988; Cao *et al.*, 2020; Fried, 1975; Parker and van Genuchten, 1984; Sorbie *et al.*, 1987; van Genuchten and Parker, 1984). ADE results from total solute mass balance equation, which is obtained by adding the solute mass balance equation on both phases, fluid and solid, and assuming that reaction of solute between both phases is instantaneous, such that local equilibrium is valid, and then it is possible to simplify the expression corresponding to the retardation factor. The implicit physical phenomena are the advection due to drag from the fluid velocity field, which transports the solution, and the hydrodynamic dispersion that accounts for both the mechanical dispersion and the molecular diffusion (Bear, 1988; Bear and Bachmat, 1990). Boundary value problems (BVPs) can be obtained from the ADE, by addition of constraints named boundary conditions specified either on the solute concentration value itself (first-type), on its derivative (second-type) or even on both (third-type); also the boundary conditions are labeled inlet at the injection point and outlet at the withdrawal point, respectively. To describe the complex interrelated phenomena, existing in the reactive solute transport through porous media, non-linear equations are often needed, then an analytical solution is very difficult or even impossible to obtain. However, by establishing some simplifications, it is possible to get analytical solutions, as portrayed in this work.

Studies of solute transport are frequently done by analyzing the solute concentration on effluent samples collected at an observation point. The breakthrough curve is a plot of the effluent concentration versus time (often both dimensionless). Matching the breakthrough curve to a mathematical model available it is possible to obtain the corresponding fitting parameters, such as longitudinal dispersion and retardation factor.

An important part of mathematical models is the appropriate selection of boundary and initial conditions. This topic has been subject of many papers since the initial works in geohydrology, particularly in the case of uniform flow in homogeneous porous media (Gershon and Nir, 1969; Kreft and Zuber, 1978; van Genutchen and Alves, 1982; van Genuchten and Parker, 1984; Parker and van Genuchten, 1986).

Previous studies that evaluated the suitability of prescribed boundary conditions to predict measured solute concentrations in controlled column experiments have addressed the case of saturated flow in artificial and nonreactive media (James and Rubin, 1972; Parker, 1984; Novakowski, 1992b). Outlet effects can be accounted for in the numerical solution to estimate the amount of dispersion that occurs only in the media (James and Rubin, 1972). It has been shown that when local equilibrium between pore regions is not attained, the analytical solution with finite boundaries fails to describe measured concentrations (Parker, 1984). However, for

slow pore water velocities, the ADE should provide a good description to experimental data (Schwartz *et al.*, 1999).

The concepts of volume-averaged and flux-averaged concentration were introduced aiming to reproduce real conditions in solute sampling methods (Brigham, 1974; Kreft and Zuber, 1978). Depending on the sampling method it can be necessary to distinguish between volume-averaged and flux-averaged concentrations, which are defined by the mass of solute per elementary volume of the porous media at a given time, and as the mass of solute crossing a unit area per element of time; respectively. In both cases the concentration is defined macroscopically (Novakowsky, 1992a).

BVPs with first-type inlet boundary condition, concentration value prescribed, has been solved for both semi-infinite and finite systems (Danckwerts, 1953; Ogata and Banks, 1961, Lapidus and Amundson, 1952; Cleary and Adrian, 1973). BVPs with third-type inlet boundary condition, flow value prescribed, has been solved for also both semi-infinite and finite systems (Brenner, 1962; Coats and Smith, 1964; Lindstrom *et al.*, 1967). Regarding to outlet boundary condition there are BVPs with first-type, zero concentration value prescribed, only for semi-infinite system (Ogata and Banks, 1961; Coats and Smith, 1964). BVPs with second-type outlet boundary condition, zero gradient concentration prescribed, has been solved for semi-infinite system (Lapidus and Amundson, 1952; Lindstrom *et al.*, 1967). However, the corresponding solution to BVP with second-type outlet boundary condition is the same as the solution to BVP with first-type outlet boundary condition, provided that inlet boundary condition is the same type. That is, BVP-1,1 has the same solution as BVP-1,2; as well as BVP-3,1 has the same solution as BVP-3,2 (see Table 1 for notation). For finite system, the only outlet boundary condition used is second-type (Brenner, 1962; Cleary and Adrian, 1973).

Defining appropriate boundary conditions between porous and non-porous media is not a simple subject (Parker and van Genutchen, 1986). Several efforts have been performed to determine the real type of boundary conditions that apply in solute transport experiments through porous columns (van Genutchen and Parker, 1984; Novakowski, 1992a,b; Schwartz *et al.*, 1999). Results indicate that to certain extent third-type inlet boundary condition can better describe laboratory data than first-type inlet boundary condition can. Some apparently innocuous first-type boundary condition result in solutions that are mathematically correct but physically incorrect, since they yield improper mass balance and pulse behavior (Coronado *et al.*, 2004). This might be the reason why models based on some first-type inlet boundary conditions have failed in matching experimental data.

This paper remarks some warnings about using solutions of ADE to describe reactive solute transport through porous media. In the next section, the ADE is introduced and a discussion about various solutions available in both semi-infinite and finite systems is given. The next section shows some results based on breakthrough curves for every analytical solution available. A parametric analysis with the Peclet number is done to observe the range of values where a good approximation between solutions is obtained. Conclusions and suggestions are provided in the final section.

THEORY

The governing equation to describe reactive solute transport with linear and reversible equilibrium adsorption through homogeneous porous media, during saturated flow, is the called

ADE:

$$R\frac{\partial c}{\partial t} = D\frac{\partial^2 c}{\partial x^2} - v\frac{\partial c}{\partial x} \tag{1}$$

where c is the solute concentration on fluid phase, D is the longitudinal dispersion coefficient, v is the average pore velocity, R is the retardation factor describing solute sorption, t is time and x is longitudinal distance. It must be noted that, $R = 1 + \frac{\rho}{\phi}\frac{\partial \sigma}{\partial c}$, where it is assumed that the solute concentration on solid phase, σ, depends only on the solute concentration on fluid phase; ρ is the bulk density, and ϕ is the porosity of porous media.

Solutions

In order to obtain analytical solutions of ADE (1), some simplifying assumptions are needed to decrease the complexity of the problem. Neglecting molecular diffusion, the solute transport is basically hydrodynamic. The injection of solute into the inlet boundary is such that solute velocities are proportional to velocities of the particular flow paths causing concentration to be weighted by the combined flow rates of all flow paths. On these conditions it is agreed that the correct inlet boundary condition for flux injections of solution with a prescribed concentration c_0 is (Danckwerts, 1953; van Genuchten and Parker, 1984; Parker and van Genuchten, 1984; Barry and Sposito, 1988; Novakowski, 1992a,b; Schwartz *et al.*, 1999):

$$\lim_{x\to 0^+}\left[vc - D\frac{\partial c}{\partial x}\right] = vc_0 \tag{2}$$

which is a third-type specified flux boundary condition that is required by mass conservation across the inlet boundary condition.

However a first-type specified concentration boundary condition has also been used frequently:

$$c(0,t) = c_0 \tag{3}$$

This condition implies a usually not possible in practice situation, the concentration itself needs to be specified at the porous media surface. Moreover the solutions obtained with this condition not satisfied mass conservation.

For a semi-infinite system, the outlet boundary condition specify the behavior of the concentration as infinity is closer. It is plausible that change in concentration with respect to distance are negligible as distance goes to infinity, thus the outlet boundary condition is (van Genutchen and Parker, 1984; Schwartz *et al.*, 1999):

$$\lim_{x\to\infty}\frac{\partial c(x,t)}{\partial x} = 0 \tag{4}$$

Furthermore first-type specified zero concentration outlet boundary condition can be as (Ogata and Banks, 1961):

$$c(\infty,t) = 0 \tag{5}$$

To use a first-type specified zero concentration outlet boundary condition might be easier than a second-type zero gradient outlet boundary condition, both analytically and numerically.

For a finite system, one requirement that always must be satisfied is continuity of the solute velocity across the outlet boundary condition (van Genutchen and Parker, 1984):

$$\lim_{x\to L^-}\left[vc - D\frac{\partial c}{\partial x}\right] = vc_e \tag{6}$$

where L^- indicates evaluation just inside the limit of the porous media been observed, and $c_e = c_e(t)$ is the concentration evaluated in the outlet, that is, the effluent concentration. As the inlet boundary condition (2) this outlet boundary condition (6) assumes that diffusion-dispersion phenomena outside the system are negligible.

Assuming that the solute concentration should be continuous across the outlet boundary:

$$c\left(L^-,t\right) = c_e\left(t\right) \tag{7}$$

Therefore, the outlet boundary condition (6) results in:

$$\frac{\partial c\left(L,t\right)}{\partial x} = 0 \tag{8}$$

which is a second-type zero-gradient outlet boundary condition, almost always used (Brenner, 1962; Cleary and Adrian; 1973).

To complete the different BVPs to be analyzed here, the initial condition that describe a porous media system free of solute is used:

$$c\left(x,0\right) = 0 \tag{9}$$

Table 1 summarizes the various BVPs, which could be defined with the above boundary and initial conditions.

For a semi-infinite system, the first BVP listed on Table 1, called BVP-1,1, have the inlet boundary condition (3), the outlet boundary condition (5) and the initial condition (9); which analytical solution for ADE (1) is adapted from Ogata and Banks (1961):

$$\frac{c\left(x,t\right)}{c_0} = \frac{1}{2}\operatorname{erfc}\left(\frac{Rx-vt}{2\sqrt{DRt}}\right) + \frac{1}{2}\exp\left(\frac{vx}{D}\right)\operatorname{erfc}\left(\frac{Rx+vt}{2\sqrt{DRt}}\right) \tag{10}$$

The second BVP on Table 1, called BVP-1,2, has the same inlet boundary condition (3) and initial condition (9) as the first one, but the outlet boundary condition is now (4). Its analytical solution, adapted from Lapidus and Amundson (1952), is the same as the solution for ADE (1) , adapted from Ogata and Banks (1961). For this reason, only one will be presented.

The BVP-3,1 is defined using the inlet boundary condition (2), the outlet boundary condition (5) and the initial condition (9). Its analytical solution is taken from Coats and Smith (1964):

$$\begin{aligned}\frac{c\left(x,t\right)}{c_0} &= \frac{1}{2}\operatorname{erfc}\left(\frac{Rx-vt}{2\sqrt{DRt}}\right) + \sqrt{\frac{v^2t}{\pi DR}}\exp\left(-\frac{\left(Rx-vt\right)^2}{4DRt}\right) \\ &-\frac{1}{2}\left(1+\frac{vx}{D}+\frac{v^2t}{DR}\right)\exp\left(\frac{vx}{D}\right)\operatorname{erfc}\left(\frac{Rx+vt}{2\sqrt{DRt}}\right)\end{aligned} \tag{11}$$

The BVP-3,2 is like the previous one, but using the outlet boundary condition (4). The analytical solution is given by Lindstrom *et al.* (1967) and is the same as the analytical solution adapted from Coats and Smith (1964). For this reason, only one will be presented.

Expressions for the effluent concentration $c_e(t)$ are obtained by evaluation of each solution in $x = L$.

Table 1. Summary of BVPs analyzed.

Notation	Type of System	Type of Inlet Boundary Condition	Type of Outlet Boundary Condition	Reference to the Analytical Solution
BVP-1,1	Semi-Infinite	First-type Equation (3)	First-type Equation (5)	Ogata and Banks, 1961.
BVP-1,2	Semi-Infinite	First-type Equation (3)	Second-type Equation (4)	Lapidus and Amundson, 1952.
BVP-3,1	Semi-Infinite	Third-type Equation (2)	First-type Equation (5)	Coats and Smith, 1964.
BVP-3,2	Semi-Infinite	Third-type Equation (2)	Second-type Equation (4)	Lindstrom *et al.*, 1967.
FBVP-1,2	Finite	First-type Equation (3)	Second-type Equation (8)	Cleary and Adrian, 1973.
FBVP-3,2	Finite	Third-type Equation (2)	Second-type Equation (8)	Brenner, 1962.

For a finite system, similar problems can be defined. Thus the problem with the inlet boundary condition (2), the outlet boundary condition (8), and the initial condition (9); is the FBVP-3,2 which have the analytical solution adapted from Brenner (1962):

$$\frac{c(x,t)}{c_0} = 1 - \sum_{k=1}^{\infty} \frac{\frac{vL\lambda_k}{2D}\left[\lambda_k \cos\left(\frac{2\lambda_k x}{L}\right) + \frac{vL}{4D}\sin\left(\frac{2\lambda_k x}{L}\right)\right]}{\left[\lambda_k^2 + \left(\frac{vL}{4D}\right)^2 + \frac{vL}{4D}\right]\left[\lambda_k^2 + \left(\frac{vL}{4D}\right)^2\right]} \exp\left(\frac{vx}{2D} - \frac{v^2 t}{4DR} - \frac{4\lambda_k^2 Dt}{L^2 R}\right) \quad (12)$$

where λ_k are the positive roots of:

$$\tan(2\lambda_k) = \frac{\frac{\lambda_k vL}{2D}}{\lambda_k^2 - \left(\frac{vL}{4D}\right)^2} \quad (13)$$

The FBVP-1,2 is like the previous one, but using the inlet boundary condition (3); and have the analytical solution adapted from Cleary and Adrian (1973):

$$\frac{c(x,t)}{c_0} = 1 - \sum_{m=1}^{\infty} \frac{2\alpha_m \sin\left(\frac{\alpha_m x}{L}\right)\exp\left(\frac{vx}{2D} - \frac{v^2 t}{4DR} - \frac{\alpha_m^2 Dt}{L^2 R}\right)}{\left[\alpha_m^2 + \left(\frac{vL}{2D}\right)^2 + \frac{vL}{2D}\right]} \quad (14)$$

where α_m are the positive roots of:

$$\alpha_m \cot(\alpha_m) = -\frac{vL}{2D} \tag{15}$$

Expressions for the effluent concentration $c_e(t)$ are obtained by evaluation of each solution in $x = L$.

In order to compare the solutions for the semi-infinite system with the solutions for the finite system, the position of the outlet boundary condition is denoted by x_{OBC} and the observation or measuring position by L.

RESULTS AND DISCUSSION

Dimensionless variables are used to solute concentration, $c_D = c/c_0$, and time, $t_D = tv/L$; as well as some useful parameters like the Peclet number, $Pe = vL/D$, and dispersivity, $\alpha = D/v$.

Figure 1 shows the breakthrough curves corresponding to the analytical solutions for the different initial and boundary value problems described above. The Peclet number was chosen equal to 1 to increase the differences among the solutions because, as can be seen in Figure 2, for a Peclet number equal to 20, some breakthrough curves become practically indistinguishable. It can be observed that analytical solutions approach each other as Peclet number grows, such that differences between them are practically negligible for a Peclet number greater than twenty. Note that only four curves are shown because two solutions are identical to another two, specifically BVP-1,1 has the same solution as BVP-1,2; as well as BVP-3,1 has the same solution as BVP-3,2.

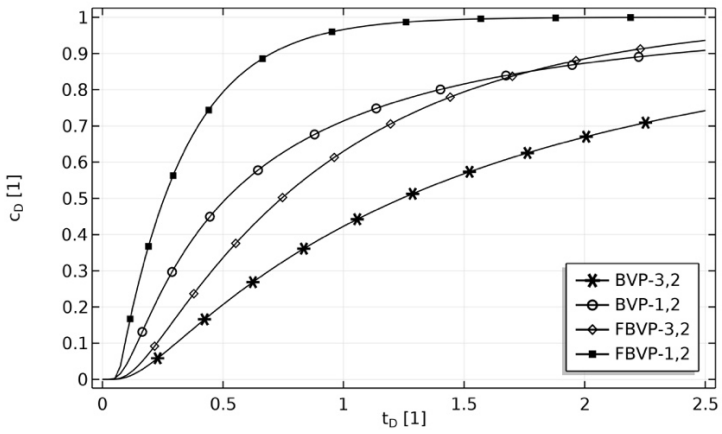

Figure 1. Breakthrough curves for semi-infinite systems (BVP) and finite systems (FBVP). The Peclet number equals 1.

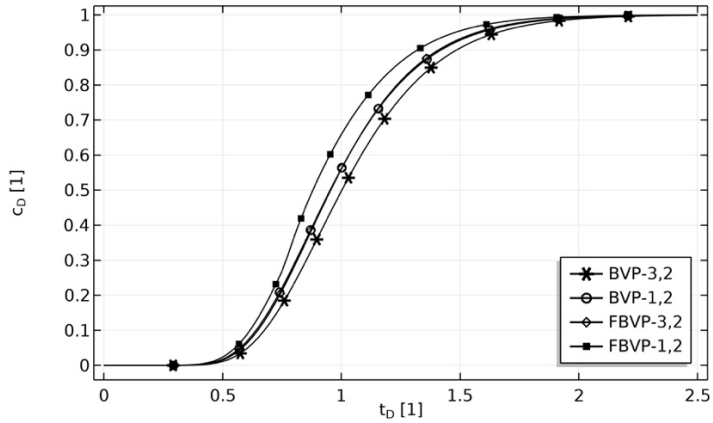

Figure 2. Breakthrough curves for semi-infinite systems (BVP) and finite systems (FBVP). The Peclet number equals 20.

The Peclet number is used to do a parametric analysis for each problem in Table 1. Figure 3 shows the breakthrough curves for the FBVP-3,2 depending on the Peclet number. For a finite system, the position of the outlet boundary condition is the same as the measurement position, $x_{OBC} = L$.

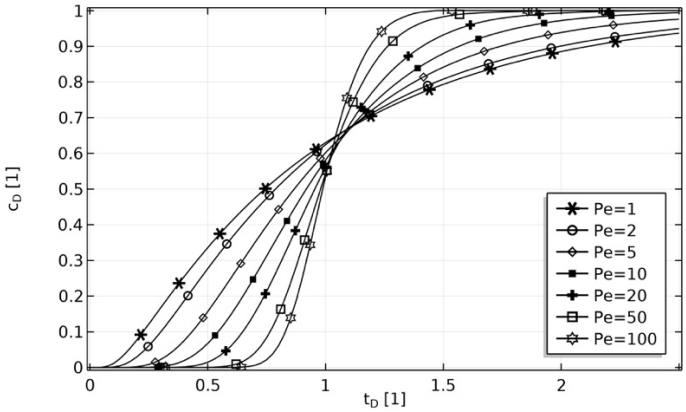

Figure 3. Breakthrough curves for the FBVP-3,2 depending on the Peclet number.

Figure 4 shows the breakthrough curves for the BVP-3,2 depending on the Peclet number. In this case, the position of the outlet boundary condition goes to infinity.

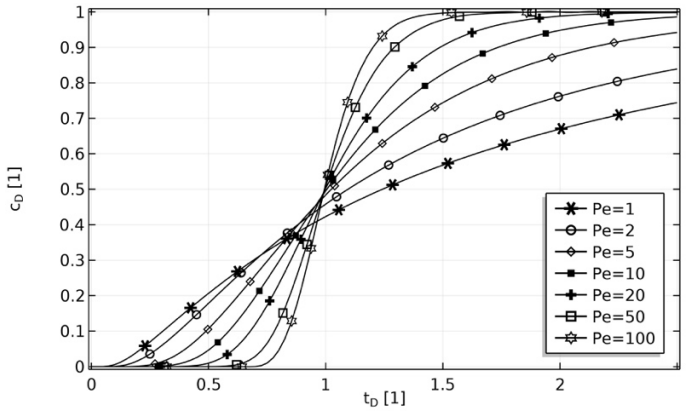

Figure 4. Breakthrough curves for the BVP-3,2 depending on the Peclet number.

In Figure 5, observe how, as the position of the outlet boundary condition goes from the measurement position to infinity, the breakthrough curves go from the analytical solution for the finite system to the analytical solution for the semi-infinite system.

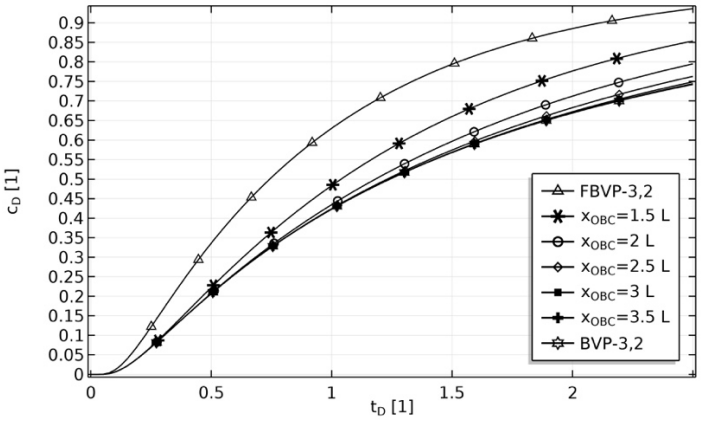

Figure 5. Breakthrough curves for the FBVP-3,2 and the BVP-3,2; and transition between them as the position of the outlet boundary condition goes from the measurement position to infinity. The Peclet number equals 1.

Figure 6 shows the breakthrough curves for the FBVP-1,2 depending on the Peclet number. For a finite system, the position of the outlet boundary condition is the same as the measurement position, $x_{OBC} = L$.

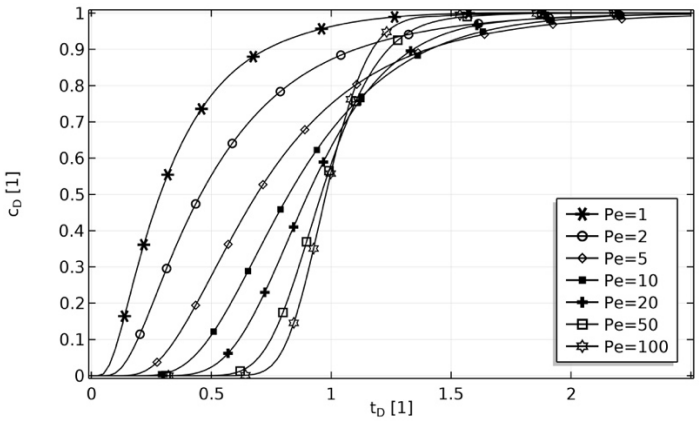

Figure 6. Breakthrough curves for the FBVP-1,2 as function of the Peclet number.

Figure 7 shows the breakthrough curves for the same problem as above, but for a semi-infinite system, it is a BVP-1,2. In this case, the position of the outlet boundary condition goes to infinity,

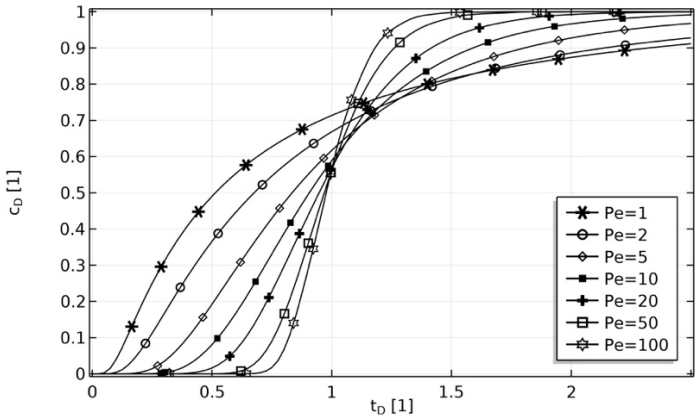

Figure 7. Breakthrough curves for the BVP-1,2 as function of the Peclet number.

In Figure 8, observe how, as the position of the outlet boundary condition goes from the measurement position to infinity, the breakthrough curves go from the analytical solution for the finite system to the analytical solution for the semi-infinite system.

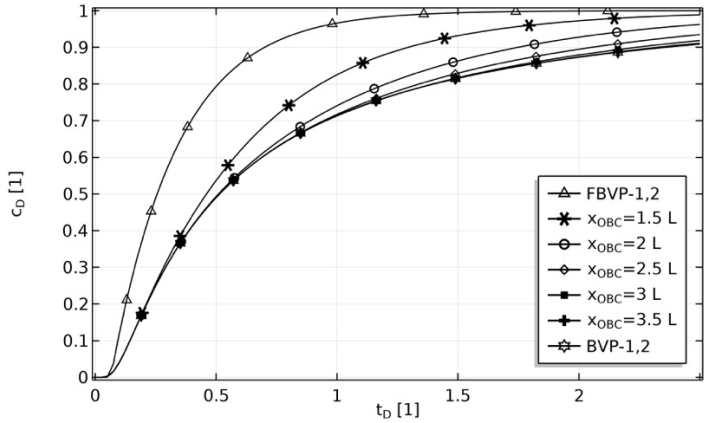

Figure 8. Breakthrough curves for the FBVP-1,2 and for the BVP-1,2; and transition between them as the position of the outlet boundary condition goes from the measurement position to infinity. The Peclet number equals 1.

It is very important to estimate the Peclet number, for each experimental or field test, to have confidence about using analytical solutions of ADE to describe solute transport through porous media. Be aware of which solution may be more appropriate to describe data obtained from a real breakthrough curve because, as is shown here, there may be significant differences between them; and then get misleading parameters from the matching procedure.

Conclusions

Analytical solutions for different BVPs defined by de ADE with various combinations of inlet and outlet boundary conditions, and the initial condition corresponding to a free of solute, both finite and semi-infinite systems, had been analyzed systematically. All the available analytical solutions are plotted together to observe their behavior for a Peclet number equal to one (Fig. 1) and for a Peclet number equal to twenty (Fig. 2). From this comparison, it is concluded that

much thoughtfulness must be taken to choose the most suitable analytical solution to describe the transport of reactive solute through porous media when the system to be studied has a Peclet number smaller than five. However, when the system under research has a Peclet number greater than twenty, the differences between all solutions available are practically negligible and therefore any of them could be useful. It is important to remark that, even though, the analytical solution for the BVP-1,1 is the same as the analytical solution for the BVP-1,2, as well as, the analytical solution for the BVP-3,1 is the same as the analytical solution for the BVP-3,2 it is generally easier to compute, to use, and to implement, the former than the latter. That is because an outlet boundary condition type-1 prescribes the variable value directly instead of prescribing its derivative as an outlet boundary condition type-2 does. Even more, when a numerically solution is to be implemented, some advantage could be obtained if an outlet boundary condition type-1 is used, instead of a type-2.

It is possible to observe the behavior of the solutions going from the solution for the finite system to that for the semi-infinite system, moving the location of the outlet boundary condition from the observation or measurement location, where $x_{OBC} = L$; to infinity, where it is enough that $x_{OBC} > 3L$. Fig. 5 shows the transit from the FBVP-3,2 analytical solution to the BVP-3,2 analytical solution, while Fig. 8 shows the transit from the FBVP-1,2 analytical solution to the BVP-1,2 analytical solution. From these observations it can be concluded that location of the outlet boundary condition must be at least three times away from the observation or measurement location, *i.e.* $x_{OBC} > 3L$, in order to obtain a good approximation (Figs. 3-8).

Based on the parametric analysis done, it is advisable that system studied has a Peclet number at least of five, confirming suggestions by other authors (*e.g.* van Genutchen and Parker, 1984; Parlange *et al.*, 1985; Coronado and Ramirez-Sabag, 2005), in order to confidently use the solutions mentioned above. Also could be observed in Fig. 2 that for Peclet number greater than twenty, there are not significant difference between the revised solutions, therefore there are not preference to use anyone of them.

REFERENCES

Allen, M.B., Herrera, I., Pinder, G.F., 1988. Numerical modeling in science and engineering. John Wiley & Sons., USA.

Barry, D.A., and G. Sposito, 1988. Application of the convection-dispersion model to solute transport in finite soil columns, *Soil Sci. Soc. Am. J.*, 52, 3-9.

Bear, J., 1988. Dynamics of fluids in porous media. Dover, USA.

Bear, J., Bachmat, Y., 1990. Introduction to modeling of transport phenomena in porous media. Springer, USA.

Brenner H., 1962. The diffusion model of longitudinal mixing in beds of finite length. Numerical values, *Chemical Engineering Science*, 17, 229-243.

Brigham, W.E., 1974. Mixing equations in short laboratory cores, *Society of Petroleum Engineers Journal*, 14, 91-99.

Cao, D., Wang, J., Han, M., Alshehri, A.J., 2020. Propagation of surfactant and polymer flow in natural carbonate cores. Petroleum. https://doi.org/10.1016/j.petlm.2020.08.002.

Cleary, R.W., and D.D. Adrian, 1973. Analytical solution of the convective-dispersive equation for cation adsorption in soils, *Soil Sci. Soc. Am. Proc.*, 37, 197-199.

Coats, K.H., and B.D. Smith, 1964. Dead-end pore volume and dispersion in porous media, *Society of Petroleum Engineers Journal*, 73-84, March.

Coronado, M., J. Ramirez, F. Samaniego, 2004. New considerations on analytical solutions employed in tracer flow modeling, *Transport in Porous Media*, 54: 221-237.

Coronado, M., and J. Ramirez-Sabag, 2005. A new analytical formulation for interwell finite-step tracer injection tests in reservoirs, *Transport in Porous Media*, 60: 339-351.

Danckwerts, P.V., 1953. Continuous flow systems, *Chemical Engineering Science*, 2, 1-13.

Fried, J.J., 1975. Groundwater Pollution. Elsevier Science Publishing Co., New York City.

Gershon, N.D., and A. Nir, 1969. Effect of boundary conditions of models on tracer distribution in flow through porous mediums, *Water Resources Research*, 5, 830-839.

James, R.V., and J. Rubin, 1972. Accounting for apparatus-induced dispersion in analysis of miscible displacement experiments, *Water Resources Research*, 8, 717-721.

Kreft, A., and A. Zuber, 1978. On the physical interpretation of the dispersion equation and its solution for different initial and boundary conditions, *Chemical Engineering Science*, 33, 1471-1480.

Lapidus, L., and N.R., Amundson, 1952. Mathematics of adsorption in beds, VI, The effect of longitudinal diffusion in ion exchange and chromatographic columns, *J. Phys. Chem.*, 56, 984-988.

Lindstrom, F.T., R. Haque, V.H. Freed, L. Boersma, 1967. Theory on the movement of some herbicides in soils: Linear diffusion and convection of chemicals in soils. *Environ. Sci. Technol.,* 1, 561-565.

Novakowski, K.S., 1992a. An evaluation of boundary conditions for one-dimensional solute transport, 1, Mathematical development, *Water Resources Research*, 28, 2399-2410.

Novakowski, K.S., 1992b. An evaluation of boundary conditions for one-dimensional solute transport, 2, Column experiments, *Water Resources Research*, 28, 2411-2423.

Ogata, A., and R.B. Banks, 1961. A solution of the differential equation of longitudinal dispersion in porous media, *USGS Professional Paper*, 411-A, Washington.

Parker, J.C., 1984. Analysis of solute transport in column tracer studies, *Soil Sci. Soc. Am. J.*, 48, 719-724.

Parker, J.C., and M.T. van Genuchten, 1984. Flux-averaged and volume-averaged concentrations in continuum approaches to solute transport, *Water Resources Research*, 20, 866-872.

Parker, J.C., and M.T. van Genuchten, 1986. Replay, *Water Resources Research*, 22, 1159-1160.

Parlange, J.Y., D.A. Barry, J.L. Starr, 1985. Comments on Boundary conditions for displacement experiments through short laboratory soil columns, *Soil Sci. Soc. Am. J.*, 49, 1325.

Schwartz, R.C., K.J. McInnes, A.S.R. Juo, L.P. Wilding, 1999. Boundary effects on solute transport in finite soil columns, *Water Resources Research*, 35, 671-681.

Sorbie, K.S., Parker, A., Clifford, P.J., 1987. Experimental and theoretical study of polymer flow in porous media. SPERE (Aug. 1987) 281-304.

van Genuchten, M.T., and W.J. Alves, 1982. Analytical solutions of the one-dimensional convective-dispersive solute transport equation, *USDA Technical Bulletin*, 1661.

van Genuchten, M.T., and J.C. Parker, 1984. Boundary conditions for displacement experiments through short laboratory soil columns, *Soil Sci. Soc. Am. J.*, 48, 703-708.

Original article

https://doi.org/10.22201/igeof.00167169p.2021.60.3.2041

Application of Quantitative Electromagnetic Technology to Assess Coating Integrity of Pipelines in Mexico

Omar Delgado-Rodríguez[1*], Aleksandr Mousatov[2], Edgar Kiyoshi Nakamura-Labastida[2] and Vladimir Shevnin[3]

Received: February 25, 2020; accepted: April 15, 2021; published on-line: July 1, 2021.

Resumen

Existen varios métodos de inspección superficial para evaluar la integridad del revestimiento de los ductos metálicos, obteniendo resultados cualitativos aceptables en algunos tipos de suelo y en sistemas de tuberías de baja complejidad. Sin embargo, estos métodos no determinan los parámetros necesarios para una evaluación cuantitativa de la calidad del revestimiento. El Instituto Mexicano del Petróleo desarrolló la Tecnología de Inspección Electromagnética Superficial (SEMPI) para la evaluación cuantitativa de la integridad del revestimiento de los ductos enterrados; su base teórica permitió el desarrollo de su instrumentación, metodología de campo y técnicas de procesamiento e interpretación de datos. La SEMPI se aplica en dos etapas: regional y local. La etapa regional incluye mediciones de campo magnético, voltaje y resistividad (ρ_s) del suelo, donde el principal resultado es la resistencia eléctrica del revestimiento (T_c) a lo largo del ducto, como indicador de la calidad del revestimiento. Una escala semaforizada de los datos de T_c permite clasificar la calidad del revestimiento como buena (verde), regular (amarilla) y pobre (roja). La etapa local incluye mediciones detalladas del campo eléctrico en tramos anómalos (T_c < 50 Ohm.m) localizando los daños en el revestimiento con una precisión de ± 0.5 m. Durante la etapa local se calcula el área desnuda equivalente por metro de ducto inspeccionado. En este trabajo se presentan los resultados de la aplicación de las etapas regional y local de la tecnología SEMPI en dos ductos situados en el sureste de México.

Palabras clave: inspección electromagnética superficial de línea de ducto; revestimiento del ducto; resistencia eléctrica del revestimiento.

Abstract

There are several surface inspection methods to evaluate the integrity of the steel pipe coating, obtaining acceptable qualitative results in some soil types and low complexity pipeline systems. However, these methods do not determine the necessary parameters for a quantitative evaluation of coating quality. The Mexican Petroleum Institute has developed Surface Electromagnetic Pipeline Inspection (SEMPI) technology for the quantitative assessment of buried pipeline coating integrity. SEMPI is a theory-based technology that enables the development of instrumentation, field methodology, as well

**Corresponding author: omar.delgado@ipicyt.edu.mx*

[1]*Instituto Potosino de Investigación Científica y Tecnológica, San Luis Potosí, Mexico.*

[2] *Instituto Mexicano del Petróleo Mexico City, Mexico*

[3] *Department of Geophysics, Faculty of Geology, Moscow State University, Rusia*

as data processing and interpretation techniques. The application of SEMPI consists of two stages: regional and local. The regional stage includes magnetic field, voltage and, soil resistivity (ρ_s) measurements, where the main result is the determination of the electrical resistance of the coating (T_c) along the pipeline as an indicating parameter of the coating quality. A scale signalized from T_c data allows classifying the quality of pipe coating as good (green), fair (yellow) and poor (red). The local stage includes detailed electric field measurements of on anomalous pipeline sections (T_c < 50 Ohm.m), locating damage in the coating with a detection accuracy of the ± 0.5 m. The equivalent unlined (holiday) area per meter of the inspected pipeline is calculated during the local stage. This work presents successful results from the implementation of regional and local stages of SEMPI technology in two pipelines located in the southeast region of Mexico.

KEY WORDS: surface electromagnetic pipeline inspection; pipe coating; coating electrical resistance.

INTRODUCTION

Corrosion is the chemical process of the environment through which metals try to return to their original or mineral state (Roberge, 2018). In the case of buried pipelines, metals are exposed to corrosive processes that may eventually cause ruptures with the consequent environmental and economic damages (Beavers and Thompson, 1997). The pipe coating forms the main barrier against external corrosion by providing excellent protection; however, over time the coating deteriorates due to water absorption, tension and aggression caused by the soil and bacterial action, among others. Once the coating is damaged, the metal surface is exposed to the electrolyte medium (soil and/or water), the metal loses mass and, if this condition persists for some time, corrosion process and hydrocarbon leakage occur.

Oil spills have numerous effects on the environment and the economy, damaging waterways, animal life and plants. The main sources of hydrocarbon contamination are pipelines (Delgado *et al.*, 2006), from small and permanent leakages up to a full collapse of the pipe. Therefore, external and internal inspections of pipelines are required to assess their integrity, as well as to determine the technical characteristics and their variations during the exploitation process.

The quality of the insulator coating determines the optimal strategy of the pipeline maintenance and the appropriated performance of the cathodic protection (CP) system (Morgan, 1993). The coating acts as an electrical insulator preventing electrical contact between the soil and the pipe (corrosion processes) and CP leakage current. Generally, in order to estimate the coating quality, electrical and electromagnetic (EM) non-destructive methods are applied on the surface. To detect coating damage, Direct Current of Voltage Gradient (DCVG) (Leeds and Grapiglia, 1995; Nicholson, 2007; DCVG, 2008) and Pipeline Current Mapper (PCM) (Radiodetection, 2009) methods are widely applied. These methods are based on measuring the electric potential and electrical currents along a pipe and the leakage current from a pipe to earth through the defects or damage in the coating. The main difference between these methods consists of the type of measurements: electric (DCVG measuring electrical potential with the aid of electrodes in contact with the soil (Masilela and Pereira, 1998)) or magnetic (PCM measuring magnetic field using one or more contactless sensors (Furquim, 2005; Radiodetection, 2009)). In case of DCVG, relations between voltage drops and direct observations made on pipe coating through excavations have been used to predict coating defect area (Anes-Arteche *et al.*, 2017). However, DCVG and PCM provide only qualitative information about the location of the leakage current and their results can be strongly affected by changes in soil resistivity (Mckinney, 2006), as well

as by neighboring pipelines when the distance between pipes is comparable with (or less than) their depth. The main drawbacks in pipeline systems in Mexico are: corrosive soil characterized by a high clay content and low resistivity, pipeline interconnections including pipes that are out of service and the short distance between parallel pipelines compared to their depths, which reduces the possibilities for effective electrical or EM inspection based on surface measurements. Due to this, it is necessary to have inspection techniques that can determine the coating electrical resistance as a quantitative parameter of the coating quality. The Mexican Petroleum Institute has developed Surface Electromagnetic Pipeline Inspection (SEMPI) technology for quantitative assessment of the coating quality from parameters such as leakage current, leakage resistance and coating resistance. The application of SEMPI does not require the interruption of the pipeline operation and CP system.

In this paper, we present the SEMPI technology as a set of electric and EM methods that provide solutions to the aforementioned limitations. SEMPI technology is applied in two stages: regional (medium resolution) and local (high resolution). The adequate combination of both stages provides SEMPI with high efficiency and resolution.

During the regional stage, magnetic field measurements are performed in order to calculate the leakage current (Mousatov *et al.*, 2012). For the quantitative assessing of the coating quality, the leakage and coating resistances along the pipeline are determined using additional voltage and soil resistivity (ρ_s) measurements. The main calculated parameters in the regional stages are: electrical coating resistance as the pipe coating quality indicator and ρ_s as a measurement of the soil corrosivity rate.

To localize coating holidays and evaluate their exposed areas, which are often a small part of the total pipeline surface, SEMPI technology should include a high-resolution measurement stage. The local (high resolution) stage includes detailed Alternating Current Voltage Gradient (ACVG) measurements generated by leakage currents on the anomalous pipe sections identified in the regional stage, allowing the precise location of damage in the coating and the calculation of equivalent unlined (holiday) areas.

We present practical results obtained in Mexico that demonstrate their effective implementation in the aforementioned situations. Specifically, we show two successfully achieved results: (1) the inspection of a 4 *in* outside diameter (OD) buried gas pipeline where the application of local and regional stages allowed the location and quantification of severe coating damages in sections of the pipes and, (2) the inspection of a 4 *in* OD buried gas pipeline with coating affected by contact with another pipe.

DESCRIPTION OF SEMPI TECHNOLOGY

FIELD METHODOLOGY OF SEMPI TECHNOLOGY

SEMPI theory was developed in the Mexican Petroleum Institute by applying the principle of transmission lines (*TL*) as an approach to metal pipes (Chipman, 1968; Kaufman, 1989; Mousatov and Nakamura, 2001). The theory of *TL* has been used in the application of EM methods in studies such as to determine the formation resistivity in cased wells (Kaufman, 1989), the estimation of CP current (Morgan, 1993), and the detection of damaged coating (Mousatov *et al.*, 2012).

Based on the equivalent parameters of the *TL*, voltage and current distributions along the pipe

can be obtained. Voltage and current decrease along the pipeline as the distance increases from the generator connection point because the pipe has the finite resistance and part of current leaks through the pipe insulation. Taking into account the high conductivity of a metal pipe and the presence of a resistive insulating coating, we approximated the pipeline by *TL* using the distributed parameters (Mousatov and Nakamura, 2001). The pipeline with insulation damage (varied leakage resistance) can be analyzed as a non-uniform transmission line that consists of piecewise homogeneous segments where leakage resistance does not change over distance.

SEMPI includes two steps: regional measurements (medium-resolution) and detailed measurements (high-resolution).

1. Regional Stage of SEMPI

The implementation of the SEMPI regional or medium-resolution stage includes the following types of measurements: pipeline current (from the magnetic field) and voltages, and ρ_s.

During the regional stage, magnetic field measurements can be performed depending on the pipe route complexity, in two ways: along the pipeline and on profiles perpendicular to the pipes (Mousatov *et al.*, 2012). To carry out current and voltage measurements, EM signal (98 Hz – 625 Hz) generators and meters are used. Current measurements are performed along the pipeline at intervals of 10 m or on profiles perpendicular to pipes at intervals of 10 – 25 m between profiles (Mousatov *et al.*, 2012). Voltage measurements are made only in the control posts of CP system. Soil resistivity measurements are obtained along the profile parallel and separately ~ 7 - 8 m to the pipeline route using EM induction equipment EM31-MK2 (Geonics Limited, 2010) in horizontal polarization, i.e, for the case of both transmitter and receiver dipoles are horizontal coplanar, ensuring a maximum study depth of 3 m (McNeill, 1980). A Trimble GeoExplorer Geo XT 6000 Series (Trimble Navigation Limited, 2014) is used to obtain the UTM coordinates for sub-meter accurate.

For quantitative assessing of the coating quality, the leakage and coating resistances along pipeline are determined using additional voltage and ρ_s measurements. The main calculated parameters in the regional stages are: electrical resistance of the coating as a measure of coating quality and ρ_s as a measure of soil corrosivity.

1.1 Leakage current, leakage resistance and coating resistance.

The leakage current (I_l) is determined as the derivative or variation of I for a section of the pipeline.

Voltages values induced by the generator are measured at the control posts of the CP system. Taking into account the measured values, the function of voltage for the studied pipeline is determined using exponential functions. We have the voltage $V(x)$ and $I_l(x)$ for each measurements point (x) of the pipeline, then, using Ohm´s law, leakage resistance $T_l(x)$ is calculated using the following expression:

$$T_l(x) = \frac{V(x)}{I_l(x)} \tag{1}$$

T_l not only depends on the coating quality, but also on T_s (soil resistance), which is a function of ρ_s. By knowing T_l and T_s, it is possible to calculate T_c as a quantitative parameter of the pipeline coating integrity by:

$$T_c = T_l - T_s \tag{2}$$

Where: $T_s = K \cdot \rho_s$

K = geometrical constant that depends on the inner and outer radii of the soil hollow body around the pipe, considered in the calculation of T_s.

Equation (2) shows that T_c is the result of subtracting T_s from T_l, thereby removing the effect caused by variations in the soil resistivity on the leakage current magnitude. The magnitude of T_s around the pipeline proportionally influences the magnitude of I_l (and therefore, the magnitude of T_l). Now, we have a value of T_c that is not affected by variations in the ρ_s, which only depends on the coating integrity.

The calculated values of T_c are plotted on scale type traffic lights in order to define a priority level to repair the damages detected in the coating. The color scale of the T_c graph is based on the theoretical modeling of pipelines with different magnitudes and types of damaged coating, as well as on experience in the application of SEMPI technology in different geological and hydrogeological environments. T_c > 250 Ohm.m (green) indicates that although there may be some damage to the coating, this does not expose the pipe to corrosion processes (*good quality coating*). Values in the range 50 Ohm.m ≤ T_c ≤ 250 Ohm.m (yellow) indicate the existence of moderate damage to the coating (*regular quality coating*). The evolution of theses damages needs to be monitored in order to schedule future maintenance. Finally, T_c < 50 Ohm.m (red) indicates the existence of major damage to the coating, exposing the pipeline to corrosion processes (*poor quality coating*). Therefore, urgent repairs are required.

2. Local stage of SEMPI

Theoretical basis

The local or high-resolution stage includes detailed measurements of the electric field. In a homogeneous semi space, the potential U of a punctual source is:

$$U = \frac{I_l \cdot \rho_s}{4\pi}\left(\frac{1}{\sqrt{Z^2 + X^2}}\right) \tag{3}$$

Where U is the electrical potential, Z is the source depth, X is the distance on the X axis between the source and the measurement point, I_l is the leakage current from the source and ρ_s is the soil resistivity.

The horizontal components of the electric field (E_x, E_y) are determined using the following equations:

$$E_{x(1-2)} = \frac{I_l \cdot \rho_s}{4\pi}\left(\frac{1}{\sqrt{Z^2 + X_1^2}} - \frac{1}{\sqrt{Z^2 + X_2^2}}\right) \tag{4}$$

$$E_y = \frac{I_l \cdot \rho_s}{4\pi}\left(\frac{1}{\sqrt{Z^2 + X^2}} - \frac{1}{\sqrt{Z^2 + X^2 + Y^2}}\right) \tag{5}$$

Now, if we consider a type "L" electrode array with a separation between electrodes of 1 m, is placed on pipeline to obtain the electric measurements (Figure 1A) and the step between measurement points along the pipe axis is 1 m, the anomaly magnitudes E_x and E_y depend on the leakage current (I_l), pipe depth (Z), and ρ_s values (see equations (4) and (5). The measurements obtained are plotted in Figure 1B. The E_y anomaly is as simple as the U anomaly, while the E_x anomaly has two peaks separated by a minimum indicating the location of the source (Figure 1B). Due to this, in order to obtain the electric measurements in the local stage, only E_y will be measured using an electric dipole oriented perpendicular to the pipe (E_y), placing one electrode above the pipeline.

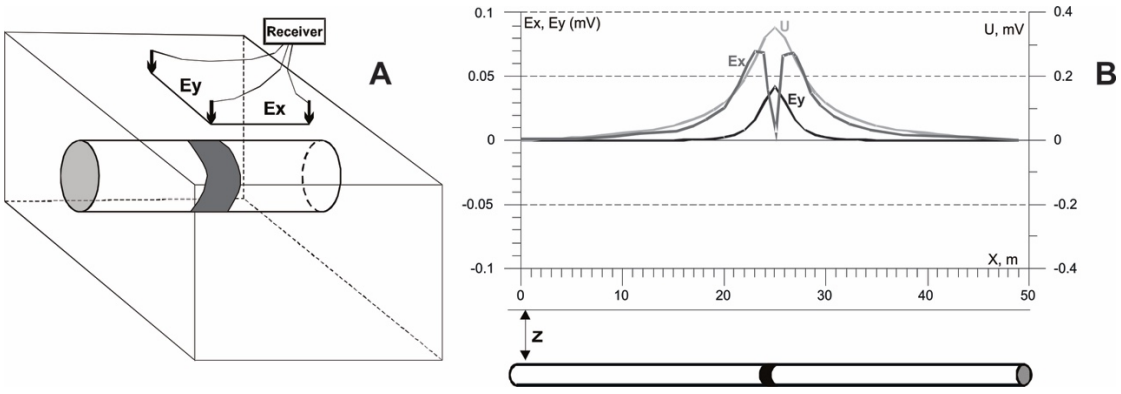

Figure 1. Electric field anomalies. A) Type "L" electrode array to measure the two horizontal components of the electric field on the pipe. B) Graphs of electric and potential field on pipeline with damaged coating at point 25 m. Z is equal to 1.5 m.

3. Field methodology of the local stage and quantitative interpretation of the Ey anomalies.

The interpretation of the E_y anomaly is required to determine the leakage current (I_l) from the sources (coating damages). The process considers the cases of discrete and continuous sources. Discrete sources are considered when anomalies are isolated or separated (distance between anomalies is greater than their widths). Continuous sources are considered when anomalies are distributed over a pipeline axis that is continuously causing interference between them, and it is not possible to locate each source separately. Both cases were verified by data interpretation from pipeline models with discrete and continuous sources, showing that the total current leakage determined for discrete and continuous sources is equal and that both models are equivalent.

The interpretation process has a standard structure, complying with the following stages: initial model creation, calculation of fitting error between measured and calculated electric fields for

the initial model, and finally, the fitting error minimization procedure. The E_y anomaly is used as an initial model, assuming that the leakage current value is equal to the electric field. Based on this model the algorithm converges faster.

The detailed measurements of electric field E_y on anomalous pipeline sections identified in the regional stage, in intervals of 1 m, allow the precise location of damages in the coating and its quantitative evaluation by the calculation of an unlined (holiday) equivalent area.

The intensity of the electric field in the soil surrounding the pipeline induced by leakage current (I_l) is measured using an electric dipole perpendicularly oriented to the pipeline, placing one electrode above the pipe's axis. Knowing the measured voltage difference (ΔU_y) between the M and N electrodes, ρ_s, pipe depth (Z) and electric dipole length, it is possible to estimate the magnitude I_l, using equation (5).

For each anomalous pipeline section, V values can be determined from the voltage distribution obtained during the application of the regional stage. By equations (1) and (2), T_l and T_c values, in intervals of 1 m on anomalous pipeline, are calculated, allowing the precise location of damage to the coating. If we consider T_i as the perfect or ideal condition of pipe coating, it is possible to determine the percentage of equivalent holiday area (EHA) for each meter of pipeline inspected by the electric field according to the expression:

$$EHA(\%) = \frac{T_s \cdot (T_i - T)}{T \cdot (T_i - T_s)} \cdot 100 \tag{6}$$

The estimation of EHA provides a high-resolution quantitative assessment of the coating quality. Values of EHA> 5% indicate significant damages to the coating.

The local stage offers high-resolution results, but electric field measurements are slower than magnetic field measurements (regional stage). The implementation of the regional stage allows an overall assessment of the condition of the pipeline coating by defining the sections that require a detailed inspection in the local stage. The joint application of magnetic and electrical methods allows us to optimize the coating inspection works.

In conclusion, the application of both stages of SEMPI can solve the following problems: (1) location of the pipelines on the surface and at depth, (2) quantitative estimation of the coating quality, (3) detailed location of damages in the coating, (4) estimation of EHA (%) for each linear meter (5) and soil corrosivity assessment based on ρ_s values.

SEMPI Instrumentation and Software

We have developed electromagnetic instruments to properly evaluate the insulation coating. The SEMPI instrumentation includes: a high power generator, a unified receiver for measurements of the magnetic-field, electric-field and voltage, induction antennas as magnetic field sensors and the SITIEMS software for processing and interpreting experimental data (Figure 2).

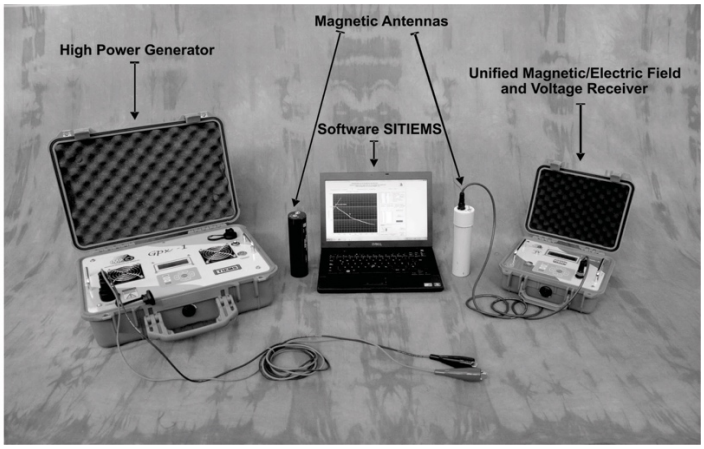

Figure 2. High power generator, unified magnetic-field, electric-field and potentials receiver, magnetic antennas and SITIEMS software.

The equipment developed is robust and able to work in different geographical and weather conditions. The high-power generator, high-resolution receiver and high-sensitivity antennas (Figure 2, Table 1), allow for the recording of reliable field data in pipeline routes under complex conditions (nearby pipelines and resistive subsoil).

Table 1. Technical Specifications of the SEMPI Instrumentation

High Power Generator	Unified Receiver	Antennas
Input Power: 117 VAC; 5 A; 60 Hz	Maximum Input Voltage: 1.8 V	High Sensibility: 20 mV/ (mA/m)
Output Power: 400 VA	Resolution: 20 nV	Input Signal Sinusoidal
Maximum Output Voltage: 100 VAC	Input Frequency: 1, 2, 4, 8, 98, 512 and 625 Hz	Input Frequency: 98, 512 and 625 Hz
Output Current: 0.1, 0.25, 0.5, 1, 1,5, 2, 2.5, 3, 3.5, and 4 A	Digitally Programmable Gains: 1, 2, 5,10, 20, 50 y 100	High Permeability Ferrite
LCD Display	*LCD Display*	Operating Temperature: -20°C to +95°C
Output Current Precision: ±0.002 A.	*Signal Strength Indicator*	Maximum Operating Humidity:70 %
KeyPad: 9 Functions Keys	*KeyPad: 9 Functions Keys*	Whether Resistance Case
Output Frequency: 1, 2, 4, 8, 98, 512 and 625 Hz	50 Hz and 60 Hz Power Line Rejection	Dimensions: Cylinder, Ø=5 cm, h=19.5 cm
Frequency Precision: ±0.1% Hz	Operating Temperature: -20°C to +55°C	Weight 1.5 Kg
Operating Temperature: -20°C to +55°C	Two Internal Rechargeable Batteries	
Maximum Operating Humidity: 70 %	Maximum Operating Humidity:70 %	
Whether Resistance Case	Whether Resistance Case	
Dimensions: 47 x 35.7 x 17.6 cm	Dimensions: 27 x 24.6 x 12.4 cm	
Weight: 10 Kg	Weight: 3.5 Kg	

RESOLUTION OF SEMPI

CASE 1: COATING DAMAGES AS HOLIDAY OR DISBONDMENT.

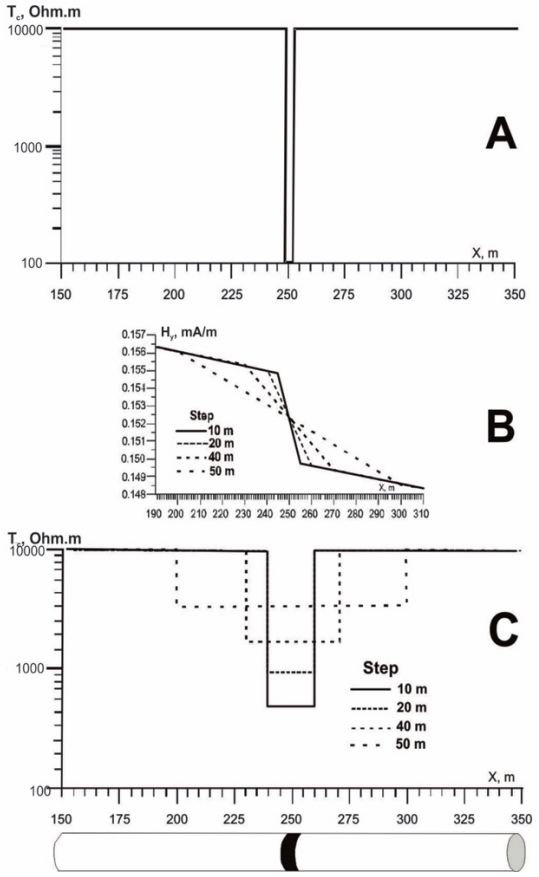

Figure 3. A) Model of pipe with damaged coating at interval 249 to 251 m, with coating resistance (T_c) values of damaged coating = 100 Ohm.m and coating in good condition, T_c = 10,000 Ohm.m. B) Magnetic field measured for different measurement intervals.

The holiday or disbondment area is often a small part of the pipeline surface through a significant magnitude of current leaks to the soil. High resolution is required to find these small damages. To study the resolution in determining coating damage, we analyzed the distributions of the magnetic field along the pipe as a function of the distance between the measurement points. Figure 3A shows a pipe with severe damage in the coating in the interval 249 m to 251 m (T_{c2} = 100 Ohm.m). In the intervals $0 \leq x < 249$ m and $251 < x \leq 500$ m, the coating quality is perfect ($T_{c1} = T_{c3}$ = 10,000 Ohm.m). The model includes the following metal pipe parameters: conductivity $\sigma = 10^7$ Ohm/m, OD = 0.2 m, wall thickness Δr = 0.01 m. The AC generator (625 Hz) is connected to the starting point of the pipeline (x = 0 m). The proposed distances between measurement points along the pipeline were: 10, 20, 40 and 50 m.

Figure 3B shows the behavior of the magnetic field (H_y) obtained for different lengths of the measuring step. The resolution of the technique depends on the measurement interval of the magnetic field. When the measuring step increases the resolution in the localization (Figure 3B) and quantification (Figure 3C) of the damaged coating decreases. For example, for the 10 m and 20 m steps, the leakage current anomaly shows damaged coating in a pipeline section length 20 m (medium resolution), with T_c = 650 Ohm.m, considerably less than 10,000 Ohm.m; the 50 m step locates a longer pipeline section (low resolution) with a T_c value (5,000 Ohm.m), which is less anomalous than those determined for shorter measurement steps. However, even for large measurement steps (e.g. 50 m), the leakage current through the damaged coating is expressed by a fall in the magnitude of H_y. This feature provides the implementation of magnetic field measurements that are more productive and efficient than electrical measurements (DCVG or ACVG methods), which require measurements at short steps (e.g. 1 m) to detect the current leakage caused by the damaged coating.

Case 2: Deteriorating and weakening of coating.

The deterioration or weakening of the coating may include the presence of small fractures, pores, or the thinning of coating, in small or large areas of the coating surface. The magnitude of leakage current per lineal meter is less than the leakage current from a holiday area.

Figure 4 shows a section of pipeline with coating damaged by pores and fractures distributed in the interval 175 m to 310 m, reaching the minimal values of T_c = 650 Ohm.m in the interval 240 m < $x \leq$ 250 m. In the intervals 150 $\leq x <$ 175 m, and 310 < $x \leq$ 350 m the coating quality is perfect (T_c = 10,000 Ohm.m). The pipe model (Figure 4A) includes the same pipeline parameters as those used in the model for Figure 1, as well as the measurement steps (Figures 4B and 4C). Following the example of Figure 4, we have falls in the H_y field in all measuring steps, whereas each T_c graph (Figure 4B) shows different resolution levels according to the measuring step. The T_c graph for the 10 m step (Figure 4B) is similar to the pipe model (Figure 4A).

SEMPI is designed to perform magnetic field measurements in intervals of 10-50 m to identify damaged sections of pipeline. Therefore, SEMPI technology is effective both for localization and quantification of pipe sections with holiday-disbondment (punctual) type coating damage, as well as coating damage formed by a set of pores and fractures distributed along pipeline. Subsequently, local measurements will be applied in these detected sections in order to accurately locate the damage to the coating, these being the EM technique; thereby optimizing time and cost for their application in extensive pipeline routes.

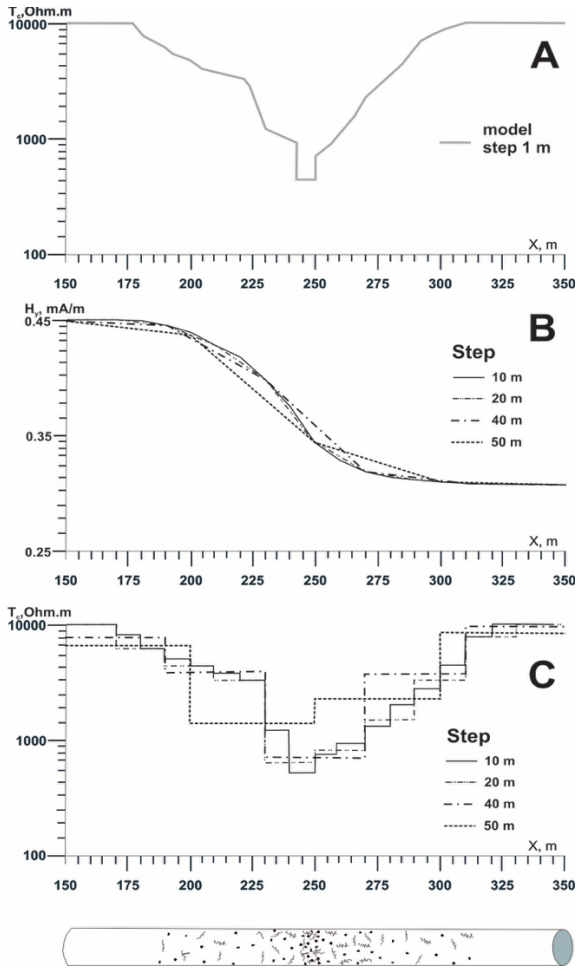

Figure 4. A) Model of pipe with irregular deteriorating (pores and fractures) of coating in the 175 m - 310 m pipe section, and coating in good condition (T_c = 10,000 Ohm.m) in the 150 m – 175 m and 310 m – 350 m sections. B) Magnetic field measured for different measurement intervals. C) Coating resistance recalculated from different measurement steps.

PRACTICAL EXAMPLES OF APPLICATION OF SEMPI TECHNOLOGY

SEMPI has been applied in experimental studies of pipeline technical conditions in several places in Mexico. We present two practical cases of application of this technology for inspection of buried pipelines in Southeast Mexico.

A soil resistivity profile parallel (and separately ~ 7 m) to the pipeline route was obtained using EM induction equipment EM31-MK2 (Geonics Limited, 2010) for a maximum study depth of 3 m.

CASE 1: LOCALIZATION AND QUANTIFICATION OF HOLIDAY IN BURIED GAS PIPELINE.

SEMPI was applied for the inspection of a 4 *in* OD gas pipeline located in the state of Tabasco, Mexico. The inspected pipe length was 11.2 km and it passes through dry silt-loam soil.

The generator, at a frequency of 512 Hz, was connected to the pipeline at the control point of the cathodic protection system. Perpendicular profiles to pipe axis were taken with step measurements of 0.5 m. The spacing between profiles was 25 m.

The leakage current is determined as the derivative or variation of the current along the pipeline. By equation (1) T_l values are calculated. The EM profiling method was applied in order to obtain the ρ_s values along pipeline route and, then, T_s values are calculated (equation (2)). In wetlands, water salinity values were determined at measurement points near to the pipeline. From equation (2) the T_c values were determined.

Figure 5 shows the T_c graph for the inspected pipeline, confirming that SEMPI is able to not only to locate, but also adequately quantify coating damages. Based on the results shown in Figure 5, some representative points of the condition of pipeline coating (green, yellow and red zones) were selected to carry out detailed electric measurements for precise localization and quantification of the damages in the coating.

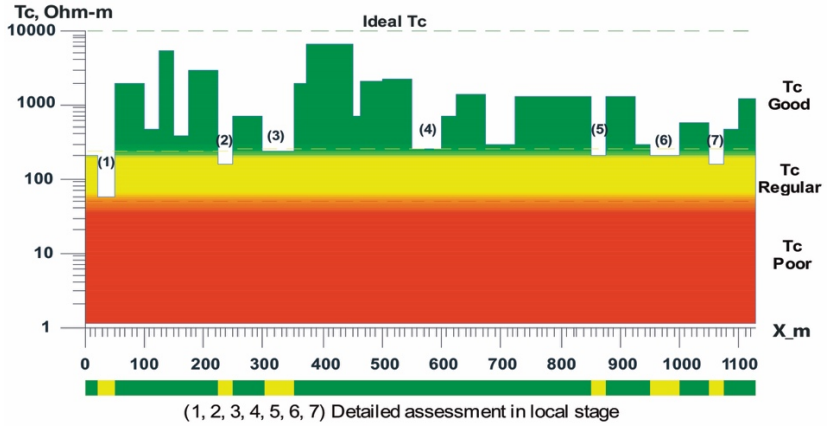

Figure 5. Coating resistance (T_c) graph, indicating zones with regular quality coating.

Evaluation of soil corrosivity

Some soil parameters are taken into account to assess their corrosiveness, mainly electrical resistivity and pH (Schwerdtfeger, 1965). Electrical resistivity depends closely on soil moisture and the salinity of pore-water, therefore it is an effective indicator of soil corrosion level. Low soil resistivity values are related with high corrosivity and the opposite is also true, being commonly used to assess corrosion potential in underground pipelines (Putra *et al.*, 1977). The classification of soil corrosivity based on resistivity values is shown in Table 2.

Table 2. Soil corrosivity rating based on resistivity values (Roberge, 2012).

Soil resistivity (Ohm.m)	Corrosivity Rating
>200	Essentially non-corrosive
100 to 200	Mildly corrosive
50 to 10,000	Moderately corrosive
30 to 50	Corrosive
10 to 30	Highly corrosive
<10	Extremely corrosive

The ground resistivity around the pipe was estimated every 25 m using EM induction equipment EM31-MK2 (Geonics Limited, 2010) in a horizontal polarization, ensuring a maximum study depth of 3 m. Soil resistivity measurements are needed for the calculation of T_s. These measurements can also be used to estimate the aggressiveness degree or corrosivity rating of soils based on electrical resistivity values (Roberge, 2018). The majority of soil along the pipeline route is moderately to mildly corrosive, exceeding 100 Ohm.m (resistive soil) in some parts of the pipeline route values; only in anomalous zones (1) and (4) (Figure 5) is the soil is classified as corrosive (ρ_s < 50 Ohm.m).

Figure 6 shows the results achieved from the application of the local stage in the anomalous area (4) (pipe interval 540 m – 605 m, see Figure 5), where electric field measurements were performed at interval of 1 m (Figure 6A). The experimental data of the electric field are used in an inversion process by taking into account voltage, soil resistivity and pipe depth values, resulting in the fitting of the theoretical and experimental curves and the determination of the T_c and EHA (%) values for each lineal meter of the pipeline (Figure 6B). Two minimum values of T_c are determined at points 554 m and 586 m, reaching EHA values of 35% and 29%, respectively.

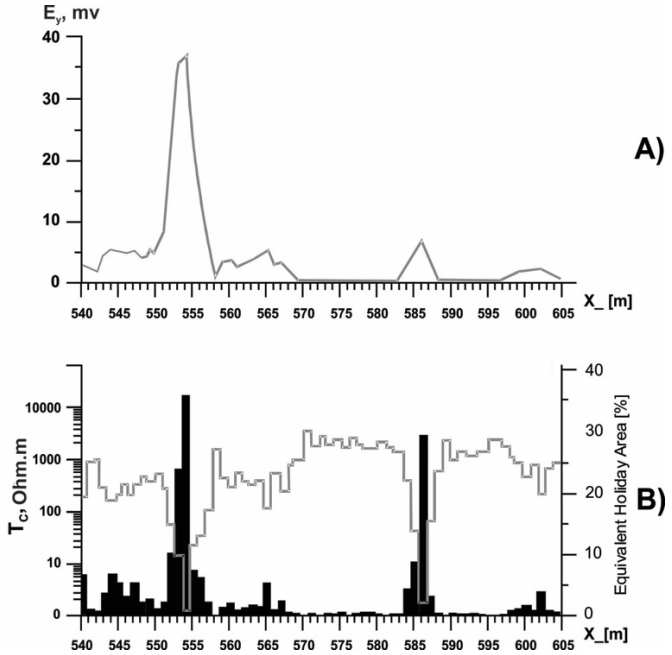

Figure 6. Results obtained from local stage of SEMPI applied in the anomalous pipeline interval 540 m - 605 m determined in the regional stage (see Figure 4). A) Electric field measurements. B) Detailed T_c values and EHA percentage.

Subsequent excavations were carried out at every (1 to 7) anomalous interval determined in the regional stage of SEMPI. Figure 7A shows the 1.5 m x 2.5 m excavation carried out at the pipe anomalous interval 4 (see Figure 5), which confirms the existence of severe damage (holiday) to the insulation coating at point 554 m (Figure 7B) causing a major leakage current from the cathodic protection (CP) system and, consequently, corrosion processes. This result confirms that SEMPI is able, not only to locate, but also to adequately quantify coating damage.

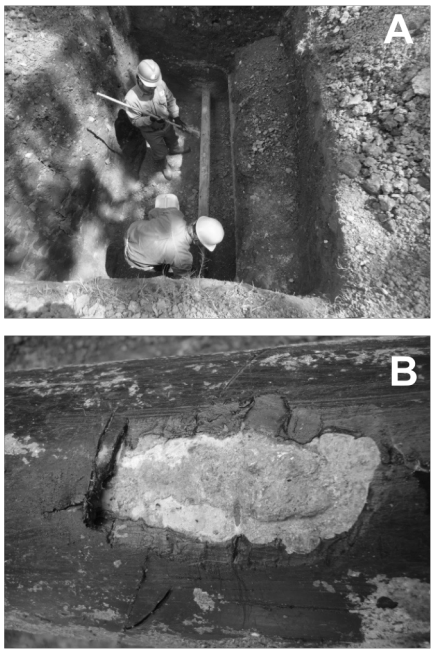

Figure 7. Verifying the main anomalies detected and quantified by SEMPI technology. A) Excavation performed in the pipeline interval 540 m – 605 m. B) Zoomed view of the coating damage located at point 554 m.

CASE 2: DAMAGES IN THE COATING CAUSED BY CONTACT BETWEEN PIPES.

In order to evaluate the coating quality of a 4 *in* OD gas pipeline of 2.4 km length, the local and regional stages of the SEMPI were performed. Through the application of the regional stage the T_c values obtained (Figure 8) show an overall good condition of the coating with a mean value of T_c = 2,438 Ohm.m (Figure 8), reaching in some pipe intervals the ideal value of 10,000 Ohm.m. In some small intervals there are low T_c anomalies. Most T_c anomalies indicate moderate damage to the coating (yellow zone, Figure 8). However, the pipeline interval 670 m - 700 m presents severe damage in the coating (red zone, T_c = 30 Ohm.m, Figure 8). This critical pipeline interval must be inspected at high resolution through the application of the local stage of the SEMPI.

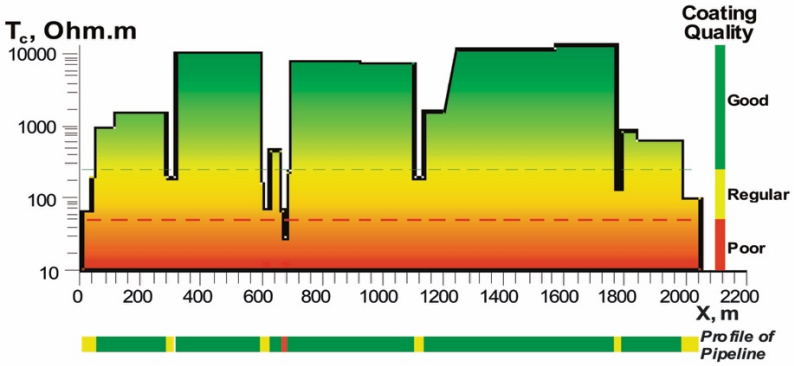

Figure 8. Coating resistance (T_c) for the 4 in OD gas pipeline. T_c graph indicate a zone with poor quality coating at interval 670 m - 700 m. Plan view of the pipeline with the T_c color scale is presented below the T_c graph.

The electrical resistivity of soil surrounding the pipeline has a mean value of 35 Ohm.m, being classified as corrosive. Three water samples collected along the pipeline route show low salinity (0.35 g/l); however, the high clay content of soil (low resistivity of soil) could facilitate corrosion processes. At the pipeline anomalous interval 674 m - 692 m, detailed electric field measurements were performed. T_c and the equivalent unlined area, with a 1 m step, were determined.

Figure 9 shows the detailed behavior of T_c, observing a minimum of 10 Ohm.m in the interval X = 681-682 m. The EHA reaches a maximum of 13% at X = 682 m, as a point where pipeline has critical damage to the coating. At the point X = 682 m an excavation (Figure 10A) was conducted which confirms the existence of physical contact between the 4 *in* OD gas pipeline and the 10 *in* OD oil pipeline (Figure 10B). This physical-electrical contact between pipes produces a major leakage current from the CP system and, consequently, corrosion processes.

We recommended repairing the pipeline coating at the point X = 682 m and the installation of devices to electrically isolate both pipes, thus optimizing the CP system of the 4 *in* OD gas pipeline.

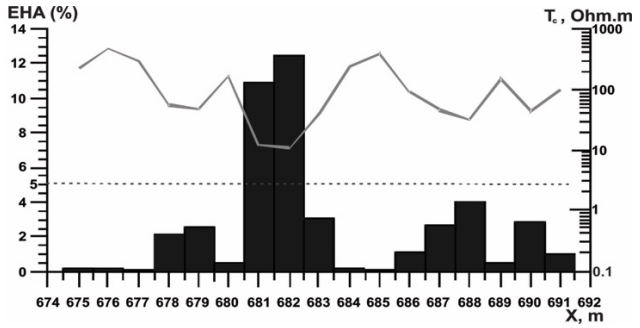

Figure 9. EHA and Tc values, for the anomalous 4 in OD gas pipeline interval 674 m - 692 m, determined in the local stage.

These results demonstrate the optimal application of a regional magnetic field measurements stage, then detailed measurements of the electric field on regional anomalies zones, obtaining accurate results without affecting the efficiency of SEMPI technology.

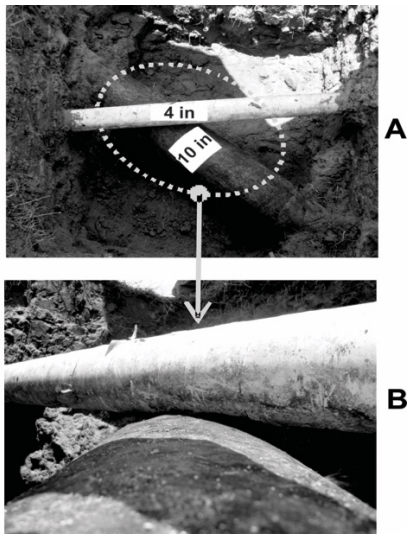

Figure 10. Excavation at X = 682 m of 4 *in* OD gas pipeline. A) Plan view of the excavation with pipelines crossing. B) Zoomed view of the contact between pipes that causes damage in the coating.

CONCLUSIONS

SEMPI technology was developed on the basis of *LT* theory, which allows the modeling of different types of pipe coating damages (holiday, disbondment, pores, fractures), as well as different types of soil surrounding the pipeline. The main result of SEMPI is the determination of the coating resistance (T_c) values along the pipeline, which indicate the quality of the pipe coating.

SEMPI technology consists of two stages: a regional or medium resolution consisting of fast magnetic field (pipe current and voltage) and soil (and water salinity) resistivity measurements, and local stage or high resolution based on the electric field measurement.

The efficiency and high resolution of SEMPI lies in the implementation of the regional stage that defines the pipeline intervals with a similar coating quality, then a local stage in order to locate and quantify the coating damages detected in the regional stage. The application of both stages gives SEMPI technology a high efficiency and resolution.

Finally, in this work successful results from the application of SEMPI technology in pipelines located in the southeast region of Mexico were presented, showing the effectiveness of SEMPI technology in determining the coating integrity of pipelines buried both in corrosive (conductive) soil, in soil with a low corrosivity rating, as well as physical-electrical contact with another pipeline.

ACKNOWLEDGEMENTS

The authors consider as a pleasant debt to express gratitude to the Pipeline Integrity Program of Mexican Petroleum Institute for support this research and permission to publish the obtained results.

REFERENCES

Anes-Arteche F., Yu K., Bharadwaj U., Lee C., Wang B., 2017, Challenges in the application of DCVG-survey to predict coating defect size on pipelines. *Electrochemical Sciences Advances*, 68, 3, 329-337.

Beavers J. A., Thompson N. G., 1997, Corrosion beneath disbonded pipeline. *Materials Performance*, 36, 13–19.

Chipman R. A., 1968, Theory and problems of transmission lines. McGraw Hill, USA.

DCVG, 2008, Principle of the DCVG Technique. DC Voltage Gradient Technology and Supply LTD. http://dcvg.co.uk/wp-content/uploads/2019/04/029-Principle-Of-The-DCVG-Technique-2008.pdf

Delgado-Rodríguez O., Shevnin V., Ochoa-Valdés J., Ryjov A., 2006, Geoelectrical characterization of a site with hydrocarbon contamination caused by pipeline leakage. *Geofísica Internacional*, 45, 1, 63-72.

Furquim J. A., 2005, Locating, mapping and assessing pipeline coating using the pipeline current mapper (PCM) method (in Postuguese). *Rio Pipeline Conference & Exposition*, 1-8.

https://www.osti.gov/etdeweb/servlets/purl/20897615

Geonics Limited, 2010, EM31-MK2 (with Archer), Operating manual, Ontario, Canada. http://www.geonics.com

Kaufman A.A., 1989, Conductivity determination in formation having a cased well. United States Patent No. 4,796,186.

Leeds J.M., Grapiglia J., 1995, The DC Voltage-Gradient Method for Accurate Delineation of Coating Defects on Buried Pipelines. *Corrosion Prevention and Control*, 42, 4,77-86.

Mckinney J. P., 2006, Evaluation of above-ground potential measurements for assessing pipeline integrity. Thesis for the degree of Master of Science. University of Florida, 71 pp.

McNeill J.D., 1980. Electromagnetic terrain conductivity measurement at low induction numbers. Geonics Limited, Technical Note TN-6, 15 pp.

Masilela Z., Pereira J., 1998, Using the DCVG technology as a quality control tool during construction of new pipelines, *Engineering Failure Analysis*, 5, 2, 99-104.

Morgan J., 1993, Cathodic Protection. National Association of Corrosion Engineers (NACE), 2nd edition, Houston, TX, USA, 519 pp.

Mousatov A. and E. Nakamura, 2001, Transmission-line approximation of pipelines with cathodic protection. SAGEEP-2001, Denver, USA, Expanded Abstracts, 11 pp.

Mousatov A., O. Delgado-Rodríguez, E. K. Nakamura-Labastida, V. Shevnin, 2012, Technical inspection of pipeline groups using surface electromagnetic methods. *Near Surface Geophysics*, 10, 2, 129-140.

Nicholson J. P., 2007, Combined CIPS and DCVG survey for more accurate ECDA data. World Pipelines, 7, 11, 1-6.

Putra R., Yusuf M., Huzni S., Ali N., Fonna S., 1977, Effect soil resistivity in mapping potential corrosion in underground pipelines area. AIP Conference Proceedings. https://doi.org/10.1063/1.5042981.

Radiodetection, 2009, Pipeline Current Mapping system. Operating manual, issue 4, Bristol, United Kingdom, http://www.radiodetection.com

Roberge P.R., 2012, Handbook of Corrosion Engineering. New York, N.Y., McGraw-Hill., 2nd edition, 1088 pp.

Roberge P.R., 2018, Corrosion Basics: An Introduction. National Association of Corrosion Engineers (NACE), 3nd edition, 822 pp.

Schwerdtfeger, W. J., 1965, Soil Resistivity as Related to Underground Corrosion and Cathodic Protection. *Journal of Research of the National Bureau of Standards*, 69C, I, 71-77.

Trimble Navigation Limited, 2014. Geoexplorer 6000 series. https://trl.trimble.com/docushare/dsweb/Get/Document-597676/022501-285E_Geo%20Series%206000_DS_0314_LR.pdf

Artículo original

https://doi.org/10.22201/igeof.00167169p.2021.60.3.2130

APUNTE GEOLÓGICO Y REVISIÓN HISTÓRICA DE LA ZONA GEOTÉRMICA DE PATHÉ, HIDALGO

Carles Canet[1,2], Sara I. Franco[2], Lucero Morelos-Rodríguez[3], Abdorahman Rajabi[4], Fernando Núñez-Useche[3]

Recibido: 5 de marzo, 2021; aceptado: 4 de abril, 2021; publicado en línea: 1 de julio, 2021.

RESUMEN

La zona geotérmica de Pathé, en el sector central de la Faja Volcánica Transmexicana, ha atraído la atención de exploradores y científicos desde finales del siglo XVIII. El ingeniero de minas alemán Joseph Burkart (1798-1870), contemporáneo de Alexander von Humboldt (1769-1859), elaboró en 1836 una descripción geológica de campo por la cual esta zona geotérmica puede considerarse la primera en México en haber sido investigada bajo los paradigmas de la ciencia moderna. A inicios del siglo XX la zona fue estudiada por el ingeniero José Guadalupe Aguilera Serrano (1857-1941), quien en 1907 describió las rocas eruptivas y sus productos de alteración. Su interés eran los yacimientos de caolín de Yexthó, situados a un km de las manifestaciones termales. A mediados del siglo XX la zona ya se prospectaba como fuente de energía geotérmica, lo que culminó en la primera planta geotermoeléctrica del continente americano, en operación entre 1959 y 1972 con una capacidad instalada de 3.5 MW.

Las manifestaciones termales de Pathé se ubican en la intersección de dos sistemas regionales de fallas normales, con rumbos N-S y E-W, y están encajonadas en una unidad volcánica (toba y lava) de composición básica a intermedia y edad Mioceno superior. Las alteraciones hidrotermales superficiales son conspicuas y su distribución está igualmente controlada por fallas pertenecientes a ambos sistemas. Asociada a las fallas N-S ocurre la asociación de alteración calcita-yeso, que involucra fluidos oxidados y alcalinos ricos en sulfato. Por otro lado, ligados a las fallas E-W —más tardías— se hallan los depósitos de caolín, producto de una alteración argílica avanzada, característica de zonas de condensación de vapor. Las condiciones del fluido indicadas por esta alteración son un pH muy ácido (2–3) y temperaturas cercanas a los 100 °C. Por su clara asociación con las fallas, así como por la ausencia de vulcanismo reciente (Cuaternario) cercano, Pathé se considera como un sistema geotérmico convectivo controlado por fallas. La sucesión de eventos de alteración sugiere que la actividad hidrotermal inició antes del Plioceno.

PALABRAS CLAVE: Joseph Burkart; José Guadalupe Aguilera Serrano; Faja Volcánica Transmexicana; alteración hidrotermal; caolín; fallas normales.

**Autor de correspondencia: ccanet@atmosfera.unam.mx*

[1]*Centro de Ciencias de la Atmósfera, UNAM*
Ciudad Universitaria, Coyoacán 04510
Ciudad de México, México

[2]*Instituto de Geofísica, UNAM*
Ciudad Universitaria, Coyoacán 04510
Ciudad de México, México

[3]*Instituto de Geología, UNAM*
Ciudad Universitaria, Coyoacán 04510
Ciudad de México, México

[4]*School of Geology, College of Science*
University of Tehran, Tehran, Irán

ABSTRACT

The Pathé geothermal zone, in the central portion of the Trans-Mexican Volcanic Belt, attracted a variety of scientists and explorers since late 18th century. Joseph Burkart (1798-1870), a German mining engineer and a contemporary of Alexander von Humboldt (1769-1859), provided in 1836 a geological description of the zone because of which Pathé was the first geothermal system to be studied in Mexico under modern science principles. At the beginning of the 20th century, this zone was investigated by the Mexican geologist José Guadalupe Aguilera Serrano (1857-1941), who described in 1907 the local volcanic rocks and their alteration. His main interest were the kaolin deposits of Yexthó, located one km to the west of the geothermal manifestations. By the middle of the century, the area was already explored for geothermal energy, which resulted in the first geothermal power plant in all America, operating between 1959 and 1972 with a nominal capacity of 3.5 MW.

The thermal manifestations of Pathé are located at the junction of two regional normal fault systems, striking N-S and E-W, and are hosted by a volcanic unit (tuff and lava) of basic to intermediate composition and Upper Miocene age. Surficial hydrothermal alteration is conspicuous and largely controlled by faults of these two systems. Associated with the N-S faults is a calcite-gypsum alteration assemblage, indicating oxidized, alkaline sulfate-rich hydrothermal fluids. On the other hand, linked to the later E-W faults are the kaolin deposits; they are the product of an advanced argillic alteration that is characteristic of a steam-heated environment and indicates acidic conditions (pH: 2 to 3) and temperatures around 100 °C. Because of its unambiguous relation to faults and the absence of recent (Quaternary) volcanism, Pathé is likely to be a fault-controlled geothermal system (non-magmatic, extensional domain type). The successive alteration events suggest that the hydrothermal activity is long-lived and dates back to before the Pliocene.

KEY WORDS: Joseph Burkart; José Guadalupe Aguilera Serrano; Trans-Mexican Volcanic Belt; hydrothermal alteration; kaolin; normal faults.

INTRODUCCIÓN

Por sus manifestaciones termales superficiales, antaño espectaculares, la zona geotérmica de Pathé (ZGP), en el límite noroccidental del estado de Hidalgo (colindante con Querétaro) (Fig. 1), atrajo desde finales del siglo XVIII la atención de exploradores y científicos. Pocos años después de las primeras relaciones documentales, las cuales aparecen en textos de carácter oficial y geográfico (Gómez Canedo, 1976; Ward, 1981), Burkart publicó en 1836 la primera descripción geológica de la zona, brindando detalles de la litología e incluso mediciones de la temperatura atmosférica y de las aguas termales. Por estos primigenios escritos de carácter técnico, Pathé se cuenta entre las primeras zonas geotérmicas de México en ser estudiada bajo los paradigmas de la ciencia moderna (*cf.* Morelos Rodríguez, 2012).

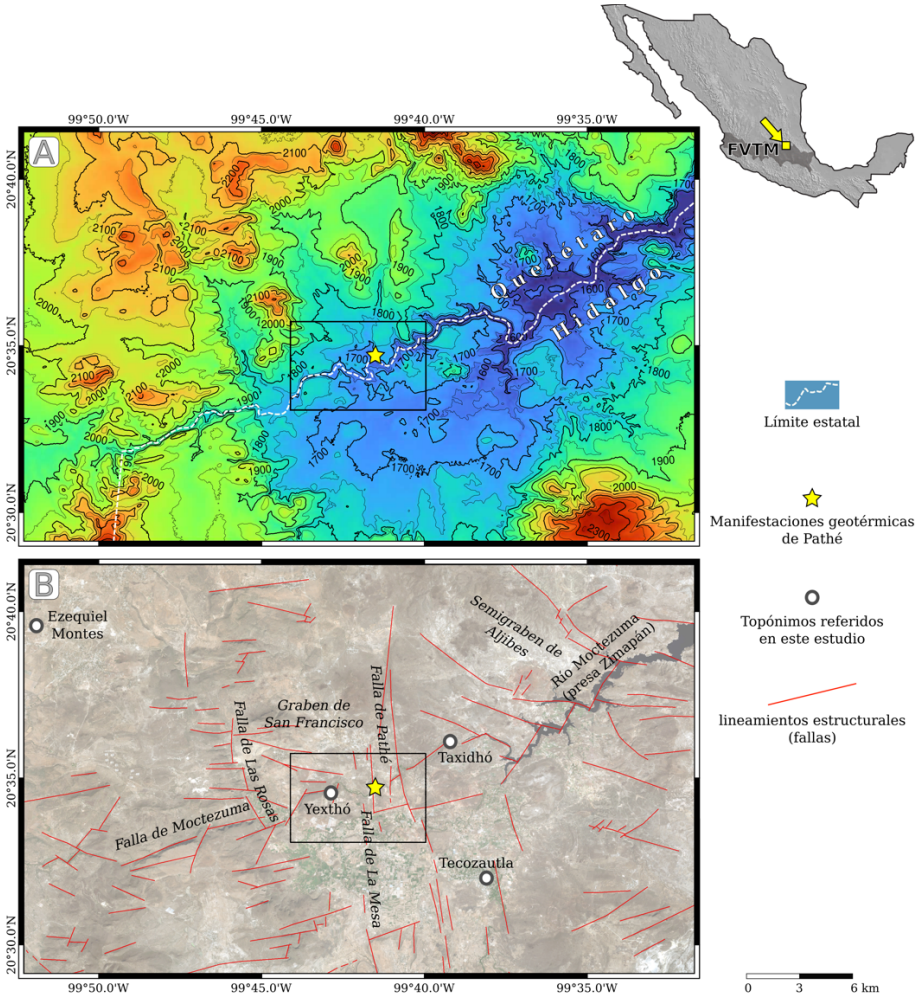

Figura 1. Mapas de ubicación de la zona geotérmica de Pathé, en la región limítrofe entre los estados de Hidalgo (municipio: Tecozautla) y Querétaro (municipios: Ezequiel Montes y Tequisquiapan). (A) Hipsometría (en m sobre el nivel del mar); (B) principales fallas y ubicación de topónimos citados en este trabajo. El recuadro corresponde al mapa geológico detallado de la zona geotérmica de Pathé, mostrado en la figura 5. La nomenclatura de las estructuras geológicas está basada en Carrillo Martínez (1998 y 2000), SGM (2007) e Hiriart Le Bert (2011). FVTM, Faja Volcánica Transmexicana.

A finales del siglo XIX e inicios del XX, en el marco de un proceso de institucionalización de la geología en México que buscaba documentar de manera sistemática y exhaustiva el territorio nacional desde un punto de vista geológico —con particular atención puesta en los recursos minerales—, se reavivó el interés por la ZGP, lo que condujo a nuevas investigaciones, enfocadas, en este caso, a los yacimientos de caolín de Yexthó (Figs. 1 y 2B), los cuales están espacial y genéticamente relacionados con los fenómenos hidrotermales del lugar (Aguilera, 1907).

Otra marca singular que ostenta la ZGP es haber tenido la primera planta geotermoeléctrica del continente americano, en operación entre 1959 y 1972 con una capacidad instalada de 3.5 MW (Hiriart Le Bert, 2011). Años después de su cierre, a partir de 1985, la zona se convirtió en un balneario de aguas termales, de nombre «Balneario El Géiser», desarrollado bajo un modelo de gestión comunitaria (Toscana Aparicio, 2017). El nombre se debe a que del antiguo pozo

productivo ('Pathé 1') emana una columna de vapor que frecuentemente es visible desde varios kilómetros de distancia (Fig. 2A). Este pozo y el edificio de la central eléctrica, además de algunas máquinas muy deterioradas, son los únicos testimonios que aún se conservan de la antigua planta, dentro de lo que hoy es un enorme complejo turístico que incluye un hotel con 650 habitaciones (Toscana Aparicio, 2017) (Fig. 3). El generador, que había sido adquirido el año 1958 en Larderello —la planta geotérmica más antigua del mundo, ubicada en la Toscana, Italia— se exhibe actualmente como una pieza de museo en el campo geotérmico de Los Azufres, Michoacán (Nieva *et al.*, 2013). En cuanto a las manifestaciones naturales descritas por los primeros geólogos que estudiaron la zona, no queda ningún vestigio de ellas.

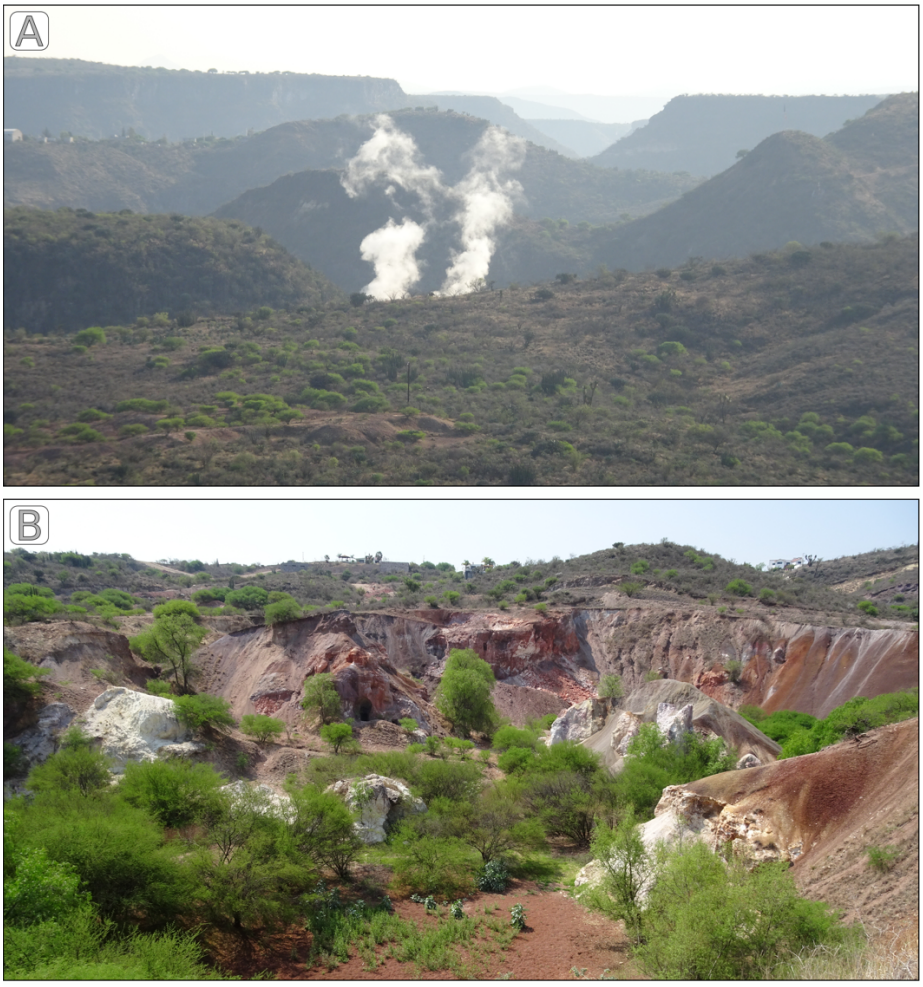

Figura 2. Vistas panorámicas de la zona geotérmica de Pathé. (A) Columna de vapor emanando del antiguo pozo geotérmico de Pathé, hoy día incluido en el complejo turístico-balneológico conocido como «Balneario El Géiser» (vista hacia el este); el relieve tabular que se observa hacia el fondo corresponde a lavas basálticas de la Unidad volcánica inferior (Mioceno superior). (B) Antiguas minas de caolín de la Hacienda de Yexthó (vista hacia el sur).

Figura 3. Vistas hacia el oeste sobre el «Balneario El Géiser», complejo turístico desarrollado a partir de 1985 en lo que fuera la planta geotermoeléctrica de Pathé —la primera del continente americano (operativa entre 1959 y 1972)—. El complejo se ubica en un surco tectónico de aproximadamente medio km de ancho y dirección N-S, producido por la Falla de Pathé, a la cual se asocia el graben de San Francisco (Carrillo Martínez, 1998), en su intersección con la Falla Moctezuma (SGM, 2007), de dirección WSW-ENE y asociada al semigraben de Aljibes (Suter *et al.*, 1995). En segundo plano, al centro de la fotografía, se observa en tonos amarillentos el escarpe de la Falla de Pathé.

Entre las más de 1380 manifestaciones geotérmicas inventariadas por la Comisión Federal de Electricidad (CFE) a lo largo y ancho del territorio mexicano (*cf.* Ordaz Méndez *et al.*, 2011), Pathé se incluye en el conjunto del ~20% de ellas con características de sistemas de media o alta entalpía (González-Ruiz *et al.*, 2015), cuyas temperaturas de reservorio (con base en geotermómetros) superan los 150 °C (Ordaz Méndez *op.cit.*). No obstante, no hay evidencia de que el sistema hidrotermal esté conectado con vulcanismo cuaternario (Hiriart Le Bert, 2011), antes bien se trataría un sistema gobernado por fallas normales activas (Nichols, 1970; Suter *et al.*, 1995; Carrillo Martínez, 1998).

A pesar de su relevancia histórica, singularidad geológica e interés económico —nutrido por sus recursos geotérmicos y minerales (no metálicos) y, además, por su actual aprovechamiento como balneario y por su potencial geoturístico—, son muy escasos los estudios publicados en las últimas décadas sobre la ZGP, destacando los que se enfocan específicamente a la geología estructural (Suter *et al.*, 1995; Carrillo Martínez, 1998 y 2000).

La presente contribución ofrece una revisión histórica de las investigaciones y exploraciones realizadas en la ZGP. Partiendo de ello, presenta un estudio original, de carácter cartográfico y descriptivo, acerca de la geología superficial de dicha zona (con énfasis en las alteraciones hidrotermales y su relación con las fallas), el cual pretende servir como marco actualizado de la geología del área.

Con este ensayo, los autores humildemente queremos homenajear al Ing. José Guadalupe Aguilera Serrano (1857-1941) y celebrar su contribución a la geología mexicana, exponiendo la vigencia de su estudio (Aguilera, 1907), publicado hace más de un siglo.

Revisión histórica

1. Contexto: el surgimiento e institucionalización de la geología en México

Antonio del Castillo (1820-1895), José Guadalupe Aguilera Serrano (1857-1941) y Ezequiel Ordóñez (1867-1951) fueron figuras sobresalientes y muy influyentes dentro de una generación de geólogos pioneros que, en la segunda mitad del siglo XIX, logró un hito sin precedentes en México: la fundación de la primera institución que se dedicaría exclusivamente al estudio geológico del territorio nacional. Así, en 1888, se creó por decreto presidencial el *Instituto Geológico Nacional* (IGN) (también conocido como Instituto Geológico de México), que debía documentar y estudiar los rasgos y fenómenos geológicos del territorio nacional bajo un triple enfoque científico-técnico-industrial. Entre sus cometidos se mencionaban: cartografiar desde el punto de vista geológico el territorio; caracterizar los tipos de suelos, rocas, minerales y materiales; así como el acopio, colecta, clasificación, conservación y exhibición de muestras de fósiles, rocas, minerales y tierras en el Museo Geológico Paleontológico de la Nación que debía desarrollar (Morelos Rodríguez y Moncada Maya, 2015).

En vísperas de recibir a la comunidad geológica internacional en el marco del Décimo Congreso Geológico Internacional, a celebrarse en 1906 en el país, los integrantes del IGN se constituyeron en una corporación científica que fue nombrada *Sociedad Geológica Mexicana* (SGM). El acto fundacional se celebró el 6 de diciembre de 1904, y se estableció el objetivo sustancial de «cultivar y propagar el estudio de la Geología y ciencias anexas, contribuir al adelanto de la Geología en general, y dar a conocer el suelo de México, tanto en sí mismo, como en sus relaciones con la minería, la agricultura y otras artes industriales» (SGM, 1904). Para asegurar la difusión de los estudios geológicos realizados por los socios, la SGM contó con el Boletín de la Sociedad Geológica Mexicana*,* instrumento de comunicación que se ha venido publicando desde 1905, siendo una de las revistas científicas más antiguas actualmente activas en México.

Entre 1904 y 1906, la SGM acometió resueltamente la exploración del territorio nacional, mediante al menos 31 excursiones por todo el país, lo que abonó para la primera versión de la Carta Geológica de América del Norte (a escala 1:5,000,000), resultado de la colaboración de los servicios geológicos de México, Estados Unidos y Canadá (USGS, 1911).

A comienzos del siglo XIX, el estado de Hidalgo había sido objeto de estudios geológicos y mineros particularmente detallados, debido a su profusa riqueza argentífera (Suter, 2016); ese interés resurgió hacia finales del mismo siglo e inicios del XX (*cf.* Aguilera, 1905). Es de suponerse que, durante alguno de los recorridos del IGN por dicho estado, haya nacido en el ingeniero José Guadalupe Aguilera el interés por explorar la zona, entonces remota, de los confines con el estado de Querétaro. En ese contexto, se publicó el artículo «Los kaolines [sic] de la Hacienda de Yexthó» (Aguilera, 1907), en el que se ofrecen detalladas y valiosas descripciones geológicas de la zona objeto del presente estudio.

2. Cronología de exploraciones y estudios en la zona geotérmica de Pathé

La primera visita documentada a la ZGP tuvo lugar en 1791, cuando un grupo de naturalistas de la Comisión Científica Novohispana, liderados por Antonio Pineda y Ramírez, realizó una expedición al Real de Minas de Zimapán (Suter, 2016). Desde este importante distrito minero se dirigieron a Tecozautla donde examinaron las manifestaciones ('baños') termales de Pathé

(Engstrand, 1981; González Claverán, 1988). De esos tiempos existe una primera referencia documental de la zona (escrita entre 1787 y 1792), correspondiente al borrador de un diario de un viaje de inspección a las «milicias de la Sierra Gorda», rescatado por Gómez Canedo (1976):

> *Andadas cuatro leguas de camino áspero y pedregoso, se encuentra la ranchería nombrada Patehé, tomando esta denominación, que en otomí significa agua caliente, de los hervideros de agua asufrosa que se hallan en la orilla del rio de San Juan, que atraviesa el camino. A distancia de otra legua se pasa el Arroyo de San Francisco, que sólo corre en tiempo de aguas, nase en los montes de Xilotepeqe y va a unirse con el Rio de Cimapán; y caminadas otras dos leguas se llega a Tecosautla, pueblo de suma fertilidad, cituado en una loma de tepetate. Su terreno es arenisco y tiene mucha agua; las calles son angostas, casi todas formadas de árboles, pero bien rectas y dispuestas con simetría. No pudo averiguarse en que tiempo se formó este pueblo, pero la iglesia y sus adornos manifiestan ser de mucha antigüedad. A 3 leguas desta población informan los vecinos hallarse las aguas thermales de Taxidío cuyos baños son muy ponderados por la bella temperatura de sus aguas, y por los innumerables enfermos que ocurren.*

Una vez que México obtuvo su independencia política de España, las autoridades del nuevo régimen abrieron las fronteras y los mercados para que inversionistas de otras naciones llegaran a la novel nación. En este escenario, diversos viajeros —con intereses también diversos— se aprestaron para visitar el país, como es el caso de Henry George Ward (1797-1860), diplomático e historiador británico encargado de los negocios de su país en México durante el periodo de 1825 a 1827, quien dedicó algunas páginas de su libro *Mexico in 1827* para describir el terreno de Tecozautla y las aguas termales de Pathé (Ward, 1981, 507):

> *Para ir de México hasta el Doctor existen dos rutas, una por San Juan del Río y Cadereita, y la otra, un camino de herradura, señalado en mi mapa de rutas según las indicaciones que me dio uno de los agentes de la Catorce Company.*
>
> *El distrito montañoso comienza al atravesar el río Tula, un poco hacia el sur de Tepetitlán (a catorce leguas de Huehuetoca), desde donde se extiende una sucesión de cerros empinados y áridos hasta la villa indígena de Tecosautla, situada en un valle bien regado y con abundancia de fértiles huertas. Después de Tecosautla el camino cruza el río Pate, en cuya vecindad hay manantiales de aguas minerales que despiden un denso vapor sulfuroso, y desde allí corre hasta el pie de una sombría montaña llamada Sombrerete, en la que se encuentra el rancho de Olveira. El rancho está a nueve leguas de Tecosautla y a cuatro del Doctor, lugar al que sin embargo es imposible llegar en un solo día.*

Desde el punto de vista geotérmico, fue el ingeniero de minas alemán Joseph Burkart (1798-1870), graduado de la Academia de Minas de Freiberg, Sajonia (actual Alemania) y contemporáneo de Alexander von Humboldt (1769-1859), quien realizó unas de las primeras descripciones de la zona comprendida entre Tecozautla y Zimapán. Este experto minero residió en México entre 1825 y 1834, trabajando en empresas mineras de capital alemán e inglés en los distritos mineros de Tlalpujahua, en Michoacán, y Veta Grande, en Zacatecas. Como resultado de su estancia redactó el libro *Aufenthalt und Reisen in Mexico in den Jahren 1825 bis 1834,* publicado en 1836 y nunca traducido al español. En la primavera de 1828 visitó varios distritos mineros después de dejar la empresa minera en Tlalpujahua

y antes de empezar su nuevo empleo en Veta Grande, Zacatecas. Desde la capital, quería visitar Zimapán y sus alrededores, para después dirigirse a Guanajuato, luego pasar a Zacatecas y finalmente ir a Durango, vía Mazapil, Catorce, Ramos y San Luis Potosí. Sin embargo, en aquella ocasión no le fue posible consumar su viaje hasta Durango, pero por otro lado se le facilitó conocer otras áreas que no tenía planeado visitar (Burkart, 1836). Así es como Joseph Burkart acabó realizando un reconocimiento geológico del terreno donde se asentaba la Hacienda de Pathé y una descripción de sus manifestaciones termales. Dada la relevancia de sus observaciones vertidas en su libro, en 1875, el naturalista mexicano Gumersindo Mendoza (1829-1886), miembro de la Sociedad Mexicana de Historia Natural, se dio a la tarea de traducir una sección de la obra del alemán que tituló «Notas sobre las fuentes termales de Pathé» para la publicación minera mexicana *El Propagador Industrial* (Mendoza, 1875):

> *Desde lo alto de la ribera izquierda del río Moctezuma, hacia el Oeste, el terreno es plano, y solo interrumpido por colinas de poca altura. Rumbo a Tecozautla, el terreno desciende, al grado de que esta población solo queda a 5,564 pies sobre el nivel del mar, pero ahí, rumbo a Cadereyta, vuelve el terreno a elevarse. El calcáreo moderno (¿del Jura?) y que yo observé en Huehuetoca y en el Valle de Tula, aquí, entre el río Moctezuma y Tecozautla, lo cubre una roca traquítica que aparece en muchos puntos. El terreno se compone, unas veces de un calcáreo amarillo gris, de poca densidad, de una textura desigual y sin fósiles; otras veces se compone de un conglomerado que encierra fragmentos traquíticos y doleríticos, unidos por un cemento calcáreo, terroso y raras veces denso.*
>
> *Al Oriente de Tecozautla, el terreno contiene algunas capas delgadas de una arenisca fina y desmoronadiza, manifestando claramente una estratificación horizontal. El pórfido, que en una masa feldspática, encierra cristales de feldspato vidrioso, surge en muchos puntos entre este calcáreo.*
>
> *Al Oriente [sic] de Tecozautla hay una masa feldspática color rojo de carne; los espacios avejigados están cubiertos de hialita, y en la masa total se hallan fragmentos grandes de un feldspato vítreo ligeramente colorido.*
>
> *De Tecozautla parte un camino, en una dirección Noroeste, (como a una y media leguas) cuyo piso es de la misma roca calcárea, hasta las inmediaciones de las fuentes termales de Pathé.*

Sobre las manifestaciones termales de Pathé, vocablo *hñähñu* (otomí) que significa agua caliente —o termal—, Joseph Burkart se explayó en valiosas descripciones geológicas-mineralógicas (Mendoza, 1875):

> *El arroyo que viene de San Juan del Río, del lado Suroeste, y dirigiéndose al Noroeste, se ha cavado un lecho algo profundo, será apenas de unas 150 a 200 varas, en un pórfido alterado.*
>
> *El pórfido es de un gris oscuro y encierra cristales de feldspato hojoso, núcleos y cordones o cintitas de granate pardo.*
>
> *Las fuentes termales de Pathé (agua caliente en otomí) brotan del pórfido y al través del mencionado conglomerado. Estas aguas están brotando con gran ruido y cuando se tapan las aberturas naturales de donde están saliendo, con una piedra, entonces el agua sale haciendo borbollones. Las aberturas son de alguna consideración, puesto que algunas de ellas tienen de uno a dos pies de diámetro. El agua que está brotando de ellas es considerable.*
>
> *Los vapores de esta agua se elevan en la atmósfera, y son visibles a gran distancia, especialmente por la mañana y por la tarde. El agua que está brotando allí es extraordinariamente transparente y de*

> *una alta temperatura, próximamente de 96º centígrados, mientras que la temperatura del aire era al tiempo de la observación de 23º. A las nueve de la mañana la columna barométrica era de 24,908 pulgadas inglesas.*
>
> *En el valle, conté 9 diversos manantiales, poco distantes entre sí: 7 a la derecha y 2 a la izquierda. Todos ellos brotan en una línea de Oriente a Poniente, y se dirigen paralelamente a la línea principal de los volcanes de México. Sobre las rocas que cubren estas aguas, van dejando un residuo de sulfato de fierro.*
>
> *Subiendo un poco más hacia el valle adyacente de Pathé, el pórfido ya descrito, se cambia por una capa de un espesor de 6 a 12 pulgadas de una pizarra blanca, espática, en la cual se encuentra la calcedonia lechosa […] El pórfido es colorido, poco más que el anterior, y a veces es de un gris rojizo, y se hiende en las tablas delgadas y paralelas a la estratificación. En esas capas pórfidos-espáticas apizarradas, suele atravesar el azufre nativo, que en otro tiempo fue explotado. La mina estaba abandonada, el camino intransitable y por esta razón no pude adquirir más datos sobre ella.*

Una extensa área situada al norte de la ZGP, correspondiente a sector central del estado de Querétaro, fue investigada a mucho detalle por el Ing. Mariano Bárcena (1842-1899), quien se desempeñó como «director sustituto de la práctica de Mineralogía y Geología de los alumnos de la Escuela de Ingenieros». De dicha expedición, realizada en el año 1872, publicó un extenso informe (Bárcena, 1873), en el que se mencionan las aguas termales, así como los depósitos de alteración de la ZGP:

> *Además de las rocas eruptivas mencionadas, tuvimos ocasión de observar otras del mismo origen (p. 215), como son la perlita y la piedra pez. En el camino de Tequisquiapam a San Juan del Río se ven grandes bancos de la primera, provista de numerosas y pequeñas concreciones de la misma sustancia. En esta formación existen algunos manantiales termales muy alcalinos, cuya temperatura média es de 31°C.*

Tres décadas más tarde, la ZGP atrajo la atención del ingeniero José Guadalupe Aguilera (Fig. 4), quien describió tanto las rocas eruptivas como sus productos de alteración. Su mayor interés, sin embargo, no fueron las aguas termales sino los yacimientos de caolín de Yexthó, situados a un kilómetro al suroeste de las manifestaciones de Pathé. Aguilera analizó la potencialidad y estado de explotación de las minas de caolín, con base en descripciones detalladas y en su relación con las rocas volcánicas de la región y con los manantiales termales. Entre sus conclusiones, el autor menciona que los numerosos manantiales de la localidad debían su temperatura a los «macizos volcánicos, relativamente recientes, que se encuentran en su periodo de enfriamiento», asignando la actividad volcánica al Plioceno (Aguilera, 1907).

Figura 4. Retrato del ingeniero José Guadalupe Aguilera Serrano (1857-1941), quien fuera director del *Instituto Geológico de México*, además de fundador y primer presidente de la *Sociedad Geológica Mexicana*, *ca.* 1906. Archivo Histórico del Instituto de Geología, UNAM.

Además de describir la estructura y composición mineralógica de las vetas de caolín, Aguilera (1907) se refirió a las minas a cielo abierto, enumerándolas (Mothó, Santa Rosa, El Có y La Salitrera) y calificando los trabajos mineros de «muy superficiales y desordenados», pero asegurando la existencia de reservas de caolín suficientes para sostener su explotación por varios años. Para principios de los años 1950 estos criaderos estaban casi agotados (Instituto Nacional para la Investigación de Recursos Minerales, 1952).

Aguilera (1907) destacó la aplicación que se le podía dar al caolín para la fabricación de porcelana, con base en los análisis realizados en el Laboratorio Químico del IGN para conocer las concentraciones de los elementos mayores «cal, potasa, sosa, fierro, magnesia» que intervenían en sus propiedades mecánicas y su coloración. A partir de sus observaciones de campo y resultados de laboratorio, Aguilera (1907) auguró el éxito en la explotación del caolín dada la cercanía de la localidad a Ciudad de México y a las vías de ferrocarril que acortaban distancias. Para esa fecha eran de sobra conocidas las diversas aplicaciones del caolín para producir objetos de uso doméstico y ornato, loza, ladrillos y tejas. Existían fábricas de loza en Salamanca, Guanajuato, la de Niño Perdido en Ciudad de México, y en Chignahuapan, Puebla (Arriaga, 1873). En su disertación, Aguilera (1907) describió el mineral no metálico:

> *De colores blanco y rosado el más puro, y amarillento el de menor calidad. El kaolín de mejor calidad viene en pequeñas bolsas dentro de las zonas de kaolín y se distingue del menos puro además de su color, que hemos dicho que es blanco rosado, por ser más blando y ligeramente untuoso, caracteres que facilitan su separación o pepena en la mina a los trabajadores.*

Por su relevancia y calidad, el estudio realizado por Aguilera (1907) fue transcrito por el ingeniero Jenaro González Reyna en su libro «Riqueza Minera y Yacimientos Minerales de México», publicado en 1944 por el Banco de México y reeditado en 1956 como parte de los trabajos del XX Congreso Geológico Internacional celebrado en México.

DESCRIPCIÓN GENERAL DEL ÁREA DE ESTUDIO

La ZGP se localiza en el límite entre los estados de Hidalgo y Querétaro (centro de México), en el trecho limítrofe interestatal que sigue el cauce del Río San Juan, el cual es un tributario de la cuenca del Pánuco que aguas abajo de esta zona toma el nombre de Río Moctezuma (Fig. 1). Tanto las manifestaciones termales (antiguo pozo geotérmico y actual balneario) como las alteraciones hidrotermales de mayor extensión (incluyendo los depósitos de caolín) se hallan en el lado hidalguense (sur) de la frontera interestatal, dentro del municipio de Tecozautla.

1. CONTEXTO GEOLÓGICO REGIONAL

Geológicamente la ZGP se encuentra en el sector central de la Faja Volcánica Transmexicana. A nivel regional se distingue una secuencia volcánica continental de más de 1000 m de espesor, de edad Mioceno y Plioceno, que cubre discordantemente un basamento sedimentario marino del Cretácico (SGM, 2007). Este último no está expuesto en la ZGP; los afloramientos más cercanos se encuentran aproximadamente a 15 km hacia el N y el E, y corresponden a las formaciones El Doctor (carbonatos de plataforma) y Soyatal (lutitas y margas) (Wilson *et al.*, 1955; Carrillo Martínez, 2000).

La cubierta volcánica consiste esencialmente en tobas y lavas de composición riolítica, andesítica y basáltica (Nichols, 1970), y presenta una configuración en bloques limitados por fallas normales escalonadas que controlan los grandes rasgos del relieve. Las fallas se agrupan en dos sistemas: E-W y N-S (Carrillo Martínez, 1998 y 2000); al primero se asocia el semigraben de Aljibes (Suter *et al.*, 1995) y al segundo el graben de San Francisco (Carrillo Martínez *op.cit.*) —o de Pathé (Hiriart Le Bert, 2011).

Para identificar los enjambres de fallas y lineamientos predominantes en la región, se han procesado para el presente estudio varias imágenes satelitales Landsat 8 y QuickBird mediante el *software* ENVI 5.3. Los lineamientos se han extraído con un filtro de dirección y se han revisado usando imágenes sombreadas; finalmente, se han cotejado uno por uno con los rasgos geomorfológicos y la geología superficial, usando diferentes capas en un sistema de información geográfica ArcGis. El mapa así generado (Fig. 1B) muestra el control estructural del cauce del Río San Juan, el cual sigue el trazado de la Falla Moctezuma; se observa asimismo que la ZGP se ubica en la intersección de los dos sistemas de fallas predominantes (E-W y N-S).

2. SISTEMA GEOTÉRMICO

Las temperaturas del reservorio geotérmico en el antiguo pozo productor de vapor 'Pathé 1' (coordenadas: 20°34'40.2"N, 99°41'34.4"W) fueron calculadas en 191 °C y en 221 °C con el geotermómetro de cationes Na/K y el de gases H_2/Ar, respectivamente (Hiriart Le Bert, 2011). Las temperaturas medidas directamente en varios pozos exploratorios perforados en la zona por la CFE rondaron los 150 °C a 300 m de profundidad (Hiriart Le Bert, 2011).

Del pozo 'Pathé 1' fluye todavía hoy agua del tipo sódico-clorurado a 95 °C, mientras que en las manifestaciones naturales adyacentes a la ZGP el agua es sódica-bicarbonatada y las temperaturas no superan los 40 °C (Hiriart Le Bert, 2011); como ejemplo de estas últimas están los manantiales de Taxidhó (topónimo *hñähñu* que significa 'piedra blanca'), situados 4.5 km hacia el NE de la zona de estudio (coordenadas: 20°36'7.2"N, 99°39'15.7"W), sobre el trazado de la Falla Moctezuma ('Falla E' en Carrillo Martínez, 1998), al fondo del cañón por el que discurre el Río San Juan (Fig. 1).

En la ZGP son conspicuas las alteraciones hidrotermales superficiales, desarrolladas a lo largo de fallas (Carrillo Martínez, 1998 y 2000), especialmente en las intersecciones de fallas (Fig. 5). Incluyen los depósitos de caolín de Yexthó, objeto de investigación de Aguilera (1907).

De acuerdo con Hiriart Le Bert (2011), el potencial del sistema geotérmico es de 33 MW (desviación estándar = 17 MW), estimado con el método volumétrico-Montecarlo, o de hasta 49 MW con el método de descompresión gradual.

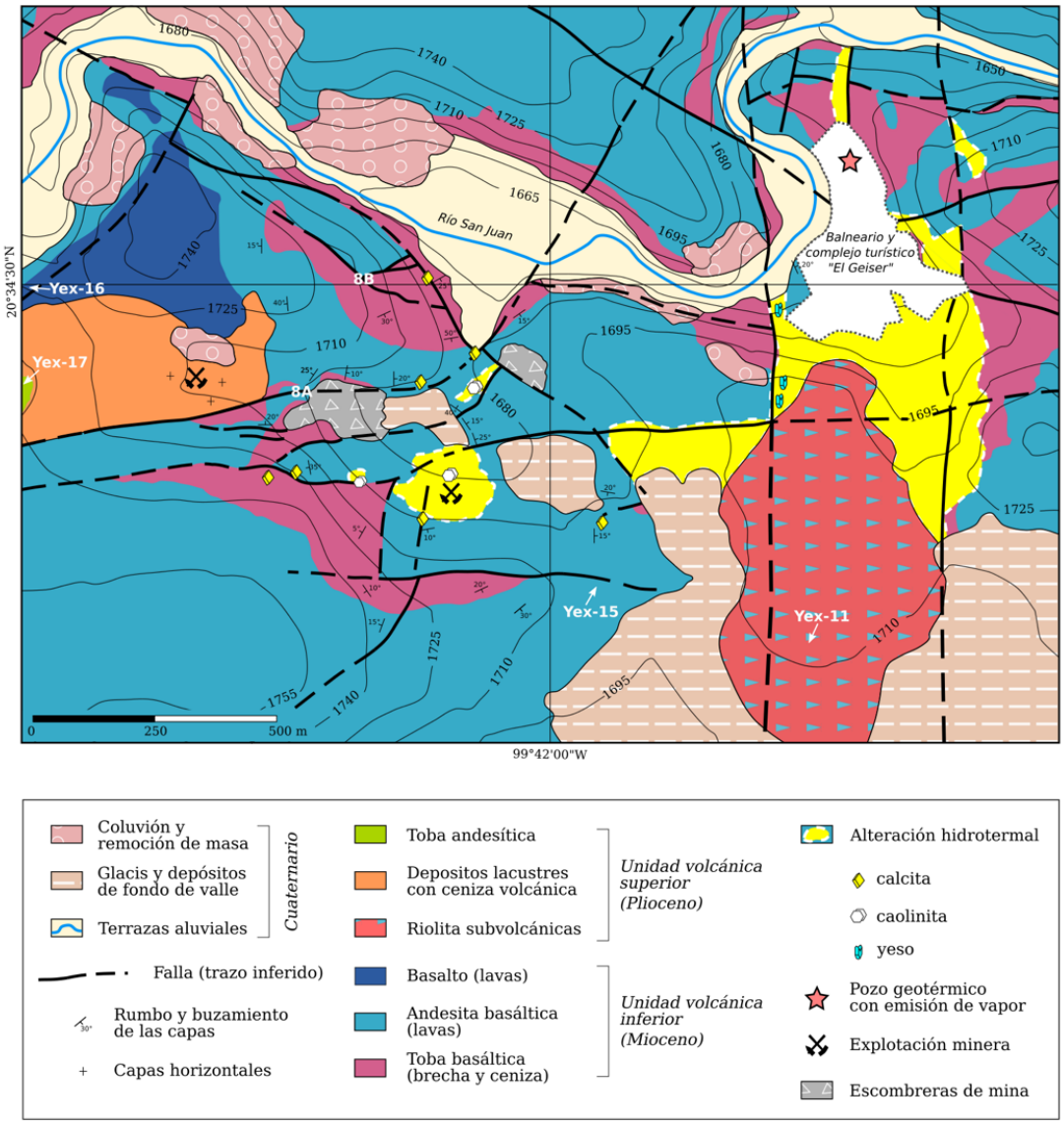

Figura 5. Mapa geológico detallado de la zona geotérmica de Pathé (fuente: elaboración propia, a partir de levantamientos de campo apoyados por imágenes satelitales), que incluye la distribución de las alteraciones hidrotermales y sus minerales más característicos, así como la ubicación de las manifestaciones termales (actual «Balneario El Géiser») y de los depósitos de caolín (antiguas minas de Yexthó).

8A y 8B: ubicaciones de las fallas mostradas en la Fig. 8.

Yex-11, Yex-15, Yex-16 y Yex-17: ubicaciones de las muestras analizadas (resultados en Tabla 1 y Fig. 7).

Estudio geológico local

A pesar del modesto rango hipsométrico, con cotas entre 1645 y 1760 m s.n.m. (en el lecho del Río San Juan y en las mesetas más elevadas, respectivamente; Fig. 1A), la orografía que enmarca la ZGP es intrincada, caracterizándose por un relieve montuoso de naturaleza volcánica disecado por barrancas (Fig. 2A), cuyo trazado está controlado por los sistemas de fallas que concurren en el área (*cf.* Carrillo Martínez, 1998). Las fallas, además de modelar el patrón de la red de drenaje hídrico (Fig. 1), tienen como expresión morfológica común los escarpes —originales o derivados (afectados por la erosión)—, con desniveles de hasta 30 m (Fig. 3); este valor en la vertical coincide con el desplazamiento medido por Carrillo Martínez (1998) en muchas de las fallas de la zona, aunque para algunas del sistema N-S reporta saltos de hasta 70 m.

1. Unidades litológicas y estructurales

Con la excepción de los depósitos del Cuaternario —que ocupan el lecho y las orillas del Río San Juan (terrazas aluviales), los terrenos llanos (glacis y depósito de fondo de valle) y el pie de las laderas (coluvión y depósitos de remoción de masa)—, todas las rocas que afloran en la ZGP pertenecen a unidades volcánicas del Neógeno (Figs. 5 y 6). Para una mayor certeza en la clasificación de dichas unidades, se ha realizado el análisis químico de cuatro muestras de roca por medio del método de espectroscopia de emisión óptica por plasma de acoplamiento inductivo (ICP-OES, por su sigla en inglés) en el laboratorio ActLabs, Ancaster, Canadá. Los resultados se presentan en la Tabla 1 y se proyectan en el diagrama de clasificación química de rocas mostrado en la figura 7.

Tabla 1. Composición química (análisis de roca total por ICP-OES) de muestras representativas de las unidades volcánicas de la zona geotérmica de Pathé (clasificación y descripción de las muestras en Fig. 7).

#	muestra	SiO_2 (% en peso)	Al_2O_3	Fe_2O_3 (T)	MnO	MgO	CaO	Na_2O	K_2O	TiO_2	P_2O_5	*LOI**	total
1	*Yex-11*	80.97	6.66	1.35	0.01	0.50	1.02	0.12	4.78	0.24	0.12	4.02	99.80
2	*Yex-15*	52.73	17.65	7.91	0.13	4.57	8.83	3.21	1.00	1.20	0.23	3.38	100.80
3	*Yex-16*	50.99	17.67	9.84	0.15	3.58	8.49	3.75	0.62	2.05	0.41	3.12	100.70
4	*Yex-17*	60.20	14.41	5.29	0.09	2.03	2.98	3.51	3.21	0.75	0.22	7.81	100.50

#	Ba (ppm)	Sr	Y	Sc	Zr	Be	V
1	518	160	22	5	196	3	11
2	285	485	21	26	161	1	171
3	438	591	33	24	296	1	174
4	476	536	29	11	303	2	52

**LOI* = pérdida por ignición (por su sigla en inglés)
Coordenadas: **#1**: 20°34'01.1"N / 99°41'43.3"W; **#2**: 20°34'03.5"N / 99°42'04.8"W; **#3**: 20°34'28.1"N / 99°42'47.0"W; **#4**: 20°34'21.4"N / 99°42'45.4"W

En la ZGP se distinguen dos unidades volcánicas, que en el presente trabajo denominaremos (*a*) Unidad volcánica inferior, de composición básica, y (*b*) Unidad volcánica superior, de composición intermedia a ácida (Figs. 6 y 7). Cabe mencionar que las perforaciones realizadas con fines exploratorios (hasta una profundad de 1286 m) revelaron una sucesión riolítica de lavas, tobas y brechas (Carrillo-Martínez, 2000), la cual no aflora en la ZGP por estar cubierta por la Unidad volcánica inferior.

La Unidad volcánica inferior es la que ocupa una mayor extensión de la ZGP y su espesor expuesto es de hasta 70 m. Se corresponde con la 'unidad basáltica' a la que Nichols (1970) atribuyó una edad Mioceno superior; de acuerdo con Suter *et al.* (1995), esta unidad equivaldría al Grupo San Juan (definido por Wilson *et al.*, 1955). Hacia la base, la Unidad volcánica inferior presenta depósitos piroclásticos (tefra) no consolidados, de tamaños ceniza y lapilli predominantes, con bloques dispersos de hasta 40 cm de diámetro. Estos depósitos, que se corresponden con la 'toba basáltica' definida por Nichols (1970), tienen un espesor máximo de ~25 m, muestran laminación, y presentan —a escala de afloramiento— cambios bruscos de coloración, de amarillo a rojizo (Fig. 6A). Por encima de ellos yace un paquete de lavas de hasta 50 m de espesor. Las lavas comúnmente se encuentran brechificadas a la base, pero su modo de ocurrencia más característico es como lavas lajeadas, aspecto que ya había sido percibido por Joseph Burkart y descrito como 'apizarrado' (en: Mendoza, 1875). Las lavas con esta fisilidad característica presentan en muestra de mano una coloración gris y fenocristales de hasta 2 mm de plagioclasa y piroxeno (Fig. 6B). Químicamente son andesitas basálitcas (Fig. 7). Hacia el techo de la unidad, las lavas son diferentes en cuanto a textura y composición: son más obscuras y marcadamente vesiculares (Fig. 6C), con una composición química distintiva de los basaltos (Fig. 7).

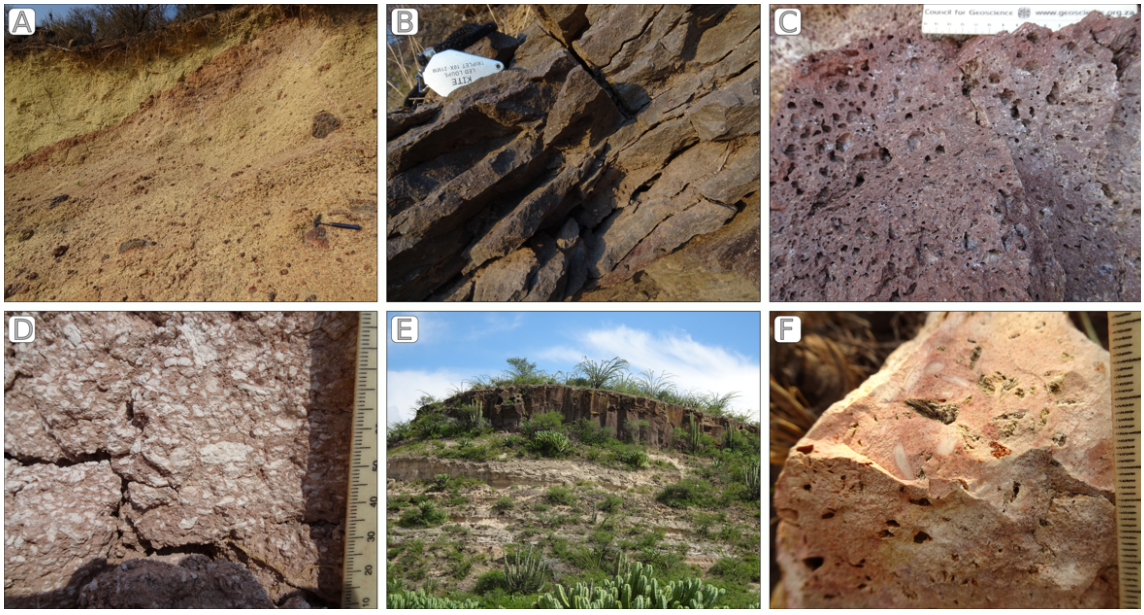

Figura 6. Fotografías de campo de las unidades volcánicas de la zona geotérmica de Pathé. Unidad volcánica inferior (Mioceno superior): (A) Depósitos piroclásticos ('toba basáltica'; Nichols, 1970), con lapilli predominante y bloques dispersos; (B) andesita basáltica sin alteración de la unidad volcánica inferior, con peculiar fisilidad que le confiere un aspecto lajeado característico; y (C) basalto vesicular. Unidad volcánica superior (Plioceno): (D) Toba pumítica; y (E) toba Don Guiñó, culminando la secuencia volcánica. (F) Riolita ('intrusión subvolcánica félsica'; Suter *et al.*, 1995), con porosidad secundaria (fantasmas) debida a la disolución cuasi total de los fenocristales.

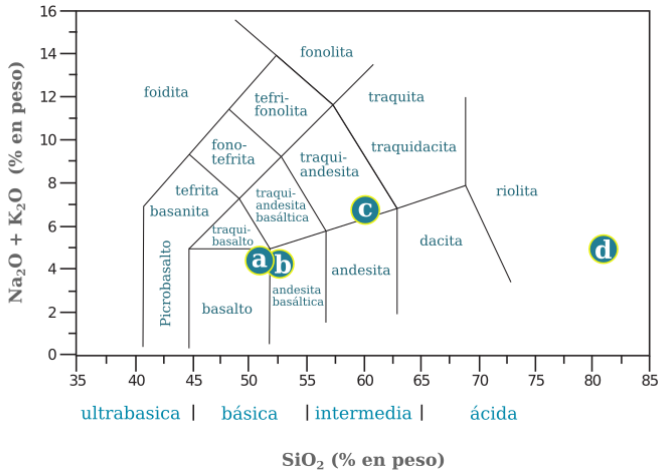

Figura 7. Clasificación química de muestras representativas de las unidades volcánicas de la zona geotérmica de Pathé (análisis y coordenadas disponibles en la Tabla 1), mediante diagrama TAS (del inglés '*total-alkali silica*'; Le Bas, 1986): (a) Basalto: lava vesicular de la Unidad volcánica inferior, Mioceno superior (muestra 'Yex-16' en Tabla 1); (b) Andesita basáltica: lava lajeada de la Unidad volcánica inferior, Mioceno superior (muestra 'Yex-15' en Tabla 1); (c) Andesita (traquiandesita): toba Don Guiñó de la Unidad volcánica superior, Plioceno (muestra 'Yex-17' en Tabla 1); (d) Riolita alta en sílice de la 'intrusión subvolcánica félsica' (Suter *et al.*, 1995) (muestra 'Yex-11' en Tabla 1).

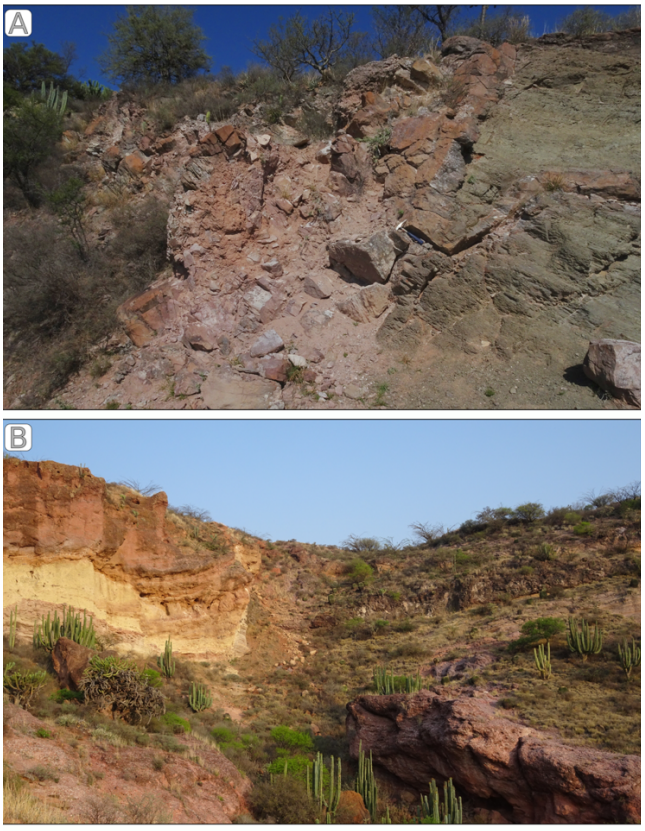

Figura 8. Fallas en la zona geotérmica de Pathé: (A) Brecha tectónica en una falla de dirección E-W que corta a las lavas (andesita basáltica) de la Unidad volcánica inferior (Mioceno superior) (coordenadas: 20°34'20.2"N, 99°42'22.1"W); (B) falla E-W que pone en contacto los depósitos piroclásticos (izquierda) con las lavas de composición andesítica-basáltica que los sobreyacen (derecha), ambos de la Unidad volcánica inferior (Mioceno superior) (coordenadas: 20°34'27.5"N, 99°42'15.7"W). La ubicación de ambas fotos se muestra en la Fig. 5.

La Unidad volcánica superior, de composición más silícica, aflora únicamente en algunas zonas elevadas de la ZGP, con espesores no mayores a 30 m (Fig. 6E). Consiste en una sucesión de dos unidades de edad Plioceno; de base a techo: (i) 'toba pumítica', depositada en un ambiente lacustre (Nichols ,1970) y que se correlaciona, según Carrillo-Martínez (2000), con la Formación Tarango (Segerstrom, 1962), y (ii) 'Toba Don Guyño' (Segerstrom, 1962) —o Don Guiño—, de naturaleza félsica, atribuida a una erupción de la Caldera de Huichapan (Ferriz y Mahood, 1986; Aguirre-Díaz y López-Martínez, 2009).

La toba basal (pumítica) forma una capa que yace sobre la Unidad volcánica inferior, y consiste en fragmentos angulares de pómez, con buena clasificación (diámetro de partículas entre 3 y 10 mm), en una matriz limosa de coloración rojiza, no superior al 30% modal (Fig. 6D). Dicho depósito no está consolidado y ha sido objeto de explotación intermitente en unos bancos de material situados 500 m al oeste de las minas de caolín (Fig. 5), donde tiene un espesor no mayor a 5 m. Esta capa presenta granoclasificación positiva e incrementa hacia el techo su proporción de matriz limosa. De esta manera, da lugar gradualmente a una capa de limo y arena, con bloques basálticos dispersos hacia la base y una marcada laminación en sus partes media y superior. Contiene restos fosilizados de plantas (posiblemente tallos y raíces) y algunos horizontes con laminaciones onduladas que podrían corresponder a sismitas.

Sobreyaciendo los depósitos vulcanosedimentarios antes descritos y, por lo tanto, culminando las unidades volcánicas de la ZGP, se encuentra la toba Don Guiño (Fig. 6E). En esta zona, dicha toba aparece únicamente en afloramientos relictos, de escasa extensión y con un espesor no mayor a 4 m, representando un emplazamiento muy distal respecto a la Caldera de Huichapan de la que se originó, donde alcanza espesores de más de 100 m y tiene importancia económica como roca dimensionable (SGM, 2012). A diferencia de las capas vulcanosedimentarias, la toba Don Guiño está consolidada y presenta mala clasificación granulométrica, con clastos de hasta 5 cm entre los que se halla obsidiana. El resultado de un análisis químico en roca total indica que su composición es entre andesítica y traquiandesítica (Fig. 7).

Inmediatamente al sur de las manifestaciones termales, se encuentra un afloramiento de ~0.2 km^2 de rocas de composición silícica, a modo de meseta (~1700-1715 m s.n.m.) (Figs. 5 y 6F), que corresponde a la unidad mencionada en Suter *et al.* (1995) como 'intrusión subvolcánica félsica'. Las rocas que la componen presentan un aspecto en afloramiento y muestra de mano marcadamente distinto al de las de las unidades volcánicas antes descritas. De gran dureza y coloración clara (blanco, beige y rosado), son masivas y microcristalinas, enteramente silícicas de acuerdo a su apariencia macroscópica (no se observa ninguna fase mineral aparte de la matriz cuarzosa), y tienen porosidad macroscópica posiblemente secundaria (Fig. 6F). Localmente presentan pseudoestratificación, aunque mucho más burda que el lajeado de las lavas de la unidad volcánica inferior. Químicamente es extremadamente rica en sílice (80.97 % en peso; Tabla 1), composición que es compatible con la de una riolita alta en sílice (Fig. 7); esta composición aunada a las relaciones de corte con el resto de unidades nos sugiere una afinidad genética y cronológica con la Unidad volcánica superior, aunque no podemos descartar que sea el producto de una silicificación hidrotermal.

Desde un punto de vista morfoestructural, la ZGP está conformada como un arreglo de bloques de la Unidad volcánica inferior basculados entre 10° y 30° hacia el S y el W, limitados por fallas con direcciones predominantes E-W, N-S y NW-SE (Figs. 5 y 8). Las tobas basales de la Unidad volcánica superior yacen en inconformidad sobre la Unidad volcánica inferior, con las capas en

disposición horizontal o cuasi horizontal (Fig. 6E). Únicamente las fallas del sistema E-W parecen afectar a la Unidad volcánica superior (incluido el cuerpo subvolcánico félsico; Fig. 5).

2. Alteración hidrotermal

La ZGP desarrolla una notoria alteración hidrotermal superficial, aunque en afloramientos discontinuos, los cuales en conjunto suman una extensión de ~0.5 km² (Figs. 5 y 9). Esta alteración fue estudiada por Aguilera (1907), quien describió en detalle su composición mineral, texturas y modo de ocurrencia. La interpretación de esta información de campo le permitió formar una hipótesis del origen hidrotermal de la alteración —incluido el caolín—, atribuyendo su génesis a la circulación de 'agua caliente' a través de fracturas y zona porosas de las rocas.

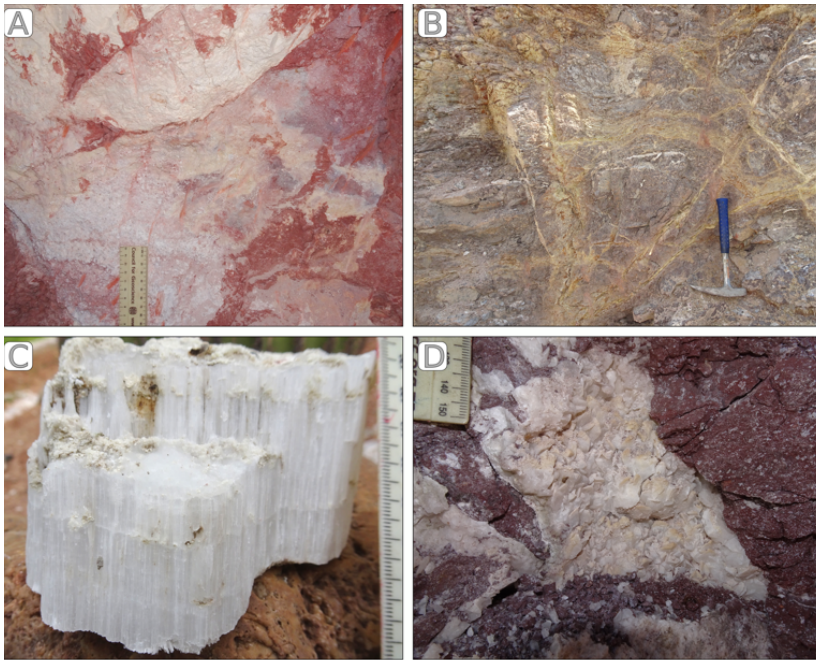

Figura 9. Fotografías de campo de los productos de la alteración hidrotermal en la zona geotérmica de Pathé: (A) Caolín de las antiguas minas de Yexthó, formado por la alteración *pervasiva* de los depósitos piroclásticos de la Unidad volcánica inferior (Mioceno superior); (B) Alteración selectiva en *stockwork* de vetillas de yeso de lavas de la Unidad volcánica inferior (Mioceno superior); (C) espécimen de yeso fibroso de origen hidrotermal recolectado en el trazado de la Falla de Pathé (N-S), en las inmediaciones de las manifestaciones geotérmicas; (D) veta de calcita «hojosa» en una brecha del techo de los depósitos piroclásticos de la Unidad volcánica inferior (Mioceno superior).

De acuerdo con su geometría y distribución en la superficie, la alteración en la ZGP está controlada por fallas (Fig. 5), y se desarrolla predominantemente a expensas de los depósitos piroclásticos de la Unidad volcánica inferior y, más escasamente, en las lavas de la misma unidad. Los depósitos de caolín de Yexthó (Figs. 2B y 9A), de al menos 10 m de espesor, se hallan sobre el trazado de fallas E-W (Fig. 5). Desarrollan una textura masiva y criptocristalina, producto de una alteración *pervasiva* de las cenizas volcánicas (Fig. 9A), aunque localmente preservan texturas relictas de la tefra. Asociado al caolín, en cantidades subordinadas, hay ópalo de aspecto lechoso y textura botroidal. En su parte superior, el depósito de caolín termina de manera abrupta, dando lugar a las lavas andesítico-basálticas. El espectro de reflexión en el infrarrojo de onda corta (λ: 1300–2500 nm) del caolín de Yexthó, obtenido con un equipo LabSpec Pro Spectrophotometer

(Analytical Spec-tral Devices, Inc.) en el Instituto de Geofísica de la UNAM, muestra únicamente —y muy claramente— los rasgos de absorción característicos de la caolinita, $Al_2Si_2O_5(OH)_4$ (USGS Spectroscopy Lab de Clark *et al.*, 2007), revelando la gran pureza del depósito (Fig. 10).

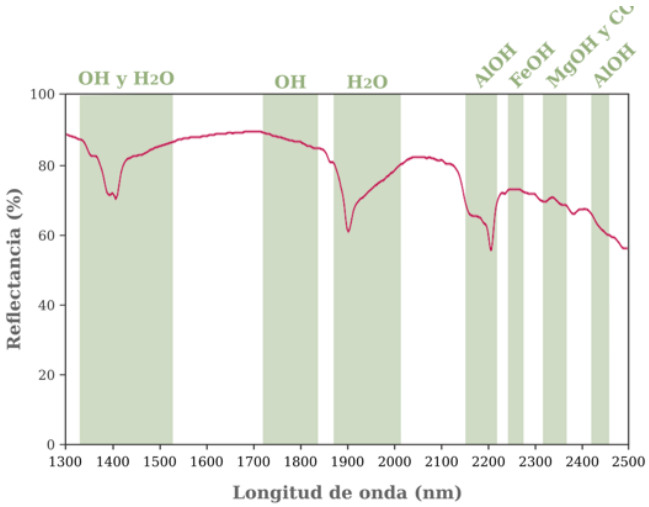

Figura 10. Espectro de reflectancia en el infrarrojo de onda corta (λ: 1300–2500 nm), representativo de los depósitos de caolín de Yexthó (coordenadas: 20°34'13.7"N, 99°42'08.9"W). Los rasgos de absorción revelan que la muestra analizada está compuesta por caolinita $Al_2Si_2O_5(OH)_4$ de gran pureza. Las bandas de absorción usadas para la identificación mineral (barras verticales) se obtuvieron de Spectral International Inc. (1994).

Por otro lado, la alteración asociada a las fallas N-S es muy distinta en composición y modo de ocurrencia: los minerales predominantes son la calcita y el yeso, emplazados en vetillas de algunos mm hasta 25 cm de espesor. Las vetas están encajonadas en la Unidad volcánica inferior, tanto en los depósitos piroclásticos como en las lavas, y su orientación predominante es N-S (Fig. 11). Localmente forman *stockworks* (Fig. 9B) y pueden presentar brechamiento hidráulico. La calcita desarrolla una textura hojosa, con cristales tabulares de hasta 1 cm (Fig. 9D), mientras que el yeso se presenta en agregados de cristales de hábito fibroso, de hasta 5 cm de longitud (Fig. 9C).

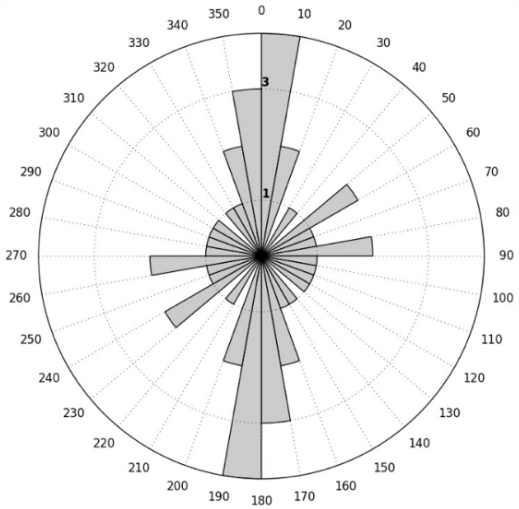

Figura 11. Diagrama de rosa de los vientos (n = 24 mediciones) que muestra las orientaciones predominantes de vetillas de calcita de la zona geotérmica de Pathé.

DISCUSIÓN Y CONCLUSIONES

1. RELEVANCIA HISTÓRICA Y PATRIMONIAL

Durante los siglos XVIII y XIX la ZGP recibió la visita de distinguidos exploradores y científicos, cuyo objetivo era recorrer el territorio mexicano y describir sus recursos naturales. Sin embargo, esas visitas de hecho tenían como destino el Real de Minas de Zimapán, renombrado por su extraordinaria riqueza argentífera desde el periodo colonial temprano (Suter, 2016). Pero la cercanía de éste (situado ~35 km hacia el NE) a la ZGP, aunada a la fama que por aquel entonces tenían las manifestaciones termales de Pathé, debió persuadir a los exploradores a acercarse hasta dicha zona, en ese entonces remota.

Entrando al siglo XIX, la ZGP se convirtió en objeto de interés por sí misma, primero por sus recursos minerales (Aguilera, 1907) y, a mediados de siglo, como fuente de energía (*cf.* Hiriart Le Bert, 2011). Si bien la producción eléctrica fue baja (3.5 MW de capacidad instalada) y duró apenas 13 años (1959–1972), Pathé fue la primera planta geotermoeléctrica del continente americano, y forjó capacidades técnicas que le permitieron a México desarrollar otros campos más productivos y alcanzar en 2016 la cuarta posición a nivel mundial en capacidad geotermoeléctrica instalada (CeMIEGeo, 2020). Además, dada la necesidad de una transición energética global hacia las fuentes renovables como una medida urgente para afrontar el desafío mundial del cambio climático (*e.g.* Solheim *et al.*, 2018), resulta inverosímil que la ZGP caiga en el olvido.

Al margen de cualquier consideración acerca de su memorable pasado histórico, su singular contexto geológico y la estética particular de su entorno natural, existe desde 1985 un complejo turístico en la ZGP, el cual es considerado por Toscana Aparicio (2017) como un éxito en términos del desarrollo económico de las comunidades. Sin embargo, las instalaciones no cuentan con ningún elemento de interpretación geoturística (*i.e.* paneles informativos sobre la energía geotérmica o sobre el valor histórico y geológico del sitio) que sensibilice e informe al visitante o que promueva la educación. El estudio y eventual restauración de los testimonios que aún quedan de la antigua planta eléctrica deberían hacerse siguiendo los preceptos de la arqueología industrial, en aras de garantizar su conservación para las futuras generaciones. De la misma manera, deberían preservarse los afloramientos rocosos que en el pasado encajonaron las manifestaciones termales.

2. CONDICIONANTES GEOLÓGICOS Y MODELO DEL SISTEMA HIDROTERMAL

Las manifestaciones termales de la ZGP se ubican en una zona de intersección de dos sistemas regionales de fallas, con direcciones N-S y E-W; asimismo, la distribución de las alteraciones está controlada por fallas pertenecientes a dichos sistemas (Fig. 5). Esta característica, junto con la ausencia de vulcanismo reciente (Cuaternario) cerca del área de estudio, permite interpretar la ZGP como un sistema geotérmico convectivo controlado por fallas ('*non-magmatic, extensional domain type*' según la clasificación de Moeck, 2014). Dentro de esta tipología se incluyen numerosos ejemplos de la Faja Volcánica Transmexicana (*e.g.* Cruz Pérez *et al.*, 2018; Canet *et al.*, 2019; Pérez-Martínez *et al.*, 2020). En este tipo de sistemas geotérmicos la energía es transportada hacia la superficie mediante fluidos que ascienden a través de fallas normales, en ausencia de una fuente magmática de calor; el desplazamiento vertical relativo provocado por las fallas es lo que ocasiona que las alteraciones queden expuestas (*e.g.* Faulds y Hinz, 2009).

En la ZGP, las fallas del sistema N-S afectan exclusivamente a la Unidad volcánica inferior, del Mioceno Superior (Nichols, 1970), la cual se presenta segmentada en bloques basculados. Por otro lado la Unidad volcánica superior, del Plioceno (Nichols, 1970), aparece afectada únicamente por las fallas del sistema E-W, lo cual se percibe a nivel regional, ya que localmente las tobas que la componen se disponen horizontalmente y sin evidencia de deformación (Fig. 5). Podemos considerar, por lo tanto, que las fallas N-S son en términos generales más antiguas que las E-W. Asociada a las fallas N-S ocurre la asociación de alteración calcita-yeso, que involucra fluidos ricos en sulfato, oxidados y alcalinos. Para establecer el origen del azufre sería necesario conocer su composición isotópica en el yeso; en tanto no se cuenta con dicha información no se puede descartar una posible removilización hidrotermal desde series evaporíticas del basamento Mesozoico.

La formación de caolinita, claramente ligada a las fallas E-W —y por lo tanto más tardía—, es índice de una alteración argílica avanzada (*e.g.* Thompson y Thompson, 1996). Este tipo de alteración es característico de zonas de condensación de vapor en sistemas geotérmicos (*e.g.* González-Partida *et al.*, 2005), de tal modo que ocurre por encima del nivel freático debido a la disolución y oxidación del H_2S, el cual condensa como resultado de la interacción entre el vapor y el acuífero; las condiciones del fluido son un pH muy ácido (2–3) y temperaturas cercanas a los 100 °C (Thompson y Thompson, 1996).

La sucesión de los eventos de alteración, asignables a sendos sistemas de fallas, sugiere que la actividad de la ZGP inició desde antes del Plioceno, tratándose, por lo tanto, de una actividad hidrotermal longeva.

AGRADECIMIENTOS

Nuestro mayor reconocimiento y gratitud a las personas e instituciones mexicanas cuya labor pionera sentó las bases de las investigaciones geológicas actuales, en particular aquellas cuyos trabajos son citados en este artículo. Agradecemos a Xavier M. Canet Franco y a Meritxell Canet Franco por su apoyo incondicional durante el trabajo de campo. Igualmente expresamos nuestro agradecimiento a Michael Vázquez Gómez y Augusto A. Rodríguez Díaz por los análisis mediante espectroscopia de reflexión de las alteraciones hidrotermales, a Iván Gustavo Vallejo Castillo por el modelo digital de elevaciones, al profesor Gregorio Jaén Gaspar por la revisión y traducción de los topónimos de origen *hñähñú*, al M. en C. Miguel Á. Cruz Pérez por las discusiones en campo, y al Lic. Saúl Armendáriz Sánchez por el apoyo documental. Este trabajo se ha beneficiado de las valiosas revisiones realizadas por el Dr. Max Suter, el Dr. Arturo Iglesias y un revisor anónimo, así como del apoyo editorial del Dr. Servando De la Cruz-Reyna y de la Mtra. Andrea Rostan Robledo.

REFERENCIAS

Aguilera, J.G., 1905, Reseña del Desarrollo de la Geología en México: Boletín de la Sociedad Geológica Mexicana, 1, 35–117.

Aguilera, J.G., 1907, Los Caolines de la Hacienda de Yexthó: Boletín de la Sociedad Geológica Mexicana, 3, 25–33.

Aguirre-Díaz, G.J., López-Martínez, M., 2009, Geologic evolution of the Donguinyó-Huichapan caldera complex, central Mexican Volcanic Belt, Mexico: Journal of Volcanology and Geothermal Research, 179 (1–2), 133–148.

Arriaga, J.J., 1873, La Exposición Municipal. Artículo V. Productos cerámicos: El Minero Mexicano, tomo I, núm. 37, 4.

Bárcena, M. 1873, Memoria presentada al Sr. Blas Balcárcel, Director de la Escuela Especial de Ingenieros, por Mariano Bárcena, Director sustituto de la práctica de Mineralogía y Geología en el año de 1872, Díaz Covarrubias, J., Memoria que el encargado de la Secretaría de Justicia e Instrucción Pública presenta al Congreso de la Unión en 15 de septiembre de 1873: México, Imprenta del Gobierno, en Palacio, 201-227.

Burkart, J., 1836, Aufenthalt und Reisen in Mexico in den Jahren 1825 bis 1834; Bemerkungen über Land, Produkte, Leben und Sitten der Einwohner und Beobachtungen aus dem Gebiete der Mineralogie, Geognosie, Bergbaukunde, Meteorologie, Geographie: Stuttgart, Verlag Schweizerbarth, 1, 392 p.; 2, 286 p.

Canet, C., Rodríguez-Díaz, A.A., Bernal, I.D., Pi, T., Sánchez-Córdova, M.M., Núñez-Useche, F., Villanueva-Estrada, R., Molina, G., Reich, M., Peláez, B., Jiménez Salgado, E., González-Partida, E., Sandoval Medina, F., Carrillo-Sánchez, C.B., 2019, Consideraciones sobre el sistema geotérmico de San Bartolomé de los Baños, Guanajuato (México), desde un análisis de la alteración hidrotermal y las inclusiones fluidas: Geofísica Internacional, 58-3, 229–246.

Carrillo Martínez, M., 1998, Normal faulting in the Pathé geothermal area, Central Mexico: Geofísica Internacional, 37, 103–111.

Carrillo-Martínez, M., 2000, Geología de la Hoja 14Q-e(7) Zimapán, Estados de Hidalgo y Querétaro: México, D.F., Universidad Nacional Autónoma de México, Instituto de Geología, Carta geológica de México, serie 1:100000, map explanations, 33 p.

Centro Mexicano de Innovación en Energía Geotérmica (CeMIEGeo), 2020, Geotermia en México, disponible en http://www.cemiegeo.org/index.php/geotermia-en-mexico, consultado el 3 de noviembre de 2020.

Clark R.N., Swayze G.A., Wise R.A., Livo K.E., Hoefen T.M., Kokaly R.F., Sutley S.J., 2007, USGS Digital Spectral Library splib06a, USGS Digital Data Series, 231, http://speclab.cr.usgs.gov, consultado el 3 de noviembre de 2020.

Cruz Pérez, M.A., Canet Miquel, C., Salgado Martínez, E., Morelos-Rodríguez, L., García Alonso, E., 2018, Geositios, en Canet Miquel C. (coord.), Guía de campo del Geoparque de la Comarca Minera, 1a edición, Instituto de Geofísica–Secretaría de Desarrollo Institucional, UNAM, 150–221.

Engstrand, I.H.W., 1981, Spanish scientists in the New World, The eighteenth-century expeditions: Seattle, Washington, University of Washington Press, 220 p.

Faulds J.E., Bouchot V., Moeck I., Oguz K., 2009, Structural controls of geothermal systems in Western Turkey: A preliminary report: GRC Transactions, 33, 375–383.

Ferriz, H., Mahood, G.A., 1986, Volcanismo riolítico en el eje neo volcánico mexicano: Geofísica Internacional, 25, 117–156.

Gómez Canedo, L., 1976, La Sierra Gorda a fines del siglo XVIII. Diario de un viaje de inspección a sus milicias: Historia Mexicana, 26 (1), 132-149.

González Claverán, V., 1988, La expedición científica de Malaspina en Nueva España 1789–1794: México, D.F., El Colegio de México, 528 p.

González-Partida E., Carrillo-Chávez A., Levresse G., Tello-Hinojosa E., Venegas-Salgado S., Ramirez-Silva G., Pal-Verma M., Tritlla J., Camprubi A., 2005, Hydrogeochemical and isotopic fluid evolution of the Los Azufres geothermal field, Central Mexico: Appl. Geochem., 20, 23–29.

González-Ruiz, L.E., González-Partida, E., Garduño Monroy, V.H., Martinez, L., Pironon, J., Díaz-Carreño, E.H., Yáñez-Dávila, D., Romero Rojas, W., Romero-Rojas, M.C., 2015, Distribución de Anomalías Geotérmicas en México: Una guía útil en la prospección geotérmica: Revista Internacional de Investigación e Innovación Tecnológica, nota técnica.

Hiriart Le Bert, G., 2011, Evaluación de la energía geotérmica en México: Informe para el Banco Interamericano de Desarrollo y la Comisión Reguladora de Energía, 164 p.

Instituto Nacional para la Investigación de Recursos Minerales, 1952, Memorias de la Primera Convención Interamericana de Recursos Minerales, México, Imprenta Moctezuma, 331 p.

Le Bas, M.J., Le Maitre, R.W., Streckeisen, A., Zanettin, B., 1986, A chemical classification of volcanic rocks based on the total alkali-silica diagram: Jourary of Petrology. 27, 745–750.

Mendoza, G., 1875, Notas sobre las fuentes termales de Pathé, traducidas de "Los Viajes en México del Dr. J. Burkart, por el señor socio": El Propagador Industrial, tomo I, núm. 32, 373.

Moeck, I.S., 2014, Catalog of geothermal play types based on geologic controls: Renewable and Sustainable Energy Reviews, 37, 867–882.

Morelos Rodríguez, L., 2012, La geología mexicana en el siglo XIX. Una revisión histórica de la obra de Antonio del Castillo, Santiago Ramírez y Mariano Bárcena, México: Secretaría de Cultura de Michoacán / Plaza y Valdés, 356 p.

Morelos Rodríguez, L., Moncada Maya, J.O., 2015, Orígenes y fundación del Instituto Geológico de México: Asclepio, 67, 103.

Nichols, C.R., 1970, The geology and geochemistry of the Pathé geothermal zone, Hidalgo, Mexico: Norman, Oklahoma, EUA, The University of Oklahoma, tesis doctoral 178 p.

Nieva, D., Prol-Ledesma, R.M., Romo-Jones, J.M., 2013, La geotermia en el futuro energético sustentable de México: Foro Internacional sobre Energía Geotérmica, *Conference paper*.

Ordaz Méndez, C.A., Flores Armenta, M., Ramírez Silva, G., 2011, Potencial geotérmico de la República Mexicana: Geotermia, 24, 50–58.

Pérez-Martínez, I., Villanueva-Estrada, R.E., Cardona-Benavides, A., Rodríguez-Díaz, A.A., Rodríguez-Salazar, M.T., Guadalupe, J., 2020, Hydrogeochemical reconnaissance of the Atotonilco el Alto-Santa Rita geothermal system in the northeastern Chapala graben in Mexico: Geothermics, 83, 101733.

Segerstrom, K., 1962, Geology of south-central Hidalgo and northeastern México: U.S. Geological Survey Bulletin, 1104-C, 87–162.

Servicio Geológico Mexicano (SGM), 2007, Tequisquiapan F14-C67, carta geológico-minera 1:50,000. SGM, Pachuca, Hidalgo, 1 mapa.

Servicio Geológico Mexicano (SGM), 2012, Inventario físico de los recursos minerales de la carta Huichapan F14-C78. SGM, Pachuca, Hidalgo.

Sociedad Geológica Mexicana (SGM), 1904, Asamblea General y Estatutos de la Sociedad Geológica Mexicana: Boletín de la Sociedad Geológica Mexicana, 1, 15–18.

Solheim, E., Espinosa, P., Stieglitz, N., 2018, Clean Energy Transition Needs to Accelerate: United Nations Framework Convention on Climate Change (UNFCCC), disponible en https://unfccc.int/news/clean-energy-transition-needs-to-accelerate, consultado el 3 de noviembre de 2020.

Spectral International Inc., 1994, SWIR spectral mineral identification system and spectral database SPECMINTM, vol. II. Integrated Spectronics, CO, USA.

Suter, M., Carrillo Martínez, M., López Martínez, M., Farrar, E., 1995, The Aljibes half-graben —Active extension at the boundary between the trans-Mexican volcanic belt and the Basin and Range Province, Mexico: Geological Society of America Bulletin, 107, 627–641.

Suter, M., 2016, Early 19th Century Geologic Studies of the Zimapán Region, Central Mexico: Boletín de la Sociedad Geológica Mexicana, 68, 215–230.

Thompson, A.J.B., Thompson, F.J.H., 1996, Atlas of Alteration: A Field and Petrographic Guide to Hydrothermal Alteration Minerals: Geological Association of Canada, Mineral Deposits Division, 120 p.

Toscana Aparicio, A., 2017, Balneario El Géiser: una experiencia de turismo comunitario en México. Cuadernos de Geografía: Revista Colombiana de Geografía, 26, 279–293.

United States Geological Survey (USGS), 1911, Geologic map of North America. Compiled by the United States Geological Survey in cooperation with the Geological Survey of Canada and Instituto Geologico de Mexico, under the supervision of Bailey Willis and George W. Stose: USGS Professional paper, 71.

Ward, H.G., 1981, México en 1827: México, Fondo de Cultura Económica, Trad. de Ricardo Hass.

Wilson, B.W., Hernández, J.P., Meave, T.E., 1955, Un banco calizo en la parte oriental del Estado de Querétaro, México: Boletín de la Sociedad Geológica Mexicana, 18, 1–10.